

## Understanding Catalytic Activity Trends for NO Decomposition and CO Oxidation using Density Functional Theory and Microkinetic Modeling

Falsig, Hanne; Fehrmann, Rasmus; Nørskov, Jens Kehlet

*Publication date:*  
2010

*Document Version*  
Publisher's PDF, also known as Version of record

[Link back to DTU Orbit](#)

*Citation (APA):*

Falsig, H., Fehrmann, R., & Nørskov, J. K. (2010). Understanding Catalytic Activity Trends for NO Decomposition and CO Oxidation using Density Functional Theory and Microkinetic Modeling. Kgs. Lyngby, Denmark: Technical University of Denmark (DTU).

## DTU Library

Technical Information Center of Denmark

---

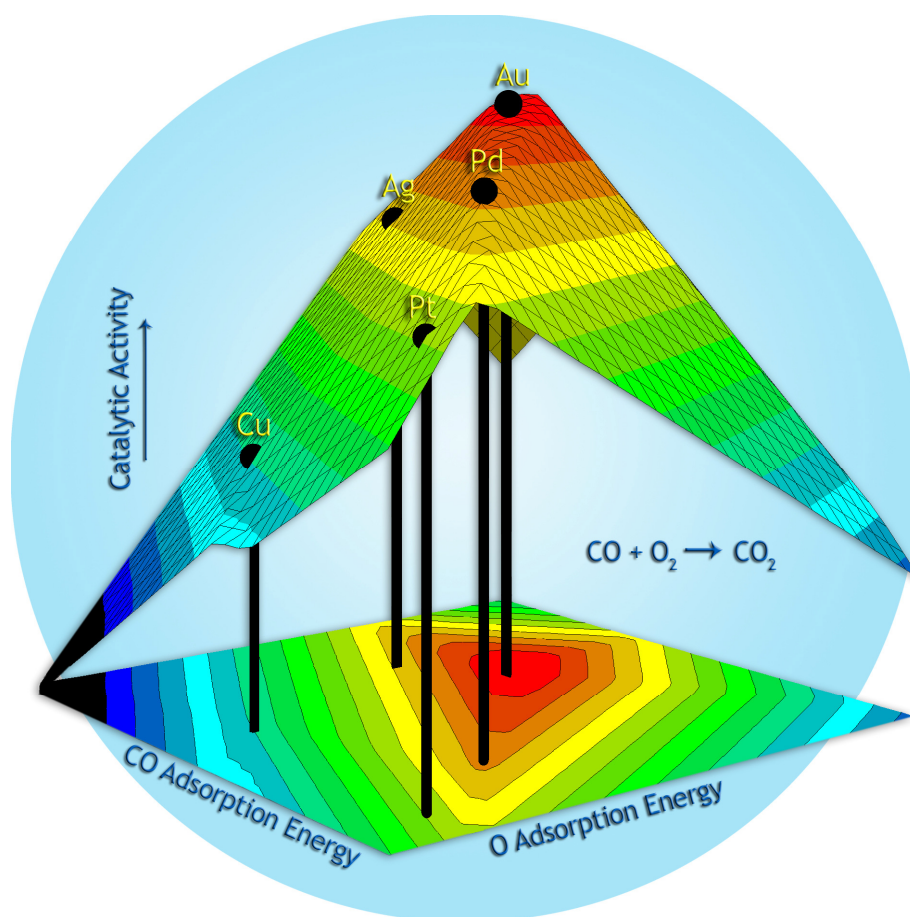
### General rights

Copyright and moral rights for the publications made accessible in the public portal are retained by the authors and/or other copyright owners and it is a condition of accessing publications that users recognise and abide by the legal requirements associated with these rights.

- Users may download and print one copy of any publication from the public portal for the purpose of private study or research.
- You may not further distribute the material or use it for any profit-making activity or commercial gain
- You may freely distribute the URL identifying the publication in the public portal

If you believe that this document breaches copyright please contact us providing details, and we will remove access to the work immediately and investigate your claim.

# Understanding Catalytic Activity Trends for NO Decomposition and CO Oxidation using Density Functional Theory and Microkinetic Modeling



Ph.D. Thesis by

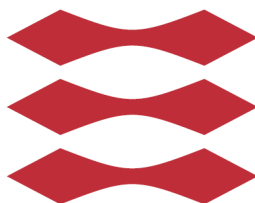
Hanne Falsig

**Understanding Catalytic Activity Trends for NO  
Decomposition and CO Oxidation using Density Functional  
Theory and Microkinetic modeling**

by

**Hanne Falsig**

**DTU**



Thesis submitted for the degree Ph.D. in Chemistry  
July 2010



## Preface

This thesis is submitted in candidacy for a Ph.D. degree from the Technical University of Denmark (DTU). It is based on the work carried out at the Center for Sustainable and Green Chemistry (CSG) and Center for Atomic-scale Materials Design (CAMD) from October 2005 to June 2010 under the supervision of Professor Claus Hviid Christensen and Professor Jens K. Nørskov from DTU. Financial support was provided by the Danish Research Foundation.

I would like to thank my supervisors Claus H. Christensen and Jens K. Nørskov for excellent supervision. I am extremely honored that I had the chance to work for you and I could not have wished for a better supervision team. I thank Claus for giving me the opportunity, being a battery of ideas and always being incredible energetic. I thank Jens for showing great interest in the projects described in this thesis. Especially I thank Jens for his extraordinary motivation and support.

I would like to thank Thomas Bligaard for giving me a driver's license in catalysis and microkinetic modeling. So many hours have been spent with microkinetic modeling – it has been absolutely great. I think Thomas actually managed to turn me into a geek.

I want to thank Britt Hvolbæk for fruitful collaboration on the gold nanoparticle project. I also thank Britt for proofreading of the central parts of this thesis. I thank Lars Grabow for helping me out with the numerical solutions. I would like to thank Marianne Ærsøe for arranging the defense.

And maybe the most important – I want to thank my boyfriend, Brian, for the two wonderful children, Sofia and Mikkel, we had during my Ph.D.

Thank you all for some memorable, inspiring and joyful years.

Lyngby, June, 2010

Hanne Falsig



## Abstract

The main aim of this thesis is to understand the catalytic activity of transition metals and noble metals for the direct decomposition of NO and the oxidation of CO.

The formation of NO<sub>x</sub> from combustion of fossil and renewable fuels continues to be a dominant environmental issue. We take one step towards rationalizing trends in catalytic activity of transition metal catalysts for NO decomposition by combining microkinetic modelling with density functional theory calculations. We establish the full potential energy diagram for the direct NO decomposition reaction over stepped transition-metal surfaces by combining a database of adsorption energies on stepped metal surfaces with known Brønsted–Evans–Polanyi (BEP) relations for the activation barriers of dissociation of diatomic molecules over stepped transition- and noble-metal surfaces. The potential energy diagram directly points to why Pd and Pt are the best direct NO decomposition catalysts among the 3d, 4d, and 5d metals. We analyze the NO decomposition reaction in terms of the Sabatier analysis and a Sabatier–Gibbs-type analysis and obtain an activity trend in agreement with experimental results. We show specifically why the key problem in using transition metal surfaces to catalyze direct NO decomposition is their significant relative overbinding of atomic oxygen compared to atomic nitrogen.

We calculate adsorption and transition state energies for the full CO oxidation reaction pathway by the use of DFT for a number of transition and noble metals; Pt, Pd, Cu, Ag and Au, and for various structures; closed packed surfaces, stepped surfaces, kinked surfaces, and a 12 atom corner model of a larger nanoparticle. We show obtained linear scaling relations between adsorption energies of reaction intermediates and BEP-relations between transition energies and adsorption energies. We establish a simple kinetic framework within the Sabatier analysis and obtain trends in catalytic activity based on the descriptors  $E_O$  and  $E_{CO}$ . We show that gold nanoparticles are optimal catalysts for low temperature CO oxidation and Pt closed packed surfaces are optimal for high temperature CO oxidation. We show that the change in catalytic activity of the elemental metals changes with the coordination number of atoms at the active sites. This effect is shown to

be electronic in nature, as low coordinated metal atoms, which bind reactants most strongly, have the highest energy metal d states.



## Dansk resume

Formålet med denne afhandling er at opnå en forståelse af den katalytiske aktivitet af overgangs og ædle metallerne for den direkte NO dekomponering og CO oxidation. Dannelsen af NO<sub>x</sub> fra forbrænding af brændstoffer er til stadighed et vigtigt miljøspørgsmål. Ved at kombinere DFT beregninger og mikrokinetisk modellering tager vi her et skridt mod at rationalisere tendenser i den katalytiske aktivitet af en række overgangs metaller og ædle metaller i den direkte dekomponering af NO.

For den direkte dekomponering af NO på steppede overgangs og ædle metaller overflader, etablerer vi et potential energi diagram for den fulde reaktion. Dette gøres ved at kombinere adsorptions energier fra en database med kendte BEP-relationer, hvorfra vi bestemmer aktiveringsenergi for de enkelte elementar reaktionerne. Potential energi diagrammet viser, hvorfor Pd og Pt er de bedste katalysatorer til direkte NO dekomponering, blandt 3d, 4d, og 5d metallerne. Yderligere opnår vi en beskrivelse af tendenser i den katalytiske aktivitet fra Sabatier Analyse og Sabatier-Gibbs Analyse i overensstemmelse med eksperimentelle opnåede tendenser. Vi viser, at hovedproblemet med at anvende steppede metaloverflader til at katalysere NO dekompositionen, ligger i at bindingen af atomart oxygen er for stærk sammenlignet med bindingen af atomart nitrogen.

Ved brug af DFT beregner vi adsorptions energier og aktiverings energier for den fulde CO oxidations reaktion for et antal overgangs og ædle metaller; Au, Ag, Cu, Pd, Pt, og for forskellige geometriske strukturer; (111)-overflader, (211)-overflader, (532)-overflader og for M12 hjørne-modellen af en større nanopartikel. Vi viser de opnåede lineære relationer mellem adsorptions energier, og mellem aktiverings energier og adsorptions energier. Vi etablerer en simple mikrokinetisk model indenfor Sabatier analysen og opnår en beskrivelse af tendenser i den katalytiske aktivitet baseret på  $E_O$  and  $E_{CO}$  alene. Vi viser, at for lave temperaturer er guld i nanopartikel form den bedste katalysator og ved høje temperaturer er Pt(111) overflader den bedste CO oxidations katalysator. Ændringen i den katalytiske aktivitet for de enkelte metaller som funktion af geometrien er korreleret til metalkoordinationen af det aktive site. Yderligere viser vi, at

denne effekt er elektronisk af nature, eftersom at de lavt koordinerede metalatomer der binder reaktanterne stærkest, har de højest liggende d-tilstande.

## List of Included Papers

### Paper I

#### Trends in catalytic NO decomposition over transition metal surfaces

Hanne Falsig, Thomas Bligaard, Jeppe Rass-Hansen, Arkady L. Kustov, Claus H. Christensen and Jens K. Nørskov  
*Topics in Catalysis* **45** 117 (2007)

### Paper II

#### Direct NO decomposition over stepped transition-metal surfaces

Hanne Falsig Thomas Bligaard, Claus H. Christensen and Jens K. Nørskov  
*Pure and Applied Chemistry* **79** 1895 (2007)

### Paper III

#### Trends in CO Oxidation Rates for Metal Nanoparticles and Close-Packed, Stepped, and Kinked Surfaces

Tao Jiang, Duncan J. Mowbray, Sergey Dobrin, Hanne Falsig, Britt Hvolbæk, Thomas Bligaard, Jens K. Nørskov  
*J. Phys. Chem. C* **113** 10548 (2009)

### Paper IV

#### Trends in the catalytic CO oxidation activity of nanoparticles

Hanne Falsig, Britt Hvolbæk, Iben S. Kristensen, Tao Jiang, Thomas Bligaard, Claus H. Christensen, Jens K. Nørskov  
*Angew. Chem. Int. Ed.* **47** 4835 (2008)

### Paper V

#### Catalytic activity of Au nanoparticles

Britt Hvolbæk, Ton V. W. Janssens, Bjerne S. Clausen, Hanne Falsig, Claus H. Christensen, Jens K. Nørskov, *NANO TODAY* **2** 14 (2007)

## **Paper VI**

### **Insights into the reactivity of supported Au nanoparticles: combining theory and experiments**

Ton V.W. Janssens, Bjerne S. Clausen, Britt Hvolbæk, Hanne Falsig, Claus H. Christensen, Thomas Bligaard, Jens K. Nørskov Top. Catal. 44 15 (2007)

## **Other Publications**

### **Bioethanol: fuel or feedstock?**

Jeppé Rass-Hansen, Hanne Falsig, Betina Jørgensen, Claus H. Christensen,  
J. Chem. Technol. Biotechnol. **82** 329 (2007)

### **Book chapters**

Peter Fristrup., Hanne Falsig., Marie-Louise Dahl Thomsen, Computerkemi: En in silico opdagelsesrejse, i *Nye Kemiske Horisonter*, DTU, (2007) 72.

Hanne Falsig, Computerkemi: In silico opdagelsesrejser, *ISIS Kemi B, Systime* (2007)  
140.

# Table of Contents

<b>CHAPTER 1</b> .....	<b>1</b>
<b>INTRODUCTION</b> .....	<b>1</b>
Outline .....	3
<b>CHAPTER 2</b> .....	<b>4</b>
<b>ELECTRONIC STRUCTURE THEORY</b> .....	<b>4</b>
2.1 The Schrödinger Equation.....	4
2.2 Density Functional Theory.....	5
2.2.1 The Hohenberg-Kohn Theorems .....	5
2.2.2 The Kohn-Sham equations.....	6
2.3 The Exchange-Correlation functional, plane waves and pseudopotentials.....	8
<b>CHAPTER 3</b> .....	<b>10</b>
<b>HETEROGENEOUS CATALYSIS</b> .....	<b>10</b>
3.1 Catalysis .....	10
3.2 Chemisorption.....	12
3.3 Surface structure.....	13
3.4 Brønsted-Evans-Polanyi relations for surface reactions .....	14
3.5 Electronic and geometric effects.....	16
3.6 Volcano curves in heterogeneous catalysis .....	17
<b>CHAPTER 4</b> .....	<b>19</b>
<b>MICROKINETIC MODELING</b> .....	<b>19</b>
4.1 Introduction .....	19
4.2 The Sabatier Analysis .....	21
4.2.1 Activation barriers .....	21
4.2.2 The approach to equilibrium .....	22
4.2.3 The Sabatier rate.....	23
4.3 Sabatier-Gibbs Analysis.....	23

4.4 Volcano curves .....	26
<b>CHAPTER 5.....</b>	<b>28</b>
<b>THE DIRECT DECOMPOSITION OF NO ON TRANSITION METAL SURFACES</b> .....	<b>28</b>
<b>5.1 Introduction .....</b>	<b>28</b>
<b>5.2 Method .....</b>	<b>29</b>
5.2.1 Experimental .....	29
5.2.2 Microkinetic models for the direct decomposition of NO.....	29
5.2.3 The Sabatier Rate .....	31
5.2.4 The Sabatier-Gibbs Rate .....	31
<b>5.3 Results .....</b>	<b>33</b>
5.3.1 Potential energy diagram for direct NO decomposition.....	33
5.3.2 Scaling relations .....	35
5.3.3 Sabatier and Sabatier-Gibbs volcanoes.....	35
5.3.4 Finding the optimal catalyst .....	38
<b>5.4 Conclusion.....</b>	<b>39</b>
<b>CHAPTER 6.....</b>	<b>40</b>
<b>CATALYTIC ACTIVITY OF SURFACES AND NANOPARTICLES FOR CO</b> <b>OXIDATION .....</b>	<b>40</b>
<b>6.1 Introduction .....</b>	<b>41</b>
<b>6.2 Method .....</b>	<b>43</b>
6.2.1 Computational details .....	43
<b>6.3 Microkinetic modeling .....</b>	<b>44</b>
6.3.1 The Sabatier Analysis .....	44
6.3.2 The analytical steady state solution .....	47
<b>6.4 Results .....</b>	<b>49</b>
6.4.1 Scaling relations .....	49
6.4.2 Volcanoes .....	52
<b>6.5 Validation of the Microkinetic Model.....</b>	<b>54</b>
<b>6.6 The Complete Picture .....</b>	<b>55</b>
6.6.1 Scaling Relations.....	56
6.6.2 Volcanoes .....	58
6.6.3 Electronic structure effect .....	59
<b>6.7 Conclusion.....</b>	<b>60</b>
<b>SUMMARY AND OUTLOOK.....</b>	<b>61</b>

**BIBLIOGRAPHY .....63**



# Chapter 1

## Introduction

Heterogeneous catalysis is one of the major industries worldwide. Catalysis is used to facilitate the production of many chemicals and materials that we use every day. It provides a range of products from fuels and fertilizers to plastics and pharmaceuticals. Catalysts are also utilized for the cleaning of exhaust from cars, power plants, and industrial production. The proliferation of heterogeneous catalysis during the 20th century has indeed led to a significant improvement in the living standard of a large fraction of the world's population. It is perhaps therefore natural that one of the hundreds of important heterogeneous catalytic reactions was selected as the most important invention of the 20th century, ahead of the discovery of penicillin, the construction of the first transistor and the design of the integrated semiconductor circuit [1].

Within this thesis we will focus on heterogeneous catalysis, where the catalyst is in the solid state and the reactants and products in the gas-phase. A catalytic reaction is made up of three major steps. First the gas phase reactants adsorb on the catalyst. Next the reaction intermediates react at the catalyst and finally the catalyst lets the products desorb from the surface of the catalyst into the gas phase. A catalytic reaction takes place at the active site of the catalyst. Therefore the active site is a key component in heterogeneous catalysis [2]. Density functional theory calculations have reached a good accuracy and efficiency for obtaining adsorption and transition state energies for catalytic reactions in heterogeneous catalysis [3, 4]. In combination with microkinetic modeling it is possible to study trends in catalytic activity from one metal to the next – and from one local structure to the next. We can thus obtain an atomic level understanding of the optimal catalyst composition and structure. Further we can understand the underlying catalyst properties causing the change in activity from one metal to the next and for different surface structures in terms of electronic and geometrical effects.

In this thesis we aim to understand which catalytic properties determine the catalytic activity at a fundamental level for direct NO decomposition on stepped transition metal surfaces and for CO oxidation on various structures of transition metals. We base such an understanding on combining DFT [3] with microkinetic modeling. For a given catalyst of a certain structure and composition we map out the full potential energy diagram for NO decomposition and CO oxidation from DFT calculations on adsorption and transition state energies. From linear scaling and Brønsted-Evans-Polanyi relations [5, 6] we predict the parameters most important in determining the catalytic activity and we use these in a microkinetic model to obtain trends in catalytic activity.

## Outline

In Chapter 2 a brief description of the basic of density functional theory is given. Throughout this thesis DFT have been employed to obtain reaction and activation energies for the direct NO decomposition reaction and the CO oxidation reaction.

In Chapter 3 the topics in heterogeneous catalysis relevant for this thesis are described briefly; catalytic reactions, chemisorption, BEP-relations, surface structure and volcano curves are covered.

In Chapter 4 an introduction to the simple kinetic framework, The Sabatier Analysis, and the more constrained Sabatier-Gibbs Analysis is given. These microkinetic models form, together with DFT, the basis for the research results obtained during this PhD.

In Chapter 5 trends in direct NO decomposition on (211) transition metal surfaces are described from BEP-relations and volcano curves obtained from a combining DFT calculated energies with microkinetic modeling.

In Chapter 6 the focus is on the catalytic activity of nanoparticles. We especially focus on gold nanoparticles and the role of surface structure for the catalytic activity for the CO oxidation reaction.

Finally some overall conclusions and outlook.

## Chapter 2

### Electronic structure theory

This chapter is a summary of the theory behind the electronic structure calculations performed. We use Density Functional Theory (DFT), which is a standard electronic structure method in heterogeneous catalysis. A number of good textbooks [7, 8] and reviews [9, 10] on DFT exist; we refer to these and give here a brief description of the most important aspects of DFT. All the calculations in this thesis are performed using the freely available total energy code DACAPO [11].

#### 2.1 The Schrödinger equation

The Schrödinger equation is central in quantum mechanics. It describes all quantum mechanical properties of a system. Within the Born-Oppenheimer approximation [12] for an isolated N-electron system the time-independent electronic Schrödinger equation is given by:

$$\hat{H}\Psi = E\Psi \tag{1}$$

Here E is the electronic energy of the system and  $\Psi = \Psi(r_1, r_2, \dots, r_N)$  is the many-body wavefunction depending on the spatial coordinates of the electrons,  $r_i$ . In the Born-Oppenheimer approximation the interactions between the nuclei and the electrons are decoupled, and the electrons are moving in a static external potential.

The Hamiltonian  $\hat{H}$  is:

$$\hat{H} = \sum_{i=1}^N \left( -\frac{1}{2} \Delta_i^2 \right) + \sum_{i=1}^N v(\mathbf{r}_i) + \sum_{i < j}^N \frac{1}{|\mathbf{r}_i - \mathbf{r}_j|} = \hat{T} + \hat{V}_{\text{ext}} + \hat{V}_{\text{ee}} \quad (2)$$

Where the first term of the Hamiltonian is a kinetic energy operator,  $\hat{T}$ , the second term is the external potential,  $\hat{V}_{\text{ext}}$ , acting on the electrons (in the absence of an external potential this reduces to the attractive forces between the nuclei and the electrons) and the last term is the electron-electron interaction and is denoted  $\hat{V}_{\text{ee}}$ .

Different wavefunction methods can be used to obtain precise results of equation (2). However such methods are computationally very demanding for extended systems of heterogeneous catalysis.

## 2.2 Density functional theory

In heterogeneous catalysis the standard electronic structure method is Density Functional Theory (DFT). The basic idea behind DFT is that the electronic energy of a system can be written in terms of the electron density,  $\rho$ . This reduces the problem of N interacting electrons with 3N degrees of freedom to 3 degrees of freedom.

### 2.2.1 The Hohenberg-Kohn theorems

In 1964 the very basis of DFT was made Hohenberg and Kohn [13], where they showed that there is a one-to-one correspondence between the potential and the electron density of the ground state. Therefore the total energy is only a functional of the density:

$$E[\rho] = \langle \Psi[\rho] | H | \Psi[\rho] \rangle \quad (1)$$

Further they proved the total energy has a minimum equal to the ground-state energy at the ground-state density. This does not tell anything about the form of the functional dependence of the energy on the density; it only tells us that such a functional exists.

### 2.2.2 The Kohn-Sham equations

The next major breakthrough came one year later in 1965 [14], where Kohn and Sham presented a scheme for obtaining the ground state energy. The scheme represents a way of mapping a many-body problem of a system of interacting particles located in an external potential, onto a system of non-interacting single electron states,  $\varphi_i(\mathbf{r})$ , in an effective potential, with the same ground state density.

They showed that the exact ground-state electronic energy functional of an N-electron system can be written as:

$$E[\rho] = E_{\text{kin}}^{\text{non}}[\rho] + E_{\text{pot}}^{\text{int}}[\rho] \quad (2)$$

where  $E_{\text{kin}}^{\text{non}}[\rho]$  is the kinetic energy for the non-interacting system.  $E_{\text{pot}}^{\text{int}}[\rho]$  is the potential energy of the interacting system:

$$E_{\text{pot}}^{\text{int}}[\rho] = E_{\text{ext}}[\rho] + E_{\text{H}}[\rho] + E_{\text{xc}}[\rho]. \quad (3)$$

where  $E_{\text{ext}}[\rho]$  is the external potential,  $E_{\text{H}}[\rho]$  is the classical Hartree energy term and  $E_{\text{xc}}[\rho]$  is the exchange-correlation term that contains all non-classical electron-electron interactions. The exchange-correlation energy is the main challenge for obtaining accurate results with DFT.

The kinetic energy of the non-interacting electron system is:

$$E_{\text{kin}}^{\text{non}}[\rho] = \sum_i^N \int \varphi_i^*(\mathbf{r}) \nabla^2 \varphi_i(\mathbf{r}) d\mathbf{r} \quad (4)$$

where  $\varphi_i(\mathbf{r})$  are the KS-orbitals which are obtained from solving the KS equations:

$$\left\{ -\frac{1}{2}\nabla^2 + v_{eff}(\mathbf{r}) \right\} \varphi_i = \varepsilon_i \varphi_i \quad (5)$$

where  $\varepsilon_i$  is the KS orbital energy corresponding to the KS orbital,  $\varphi_i$ . The effective potential has the form:

$$v_{eff}(\mathbf{r}) = v_{ext}(\mathbf{r}) + \int \frac{\rho(\mathbf{r}')}{|\mathbf{r} - \mathbf{r}'|} d\mathbf{r}' + v_{xc}(\mathbf{r}) \quad (6)$$

The effective potential is also called the KS potential. The major challenge in DFT lies in obtaining the exchange-correlation potential which is the functional derivative of the exchange-correlation energy,  $E_{xc}[\rho]$ :

$$v_{xc}[\mathbf{r}] = \frac{\delta E_{xc}[\rho(\mathbf{r})]}{\delta \rho(\mathbf{r})} \quad (7)$$

The KS equations are solved in a self-consistent fashion, where we start out with an initial guess of the electron density,  $\rho$ , and by using some approximate form for the functional dependence  $E_{xc}$  we obtain the effective potential in equation (6).

The KS equations are then solved and we obtain the KS orbitals, which can be used to calculate the density:

$$\rho(\mathbf{r}) = \sum_{i=1}^N |\varphi_i(\mathbf{r})|^2. \quad (8)$$

If the density is the same as the initial within a given threshold the calculation is converged and the energy can be computed using equations (2), (3) and (4). If not the new density (or a mixture of the new and the old) is used in equation (6) to obtain the effective potential again and the procedure is reiterated until the density is converged.

The genius part in the KS method is that we calculate the majority of the energy exactly leaving only a small residual term the exchange-correlation to be approximated. Walter Kohn received the Nobel Prize in chemistry for his contributions to DFT in 1998 [3].

### 2.3 The exchange-correlation functional, plane waves and pseudopotentials

The exchange-correlation functional contains all the unknown parts of the total energy functional. In solving the KS-equations the main challenge is finding an accurate enough approximation for the exchange-correlation functional. The approximations most commonly used in solid state physics are the Local Density Approximation (LDA) and the Generalized Gradient Approximation (GGA). In this thesis we use GGA based on the RPBE functional [15], which has shown improvement in the description of the energetics for adsorption of species on surfaces.

The most commonly used basis sets in DFT are plane waves and Gaussians. Here we describe the adsorption on metal structures in unit cells repeated infinitely in space. In the DFT code employed in this thesis DACAPO [11] the wave functions are expanded in a plane wave basis using Bloch's theorem:

$$\psi_i(\mathbf{r}) = \sum_j c_{i,j} \varphi_j(\mathbf{r}) = \sum_G c_{i,\mathbf{k}+\mathbf{G}} e^{i(\mathbf{k}+\mathbf{G})\mathbf{r}} \quad (9)$$

where  $c_{i,\mathbf{k}+\mathbf{G}}$  are the expansion coefficients,  $\mathbf{k}$  is a wave vector in the first Brillouin zone, and  $\mathbf{G}$  is the wave vector in the reciprocal space. In principal an infinite number of plane waves are needed for each  $\mathbf{k}$ -point, however a finite number is sufficient to approximate the wave function and the total energy. In our calculations we limit the number of plane waves by introducing an energy cutoff:

$$\frac{1}{2} |\mathbf{k}+\mathbf{G}|^2 \leq E_{cut-off} \quad (10)$$



Also in order to limit the amount of plane waves needed, we here use ultrasoft Vanderbilt pseudopotentials [16] to describe the core electrons and only the valence electrons are treated explicitly.

## Chapter 3

### Heterogeneous catalysis

In this chapter we will give a brief description of the background for the material presented in this thesis and in the included papers. The overall topic of this thesis is heterogeneous catalysis. We will here present some background of the factors determining the catalytic activity by describing how the adsorption energy of an atom changes from one metal to the next. We will then go on describing the linear relations between reaction and activation energies, the so called Brønsted-Evans-Polanyi (BEP) relation, for a given elemental surface reaction. We will describe the underlying effects in catalytic activity, the electronic and geometric effects, and how these effects can be separated from each other by considering BEP-relations for a given surface reaction at different transition metals and surface structures. Finally we will describe how the BEP-relations ultimately lead to a volcano curve in heterogeneous catalysis. This forms the very basis of this Ph.D-thesis.

### 3.1 Catalysis

A catalyst increases the rate of a chemical reaction. Reactants bind to the surface of the catalyst, bonds are broken, and products are being formed leaving the catalyst unaltered. Thus a good catalyst must bind the reactants and at the same time facilitate the formation of products. In order for the products to desorb a good catalyst must not bind the products too strongly. In this thesis we focus on heterogeneous catalysis in which the reactants and the catalyst are in different phases. In this thesis the reactants and products are in the gas phase and the catalyst is in the solid phase.

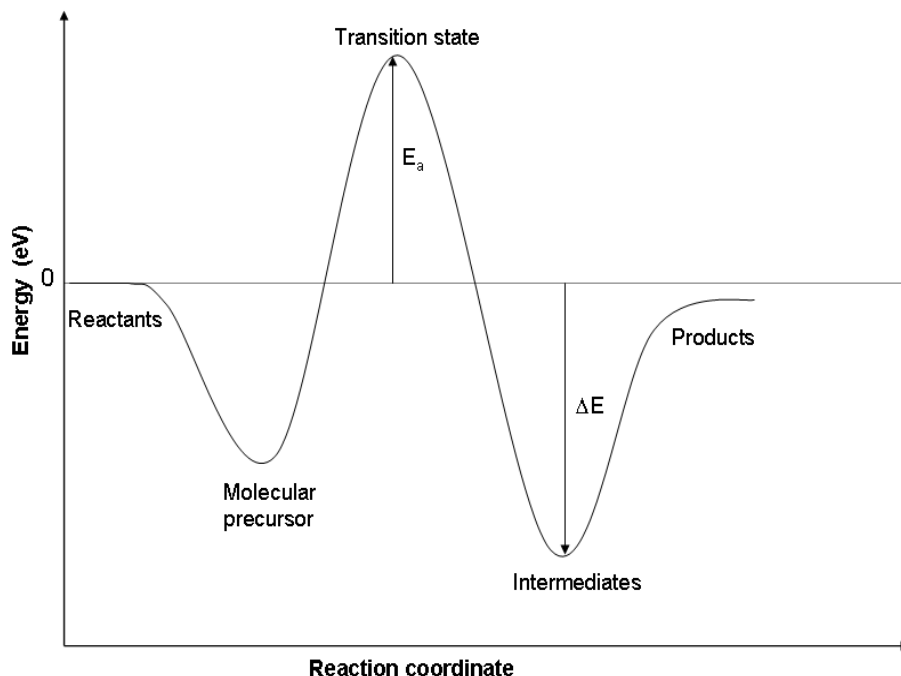


**Figure 1** Schematic energy diagram for a chemical reaction along the reaction coordinate of the reaction.

A catalytic reaction can be described by its potential energy diagram. In Figure 1 such a potential energy diagram is shown. The diagram shows the stability of the intermediates and the activation barrier of the reaction. The initial and final states of the reaction are located at the local minima on the potential energy diagram and the transition state on the local maximum separating them. In order to go from the initial to the final state the transition state must be passed. Here we denote the energy difference between the transition and initial state as the activation energy,  $E_a$ , and the energy difference between the transition state and the energy of the gas-phase reactants as the transition energy. Finally the reaction energy,  $\Delta E$ , is the final state energy,  $E_{FS}$ , minus the initial state energy,  $E_{IS}$ . A catalyst only influences the kinetics of the reaction – e.g. lowers the activation barrier for the process, while the thermodynamics is unaffected.

### 3.2 Chemisorption

The variation in the adsorption energy of a substance from one metal to the next can be understood from the d-band model [17, 18, 19]. In Figure 2 the interaction between the valence state of the adsorbent with the metal s- and d-states is shown.

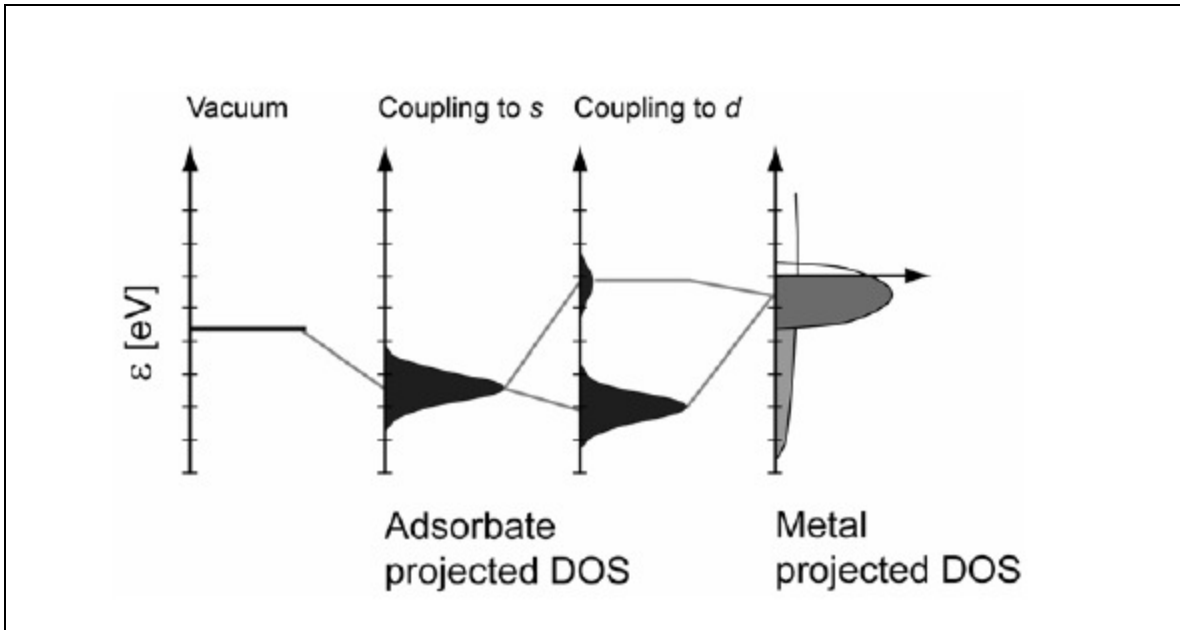


**Figure 2** Schematic of the d-band model. Adapted from Ref. [19]

We think of the adsorption as a two-step procedure. First the valence state of the adsorbate is coupled with the s-state of the metal. This causes a broadening and downshift of the adsorbate state. The transition metals all have half filled s states [20] and therefore this interaction does not change from one transition metal to the next. The interaction between the d-states of the metal and the renormalized adsorbate state is a strong interaction and leads to a splitting in bonding and anti-bonding states below and above the initial states of the adsorbate and the metal. When the antibonding states are shifted above the Fermi level they become empty and therefore the adsorbate will bind more strongly to the metal. Also, bonding states might be shifted down below the Fermi level and become occupied, which will also increase the adsorption energy. Hence trends in adsorption energies between the adsorbent and transition and noble metals will depend primarily on the coupling to the metal d-states.

### 3.3 Surface structure

In Figure 3 the different surface structures studied in this thesis are shown; closed packed, stepped, kinked surfaces, a model of a nanoparticle and a model of the corner of nanoparticle. The coordination number  $N_c$  indicated in Figure 3 is the number of nearest neighbors for the indicated metal atom. For closed packed surfaces each metal atom has coordination number equal 9, for metal atoms at the step of the (211) surfaces it is 7, for kink atoms the number is 6 and the corner metal atoms has 4 nearest neighbors.

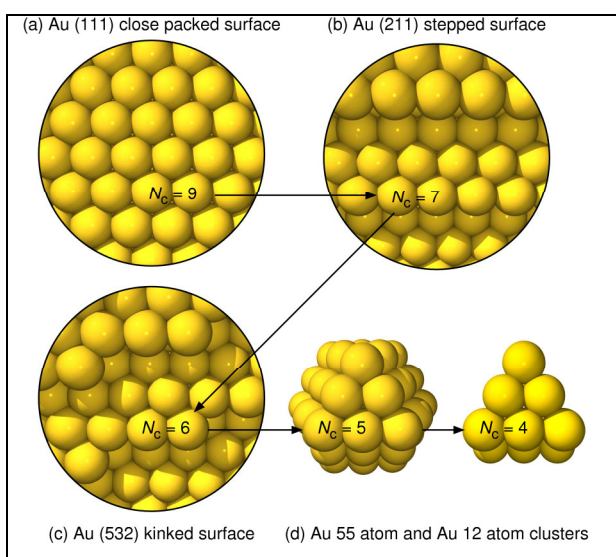


**Figure 3** Schematics of different surface structures (a) (111) closed packed surfaces, (b) stepped surface (c) kinked surface (d) nanoparticle and corner model of a nanoparticle.

Obviously, each structure offers different active sites for catalysis in terms of local geometry. A change in the surface geometry will also lead to a change in the electronic structure of the catalyst. Since we in this thesis study the catalytic activity of transition and noble metals we here characterize the change in electronic structure in terms of shifting the d-band center up or down in energy (see section 3.2).

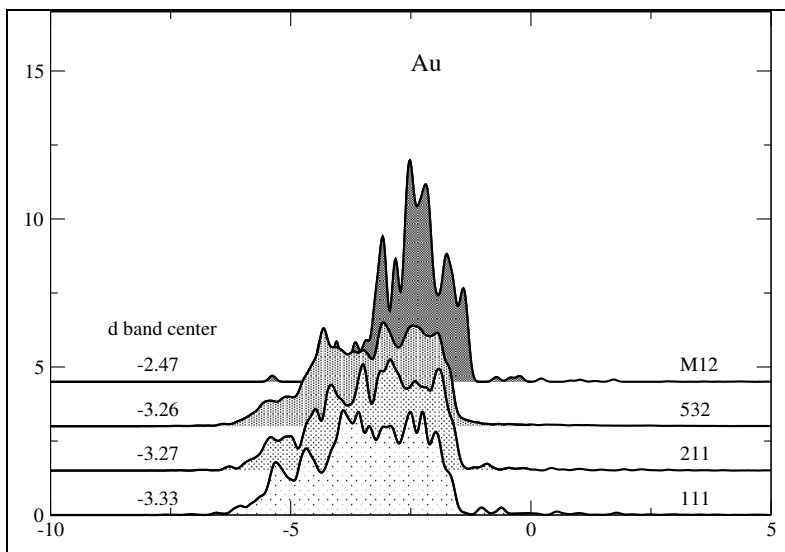


**Figure 4** Local projected DOS for the low coordinated metal atoms on different structures.

In Figure 4 we show the metal d-states for closed packed, stepped, kinked and the M12 corner-model for Au. The energy of the d-band center relative to the Fermi energy is also shown. The figure clearly shows, that the d-band shifts up, when going from high coordinated metal atoms at closed packed surfaces to low coordinated atoms at the corner-model of a nanoparticle. In chapter 6 the effect of changing surface structure will be discussed in detail for the CO oxidation reaction.

### 3.4 Brønsted-Evans-Polanyi relations for surface reactions

Here we will consider the Brønsted-Evans-Polanyi (BEP) relation between the activation energy of a chemical reaction and the reaction energy [5, 6]. It turns out, that the activation energy for a surface reaction is linearly correlated to the reaction energy:

$$E_a = \alpha \Delta E + \beta$$

Where  $E_a$  is the activation barrier for the surface reaction and  $\Delta E$  is the reaction energy. The BEP relationship is found throughout chemistry [31] and in surface chemistry in particular [32, 33, 34, 35].

For a class of heterogeneous catalytic reactions, activation of diatomic molecules ( $A_2 + 2^* \leftrightarrow 2A^*$ ) over transition metal catalysts Nørskov *et al.* [21] found a universal reactant-independent linear relationship between the activation barrier and the reaction energy.

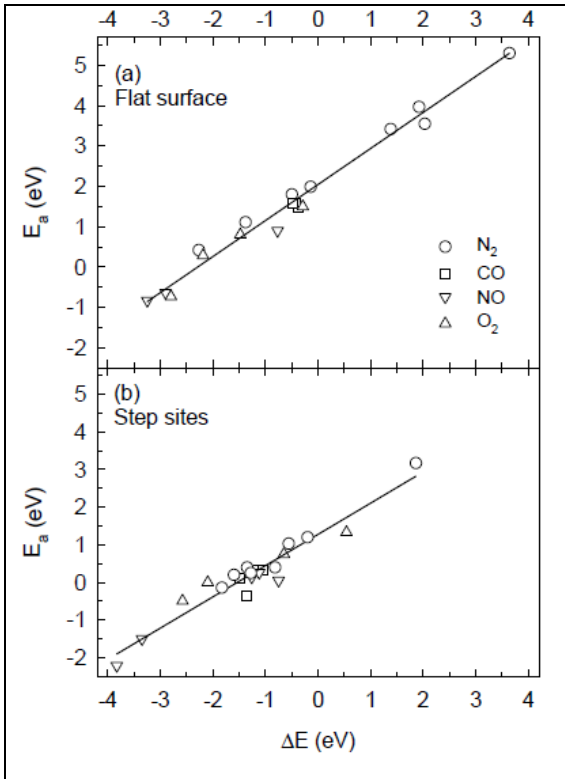


**Figure 5** The universal BEP-relations for dissociative chemisorption of diatomic molecules on (a) closed-packed surfaces and (b) stepped surfaces. Adapted from Ref [21].

The BEP-relations in Figure 5 are for dissociative chemisorption of the diatomic molecules, CO, NO,  $O_2$  and  $N_2$ , on closed-packed and stepped transition metal surfaces. The BEP lines for the different surface reactions fall on the same universal BEP-line, but varies for the closed packed and stepped surfaces.

For closed packed surfaces the BEP relation is:

$$E_a = 0.90\Delta E + 2.07\text{eV} \quad (11)$$

And for stepped surfaces:

$$E_a = 0.87\Delta E + 1.34\text{eV} . \quad (12)$$

The BEP-lines for the closed packed and stepped surfaces are clearly separated. Hence, for the same reaction energy, the activation barrier will be approximately 0.7 eV lower on a stepped metal surface, than on a closed packed surface. In the next section we will discuss the effects in the structure of the surfaces causing this separation. In Chapter 5.2.2 the microkinetic model for direct NO decomposition on stepped transition metal surfaces is based on the BEP relation in equation(12).

### **3.5 Electronic and geometric effects**

The reactivity of surfaces depends on both electronic and geometrical effects. In chapter 3.2 we showed that the d-band center of the transition metals is a good measure of the adsorption strength of the intermediates. The d-band center changes from one transition metal to the next, and as discussed, also by changing the local structure of the active site. A change in the d-band center will act on both the reaction and activation energy of an elementary surface reaction. This is a purely electronic effect. The geometrical effect, on the other hand, is due to a variation in the “geometrical stabilization” of the transition state structure offered by the different surface structures.

One can differentiate the two effects by plotting the Brønsted-Evans-Polanyi (BEP) [5, 6]relation for a given elementary reaction for varying surface structures and metals. The electronic effect acts on both the stability of the intermediates and of the transition state. This corresponds to moving along the BEP line. The geometrical effect is the shift between BEP lines in the vertical direction. Often the change in catalytic activity we observe for changing the surface structures is not either-or, but a combination of both electronic and geometrical effects. In Figure 5 the electronic and geometrical effects are clearly separated for the dissociative chemisorption of diatomic molecules. In Chapter 6



we will show that there is no geometrical effect for a change in surface structure on the CO oxidation reaction.

### 3.6 Volcano curves in heterogeneous catalysis

The French chemist Paul Sabatier stated in 1911 that the interaction between the catalyst and the adsorbate should be "just right"; that is, neither too strong nor too weak [22]. If the interaction is too weak the catalyst will e.g. be unable to dissociate a bond. On the other hand, if the interaction is too strong, the reaction intermediates will be unable to desorb from the catalyst. Due to the linear scaling between adsorption energies, and between activation energies and adsorption energies for surfaces reactions, the trend in catalytic activity for metals of different reactivity in the Periodic Table can be understood directly based on a single descriptor, which we often choose to be the dissociative chemisorption energy of the key reactant. This leads to the volcano curve for catalytic reaction.

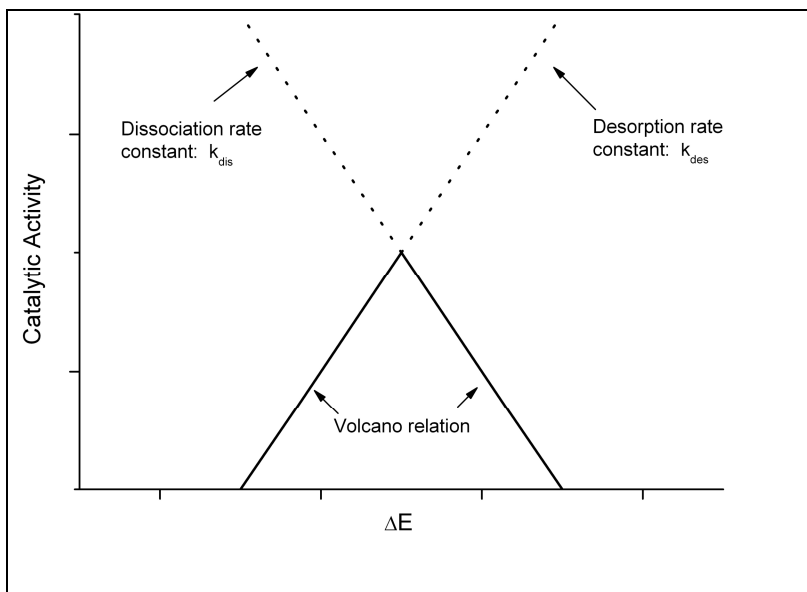


**Figure 6** The catalytic activity versus the reaction energy of the dissociation reaction. More negative reaction energy (left) signifies that the adsorption reaction is more exothermic.

An activity trend such as the schematic plot shown in Figure 6 will often appear (a volcano relation). For more reactive metals ( $\Delta E$  further to the left) the removal of the

dissociated reactants from the surface into the product gas phase will usually limit the catalytic rate. For the less reactive metals ( $\Delta E$  further to the right) this desorption process is fast, and the dissociation barrier is high, so the catalytic rate is limited by the activation of the key reactants. The optimal catalyst will be one having intermediate reaction energies and the catalyst will be located at the top of the volcano curve, as predicted by P. Sabatier.

## Chapter 4

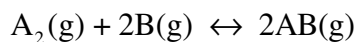
### Microkinetic modeling

Throughout this thesis we are interested in describing the trends in catalytic activity from one transition metal to the next. In Chapter 5 we describe such trends for the NO decomposition reaction on stepped transition metal surfaces and in Chapter 6 we describe trends in the CO oxidation reaction for different catalyst structures and transition metals. We model the reaction rates using a simple kinetic framework within the “Sabatier Analysis” [23]. For the NO decomposition reaction we also use the Sabatier-Gibbs Analysis, which is still within the Sabatier framework, but impose stricter upper bounds on the surface coverages of the reaction intermediates.

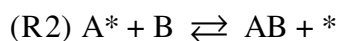
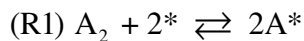
Here we illustrate how to set up the microkinetic models for the Sabatier Analysis and for the Sabatier-Gibbs Analysis. We do this for a simple catalytic reaction and we compare the obtained reaction rates with the rate from the numerical solution.

#### 4.1 Introduction

We consider the simple catalytic reaction



And assume that the reaction proceeds via the two following elementary steps:



where a diatomic gas-phase molecule  $A_2$  is dissociatively adsorbed on a catalyst surface. The adsorbed intermediate reacts with a gas-phase species, B, and associatively desorbs

from the catalyst surface. A species denoted with an asterisk is adsorbed on the catalyst surface and an asterisk is an active site on the catalyst.

The rates for elementary reactions (R1) and (R2) are:

$$r_1 = p_{A_2} k_1^+ \theta_*^2 - k_1^- \theta_A^2 = p_{A_2} \theta_*^2 k_1^+ (1 - \gamma_1) \quad (13)$$

$$r_2 = k_2^+ p_B \theta_A - k_2^- p_{AB} \theta_* = \theta_A p_B k_2^+ (1 - \gamma_2) \quad (14)$$

Where  $p_{A_2}$ ,  $p_B$  and  $p_{AB}$  are the gas-phase partial pressures,  $\theta_*$  and  $\theta_A$  the surface coverage of free sites (\*) and reaction intermediate A respectively.  $\gamma_i$  is the approach to equilibrium for elementary reaction (R<sub>i</sub>).

The rate constant  $k_i$  for step, (R<sub>i</sub>), in the forward or backward direction for each elementary step is given by:

$$k_i = \nu_i \exp \left[ \frac{-\Delta E_{ai} + T \Delta S_{ai}}{k_B T} \right] \quad (15)$$

where  $\nu_i$  is the prefactor. Throughout this thesis we assume the prefactor,  $\nu_i$  is metal independent [24] and equals  $\nu_i = k_B T/h$ .  $\Delta E_{ai}$  is the activation barrier for the reaction and  $\Delta S_{ai}$  the entropy change,  $k_B$  is the Boltzmann constant, and T is the temperature. Further we assume  $\Delta S_{ai} \approx \pm S_{gas}$ , since in general the entropy of the molecules in the adsorbed state is much smaller than the entropy of the gas-phase molecules .

The equilibrium constant is given by:

$$K_i = \frac{k_i^+}{k_i^-} = \exp \left( \frac{-(\Delta E_i - TS_i)}{k_B T} \right) \quad (16)$$

And the approach to equilibrium for the overall gas phase reaction is:

$$\gamma = \frac{1}{K_{\text{eq}}} \frac{p_{\text{AB}}^2}{p_{\text{A}_2} p_{\text{B}}^2} \quad (17)$$

## 4.2 The Sabatier analysis

The Sabatier Analysis was first described by Bligaard *et al* [23]. It is based on three basic assumptions: i) all activation barriers are calculated from known BEP relations, ii) only net-forward rates ( $r_i > 0$ ) are considered, iii) the coverage of free sites and surface species are assumed optimal for each reaction step in the forward direction. We emphasize that these assumptions ensure the Sabatier rate to be an exact upper bound to the reaction rate.

### 4.2.1 Activation barriers

The activation energies for the elementary reactions (R1) and (R2) we obtain from the “universal” BEP-relation [21] for dissociative chemisorption of diatomic molecules on closed-packed transition metal surfaces described in Chapter 3.4.

The activation barrier for the forward rate of the dissociative chemisorption of  $\text{A}_2$  is described by:

$$E_{\text{a1}} = \alpha_1 \Delta E_1 + \beta_1 \quad (18)$$

where  $\Delta E_1$  is the reaction energy for reaction (R1),  $\alpha_1 = 0.87$  and  $\beta_1 = 1.34$  eV.

The backward reaction is just the reverse, hence the activation energy for the associative desorption is given by:

$$E_{\text{a1}}^- = (\alpha_1 - 1) \Delta E_1 + \beta_1. \quad (19)$$

For the activation barrier in the forward direction of (R2) we assume that a BEP-relation exists such that:

$$E_{\text{a2}} = \alpha_2 \Delta E_1 + \beta_2$$

where we choose  $\alpha_2 = -0.13$  and  $\beta_2 = 0.8$  eV . By choosing a negative value for  $\alpha_2$  we ensure that the activation energy increases for a strong binding of reaction intermediate A. For the backward reaction the activation energy is given from:

$$E_{a2}^- = E_{a2}^+ - \Delta E_2 \quad (20)$$

The reaction energy for elementary reaction (R2) is:

$$\Delta E_2 = 1/2(\Delta E_0 - \Delta E_1) \quad (21)$$

where  $\Delta E_0$  is the reaction energy for the overall gas-phase. Since the activation energies for reactions (R1) and (R2) are described by  $\Delta E_1$  , and the reaction energies are linearly related (equation (21)), we have a single descriptor for the catalytic activity and we choose  $\Delta E_1$  as descriptor for the catalytic activity.

#### 4.2.2 The approach to equilibrium

The next basic assumption is that we only consider net forward rates ( $r_i > 0$ ). The approach to equilibrium for an elementary step,  $\gamma_i$  , and overall reaction,  $\gamma$  , are therefore restricted:

$$0 \leq \gamma \leq 1 \text{ and } 0 \leq \gamma_i \leq 1 \quad (22)$$

Since the approach to equilibrium for the overall gas phase reaction is the product of the approaches to equilibrium for the elementary reactions,  $\gamma = \gamma_1 \gamma_2^2$  we obtain the further bound:

$$0 \leq \gamma \leq \gamma_i^n \leq 1 \quad (23)$$

### 4.2.3 The Sabatier rate

Now we address the Sabatier rate. For noble metals the surface will be nearly empty ( $\theta_* = 1$ ) and the dissociative chemisorption of  $A_2$  will be rate determining ( $\gamma_1 = \gamma$  and  $\gamma_2 = 1$ ). Hence an exact upper bound to the rate for reaction (R1) is:

$$r_1 = 2p_{A_2} k_1^+ (1-\gamma) \quad (24)$$

For more reactive metals, the surface coverage will be high ( $\theta_A = 1$ ) and the desorption reaction (R2) will be the rate determining ( $\gamma_1 = 1$  and  $\gamma_2 = \sqrt{\gamma}$ ). And an exact upper bound to the rate is described by:

$$r_2 = p_B k_2^+ (1-\sqrt{\gamma}) \quad (25)$$

Because the surface coverage has an upper bound of 1, the Sabatier rate for the overall reaction must be bound by equation (24) and equation (25):

$$R = \min \left\{ 2k_1 p_{A_2} (1-\gamma), k_2 p_B (1-\sqrt{\gamma}) \right\} \quad (26)$$

### 4.3 Sabatier-Gibbs analysis

The Sabatier Analysis is based on the assumption that the coverage of the reaction intermediates and free sites are “optimal”. However this is probably too optimistic. We here apply a stricter bound on the surface coverages of the reaction intermediates in the forward reactions.

We use that we from equation (23) have lower and upper boundaries on the approach to equilibrium for each elementary reaction, and hence also on the coverages of the reaction intermediates. By using these bounds we ensure that the coverage for each reaction

intermediate is within the interval between the coverage at a given approach to equilibrium for the overall reaction and the equilibrium coverage.

The approach to equilibrium for the overall reaction is

$$\gamma = \frac{1}{K_1 K_2} \frac{P_{AB}^2}{P_B P_{A_2}} \quad (27)$$

For each elementary step the approach to equilibrium is:

$$\gamma_1 = \frac{\theta_A^2 P_{A_2}}{\theta_*^2 K_1} = \frac{\lambda_A^2 P_{A_2}}{K_1} \quad (28)$$

$$\gamma_2 = \frac{\theta_* P_{AB}}{\theta_A P_B K_2} = \frac{P_{AB}}{\lambda_A P_B K_2} = \frac{\sqrt{\gamma K_1 P_{A_2}}}{\lambda_A} \quad (29)$$

Where  $\lambda_A = \theta_A / \theta_*$  is the coverage activity of species A.

From equation (23), the boundaries on  $\gamma_1$  and  $\gamma_2$  are:

$$\gamma \leq \gamma_1 \leq 1 \text{ and } \gamma \leq (\gamma_2)^2 \leq 1 \quad (30)$$

Inserting  $\gamma_1$  and  $\gamma_2$  in eq. (30) we get the following lower and upper bounds on  $\lambda_A$ :

$$\lambda_A^{\min} = \sqrt{P_{A_2} K_1 \gamma} \text{ and } \lambda_A^{\max} = \sqrt{P_{A_2} K_1} \quad (31)$$

From the conservation of sites,  $\sum_{i=1}^n \theta_i = 1$  we have:

$$\theta_{\min}^* = \frac{1}{\lambda_A^{\max} + 1} \text{ and } \theta_{\max}^* = \frac{1}{\lambda_A^{\min} + 1} \quad (32)$$

Therefore the maximum coverage of species A is:



$$\theta_A^{\max} = \lambda_A^{\max} \theta_*^{\min} = \frac{\sqrt{p_{A_2} K_1}}{\sqrt{p_{A_2} K_1 + 1}} \quad (33)$$

We now have expressions of the maximum coverage of the surface intermediate A\*, and the maximum coverage of free sites, within the boundaries given by the coverage at a certain approach to equilibrium and the coverage at equilibrium. It is however important to note that this procedure for obtaining the maximum coverages for each reaction intermediate is only possible for a catalytic reaction, where there is exactly one product and reaction channel for each intermediate.

The Sabatier-Gibbs rate has the same form as equation (26), but with stricter upper bounds on the coverage of each intermediate in the forward direction:

$$R_{SG} = \min \left\{ 2k_1 p_{A_2} \left( \theta_*^{\max} \right)^2 (1-\gamma), k_2 p_B \theta_A^{\max} (1-\sqrt{\gamma}) \right\} \quad (34)$$

## 4.4 Volcano curves

We here study the performance of the Sabatier Analysis and of the Sabatier-Gibbs Analysis. We compare the results with the real rate obtained from the numerical solution.

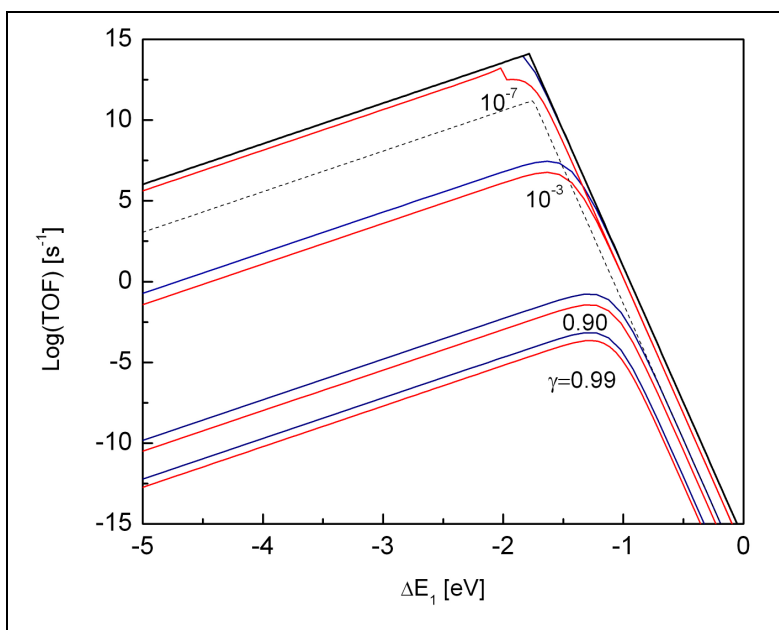


**Figure 7** The Sabatier-Gibbs volcanoes (blue) and real volcanoes (red) for various values of  $\gamma$ . The solid black volcano curve is the Sabatier volcano at  $\gamma = 0$  and the dotted black volcano is the Sabatier volcano for  $\gamma = 0.90$ .

In Figure 7 we present Sabatier, Sabatier-Gibbs and real volcanoes for various overall approaches to equilibrium. The Sabatier and the Sabatier-Gibbs volcanoes are upper bounds to the real rate.

Far from equilibrium the Sabatier volcano is in good agreement with the real volcano, since the coverages of the intermediates for an elementary reaction in the forward direction are approaching “optimal” for  $\gamma \rightarrow 0$ . On the other hand, when we approach equilibrium the Sabatier volcano is still in qualitative agreement with the real volcano, but is far off quantitatively.

In general the Sabatier-Gibbs Analysis of the surface coverages improves the description of Sabatier rate considerably. For  $\gamma \rightarrow 1$  the Sabatier-Gibbs volcano is approaching the real volcano, since the coverages are described exactly at equilibrium. On the other hand the Sabatier-Gibbs description also performs well far from equilibrium, since we here are in the range of optimal coverage. For the case with an intermediate approach to equilibrium the Sabatier-Gibbs rate is an upper bound to the real rate, and is quantitatively still close to the real rate. However for the overall reaction described here the dissociative chemisorption reaction is rate determining for the Sabatier-Gibbs rate for all approaches to equilibrium over the entire energy range, except for  $\gamma = 10^{-7}$ . For more complex catalytic reactions, where there is more than one step forming the volcano, probably the Sabatier-Gibbs volcano will not be in this good agreement with for the real volcano for an intermediate approach to equilibrium.

## Chapter 5

### **The direct decomposition of NO on transition metal surfaces**

This chapter is based on the included papers [25, 26] describing NO decomposition on stepped transition metal surfaces. We study the catalytic direct decomposition of NO to  $N_2$  and  $O_2$  over a series of (211) transition metal surfaces. We combine DFT with microkinetic modeling and obtain a simple tool to describe trends in the catalytic activity for the decomposition of NO. The Sabatier rate is described for the NO decomposition together with more restricted Sabatier-Gibbs rate. The theoretical modeling leads to a volcano curves for the catalytic activity, where the rate for the noble surfaces is limited in how fast the catalyst can dissociate NO and for the more reactive surfaces by how fast the desorption of  $O_2$  occurs. We compare the theoretical obtained activity with the experimentally obtained volcano. And finally we show why transition metal surfaces are probably not the optimal catalysts for decomposition of NO due to a significant overbinding of atomic oxygen compared to the binding of atomic nitrogen.

#### **5.1 Introduction**

Nitrogen oxide, NO, in exhaust gases from the combustion of fossil and renewable fuels is a major source of air pollution. NOx contribute to a range of environmental problems; photochemical smog, acid rain and greenhouse effects. The increasingly stringent emission requirements for diesel engines require NOx abatement technology, which is effective under lean-burn conditions. Various technologies such as NOx traps [27] and selective catalytic reduction (SCR) exist [28, 29, 30], but it would be preferable if a simpler process could be developed based on direct NO decomposition. In the direct NO decomposition reaction, the exhaust containing NO is flowed over a heterogeneously catalytic surface, where the NO bond is split, and N atoms recombine to  $N_2$  while the O atoms recombine to  $O_2$ . The direct NO decomposition reaction is thermodynamically favored at low temperatures, but it has proven difficult to

find a catalyst that is both active and oxidation-resistant [31]. Here, we study the direct decomposition of NO over stepped transition metal surfaces, since such step sites are known from theoretical calculations to be significantly more active for NO decomposition than the corresponding close-packed surfaces [21, 32, 33, 34, 35]. This enhanced reactivity of steps also explains why smaller transition-metal particles show enhanced activity for NO decomposition [36].

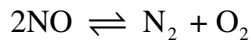
## 5.2 Method

### 5.2.1 Experimental

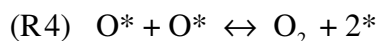
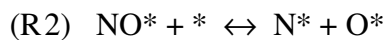
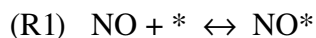
The catalysts were prepared by incipient wetness impregnation of metal solutions on a  $\text{MgAl}_2\text{O}_4$  support, with a surface area of  $70 \text{ m}^2/\text{g}$  and using metal concentrations of  $92 \text{ }\mu\text{mol}/\text{g}$ . Of each catalyst, 300 mg, was placed in a quartz tube reactor. A flow of 25 ml/min of 1 vol. % NO in He was then admitted to the reactor at ambient pressure. The activity was measured at 600-650°C. At each temperature, the measurement was performed for two hours to achieve stable conversions. The concentrations of NO,  $\text{N}_2$  and  $\text{O}_2$  were monitored using gas chromatography with a Thermal Conductivity Detector and a molecular sieve packed column. In all experiments, no traces of  $\text{N}_2\text{O}$  or other products were detected.

### 5.2.2 Microkinetic models for the direct decomposition of NO

The overall NO decomposition reaction is:



The decomposition is assumed to take place in four elementary steps:



A species denoted with an asterisk is adsorbed on an active site on the transition metal catalyst, where an asterisk is a vacant active site on the surface.

The rates for the elementary reactions are given by:

$$r_1 = p_{\text{NO}}\theta^*k_1^+ - \theta_{\text{NO}}k_1^- = p_{\text{NO}}\theta^*k_1^+(1-\gamma_1) \quad (35)$$

$$r_2 = \theta_{\text{NO}}\theta^*k_2^+ - \theta_{\text{N}}\theta_{\text{O}}k_2^- = \theta_{\text{NO}}\theta^*k_2^+(1-\gamma_2) \quad (36)$$

$$r_3 = \theta_{\text{N}}^2k_3^+ - \theta_{\text{N}_2}^2k_3^- = \theta_{\text{N}}^2k_3^+(1-\gamma_3) \quad (37)$$

$$r_4 = \theta_{\text{O}}^2k_4^+ - \theta_{\text{O}_2}^2k_4^- = \theta_{\text{O}}^2k_4^+(1-\gamma_4) \quad (38)$$

Where  $p_{\text{NO}}$ ,  $p_{\text{N}_2}$  and  $p_{\text{O}_2}$  are the gas-phase partial pressures,  $\theta^*$ ,  $\theta_{\text{NO}}$ ,  $\theta_{\text{O}}$  and  $\theta_{\text{N}}$  the surface coverage of free sites (\*), NO, O and N. The rateconstants are given from:

$$k_i = v_i \exp\left[\frac{-\Delta E_{\text{ai}} + T\Delta S_{\text{ai}}}{k_{\text{B}}T}\right] \quad (39)$$

We here assume that the prefactors and adsorption entropies are metal-independent. Since all elementary steps are dissociation or association reactions for diatomic molecules we use the universal Brønsted-Evans-Polanyi relation for stepped surfaces from Ref. [21], described in Chapter 3.4, to describe the transition state energies  $E_{\text{TS2}}$ ,  $E_{\text{TS3}}$  and  $E_{\text{TS4}}$  from reaction energies. Trends in the catalytic activity for the direct decomposition of NO is determined from following metal-dependent parameters:  $E_{\text{NO}}$ ,  $E_{\text{O}}$  and  $E_{\text{N}}$ .

The modelled NO decomposition rates, The Sabatier rate and Sabatier-Gibbs rate, are calculated using the experimental conditions for the initial partial pressure, and 5% conversion of NO corresponding to average experimental conversion.

### 5.2.3 The Sabatier rate

The Sabatier Analysis is described in Chapter 4.2 and in Ref. [23]. For the NO decomposition reaction we obtain the following Sabatier elementary rates:

$$r_{s1} = p_{NO}k_1^+ (1-\sqrt{\gamma}), r_{s2} = 1/4k_2^+ (1-\sqrt{\gamma}), r_{s3} = 2k_3^+ (1-\gamma) \text{ and } r_{s4} = 2k_4^+ (1-\gamma)$$

The Sabatier rate for the total reaction is bounded by the rates for the individual steps:

$$R_S = \min \left[ p_{NO}k_1^+ (1-\sqrt{\gamma}), 1/4k_2^+ (1-\sqrt{\gamma}), 2k_3^+ (1-\gamma), 2k_4^+ (1-\gamma) \right] \quad (40)$$

### 5.2.4 The Sabatier-Gibbs rate

In order to determine the Sabatier-Gibbs rate for the NO decomposition we follow the procedure outlined in Chapter 4.3. For the elementary reaction (R1)-(R4) the approach to equilibrium is given by:

$$\gamma_1 = \frac{\lambda_{NO}}{K_1 p_{NO}}, \gamma_2 = \frac{1}{K_2} \frac{\lambda_N \lambda_O}{\lambda_{NO} \lambda_*}, \gamma_3 = \frac{p_{N_2}}{K_3} \frac{1}{\lambda_N^2} \text{ and } \gamma_4 = \frac{p_{O_2}}{K_4} \frac{1}{\lambda_O^2}$$

Where the surface activity,  $\lambda_x$  for the adsorbed reaction intermediates

$$\text{are: } \lambda_{NO} = \theta_{NO}/\theta_* \quad \lambda_N = \theta_N/\theta_* \quad \text{and } \lambda_O = \theta_O/\theta_* .$$

The boundaries on the coverage of NO are obtained from the boundaries on the approach to equilibrium for reaction R1. The maximum possible coverage of NO is obtained, when reaction (R1) is at equilibrium:

$$\gamma_1 = 1 \Rightarrow \lambda_{NO}^{\max} = p_{NO} K_1 \quad (41)$$

The coverage of NO will be at the minimum value when the reaction being as far from equilibrium as the overall reaction “allows”:

$$\gamma_1^2 = \gamma \Rightarrow \lambda_{\text{NO}}^{\min} = p_{\text{NO}} K_1 \sqrt{\gamma}. \quad (42)$$

Similarly the boundaries on the surface activity N from the boundaries on the approach to equilibrium for reaction (R3):

$$\lambda_{\text{N}}^{\min} = \sqrt{p_{\text{N}_2}/K_3} \text{ and } \lambda_{\text{N}}^{\max} = \sqrt{p_{\text{N}_2}/K_3} \gamma. \quad (43)$$

From the boundaries on the approach to equilibrium for reaction (R4) the boundaries on  $\lambda_{\text{O}}$  are:

$$\lambda_{\text{O}}^{\min} = \sqrt{p_{\text{O}_2}/K_4} \text{ and } \lambda_{\text{O}}^{\max} = \sqrt{p_{\text{O}_2}/K_4} \gamma. \quad (44)$$

From the conservation of sites,  $\sum \theta_x = 1$ , we can express the coverage of free surface sites in terms of the surface activities of the adsorbed species:

$$\theta_* = 1 / (1 + \lambda_{\text{NO}} + \lambda_{\text{O}} + \lambda_{\text{N}}) \Rightarrow \begin{cases} \theta_*^{\min} = 1 / (1 + \lambda_{\text{NO}}^{\max} + \lambda_{\text{O}}^{\max} + \lambda_{\text{N}}^{\max}) \\ \theta_*^{\max} = 1 / (1 + \lambda_{\text{NO}}^{\min} + \lambda_{\text{O}}^{\min} + \lambda_{\text{N}}^{\min}) \end{cases} \quad (45)$$

The maximum coverages for NO, O and N are:

$$\theta_{\text{NO}}^{\max} = \lambda_{\text{NO}}^{\max} \theta_*^{\min} = \theta_*^{\min} p_{\text{NO}} K_1 \quad (46)$$

$$\theta_{\text{N}}^{\max} = \lambda_{\text{N}}^{\max} \theta_*^{\min} = \theta_*^{\min} \sqrt{p_{\text{N}_2}/K_3} \gamma \quad (47)$$

$$\theta_{\text{O}}^{\max} = \lambda_{\text{O}}^{\max} \theta_*^{\min} = \theta_*^{\min} \sqrt{p_{\text{O}_2}/K_4} \gamma \quad (48)$$



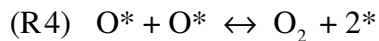
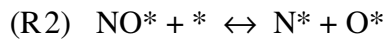
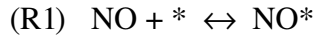
We now have expressions for the optimal coverages in a Sabatier-Gibbs sense. The Sabatier-Gibbs rate for the decomposition of NO is bounded by the rates for the elementary steps:

$$R_{SG} = \min \left\{ \theta_*^{\max} p_{NO} k_1 (1 - \sqrt{\gamma}), \theta_*^{\max} \theta_{NO}^{\max} k_2 (1 - \sqrt{\gamma}), k_3 (\theta_N^{\max})^2 (1 - \gamma), k_4 (\theta_O^{\max})^2 (1 - \gamma) \right\}$$

## 5.3 Results

### 5.3.1 Potential energy diagram for direct NO decomposition

In Figure 8 we have constructed a potential energy diagram for the decomposition of NO on a series of transition metal catalysts, showing adsorption and transition state energies. The adsorption energies are from Ref. [23] and the activation barriers are obtained from BEP-relations. As described in the previous section, the decomposition is assumed to take place via four elementary steps:



The decomposition reaction has two main parts. First the NO molecule adsorbs and dissociates at the metal surface (R<sub>1</sub> and R<sub>2</sub>), next N<sub>2</sub> and O<sub>2</sub> from the atomic precursors and are recombined and removed from the metal surface (R<sub>3</sub> and R<sub>4</sub>). A good catalyst for the direct NO decomposition is characterized by a low activation barrier for NO dissociation and weak binding of the intermediates.

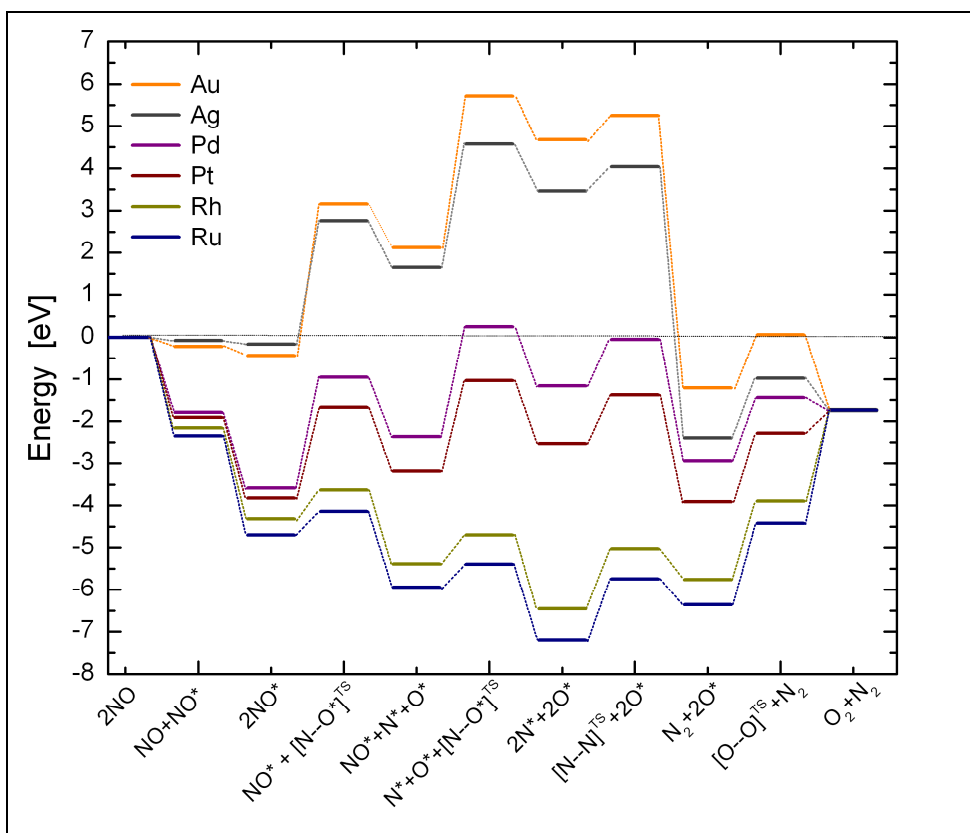


**Figure 8** Potential energy diagrams for the direct NO decomposition reaction over transition metal surfaces. A more negative energy means stronger adsorption. Adsorption energies of reaction intermediates are from Ref. [23] and transition state energies calculated applying the universality principle [21] on these energies.

The reaction intermediates, NO, N and O, adsorb strongly to the less noble transition metals, Rh and Ru, have intermediate binding energies on Pt and Pd, and adsorb weakly to the noblest of the transition metals, Ag and Au. Strong adsorption energies of the reaction intermediates on one hand favor the dissociation of NO and on the other hand hinder the associative desorption of the reaction products, O<sub>2</sub> and N<sub>2</sub>. Therefore, as seen in Figure 8, for the noblest metals, the adsorption of NO is simply too weak for the dissociation to take place, and on the other hand Ru and Rh tend to overbind the intermediates facilitating the dissociation of NO, but making the associative desorption of N and O difficult. The best catalysts must be Pd and Pt, since these do not overbind the intermediates to the same extent as Rh and Ru, and at the same time do not present the same problems with unstable reaction intermediates as the more noble catalysts Au and Ag.

### 5.3.2 Scaling relations

In Figure 9 the dissociative chemisorption energies for NO, O<sub>2</sub>, and N<sub>2</sub> on the transition metals are presented. The energies are highly correlated. Linear best fits of the energies show that the dissociation energy for adsorbed NO is described very well with the dissociative chemisorption energy for O<sub>2</sub> and less well with the corresponding energy for N<sub>2</sub> dissociation.

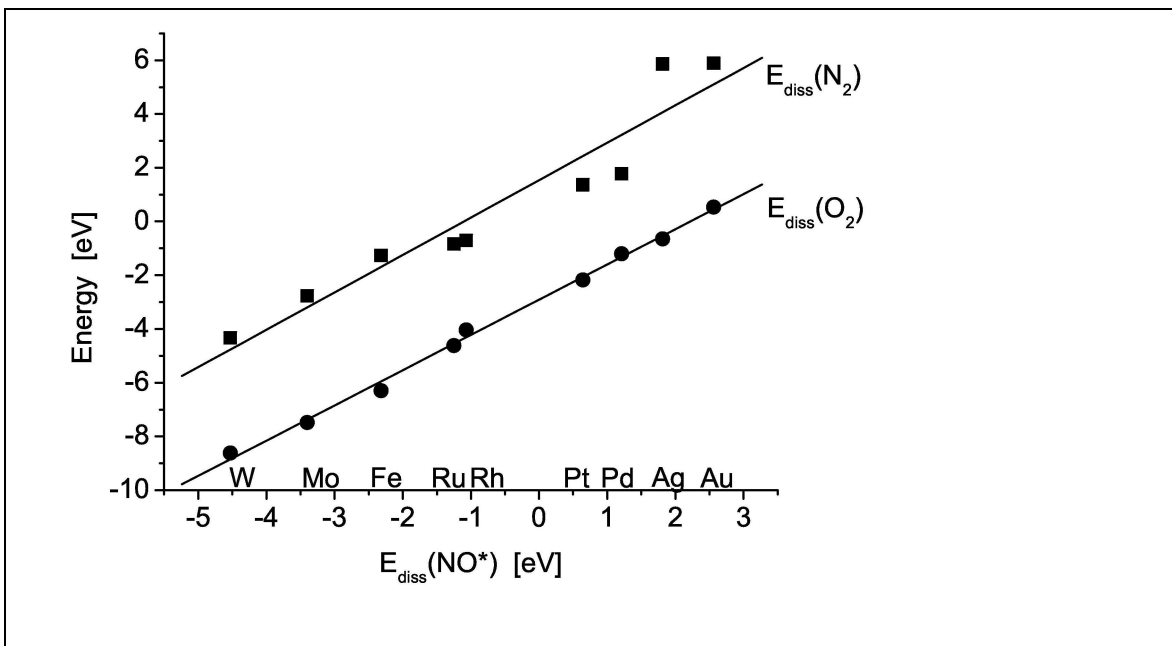


**Figure 9** The figure shows the dissociative chemisorption energies for N<sub>2</sub> and O<sub>2</sub> versus the dissociation energy of adsorbed NO. Correlation equations are obtained from linear best fits,  $E_{\text{diss}}(\text{O}_2) = 1.31E_{\text{diss}}(\text{NO}^*) - 2.91$  eV,  $R^2 = 0.99$ <sup>1</sup>;  $E_{\text{diss}}(\text{N}_2) = 1.39E_{\text{diss}}(\text{NO}^*) + 1.54$  eV,  $R^2 = 0.91$

Since the reaction energies of the elementary steps are highly correlated, we can choose just one reaction energy as the descriptor for the catalytic activity in the microkinetic model. We choose the dissociation energy of NO as descriptor for the catalytic activity.

### 5.3.3 Sabatier and Sabatier-Gibbs volcanoes

In Figure 10 we show the Sabatier rates for the elementary reactions, together with the Sabatier and the Sabatier-Gibbs volcanoes as a function of the dissociation energy for NO. The dissociation rate of NO is fast at the surfaces of the more reactive metals to the left in the periodic table and slow at the noble metals, and the rate is the limiting step for

<sup>1</sup> The linear values have been corrected from Ref. [26].

the overall NO decomposition on Au, Ag and Pd. On these metals the weak binding of oxygen facilitates the associative desorption of O<sub>2</sub>, where the strong binding at the more reactive metals like Ru and Rh inhibits the associative desorption and causes the rate to be limiting for the overall reaction. Oxygen is at all surfaces more strongly adsorbed to the metals than nitrogen and for this reason is associative desorption for N<sub>2</sub> is faster than O<sub>2</sub> for all the transition metals here. From the individual rates a Sabatier type volcano is formed (the Sabatier rate).

At the left leg of the Sabatier volcano the NO decomposition is limited by a too strong adsorption (the reactive transition metals) of oxygen and on the right side (the more noble metals) the weak interaction hinders the dissociation of NO in agreement with the Sabatier principle [22]. This is also the picture one would expect from the discussion of the energies in section 5.3.1 .

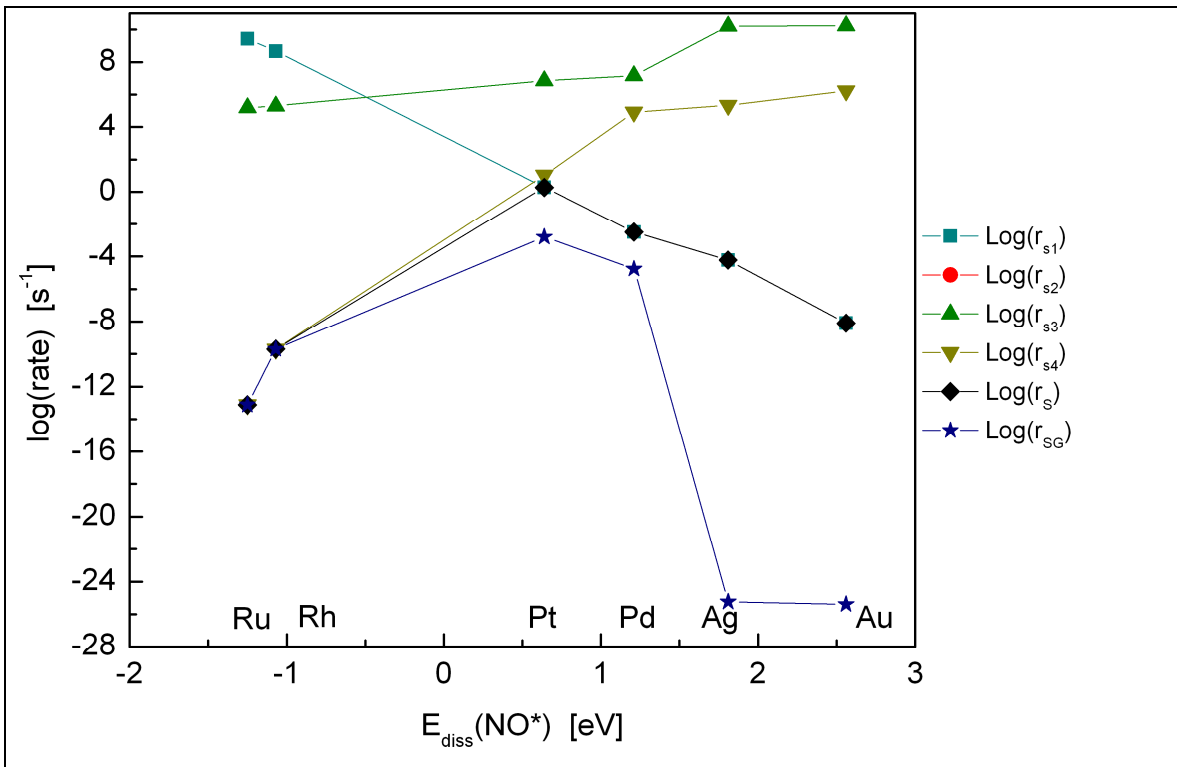


**Figure 10** Sabatier rates for each elementary reaction and the Sabatier and the Sabatier-Gibbs volcano curves versus the dissociation energy of adsorbed NO.  $r_{s1}$  is the rate for adsorption of NO,  $r_{s2}$  is the rate for dissociation of NO,  $r_{s3}$  is the rate for associative desorption of N<sub>2</sub> and  $r_{s4}$  is the rate for associative desorption of O<sub>2</sub>. . The Sabatier-Gibbs rate has been slightly corrected from the Sabatier-Gibbs volcano in Ref. [26].

The activity ranking can be compiled:  $\text{Pt} > \text{Pd} > \text{Ag} > \text{Au} > \text{Rh} > \text{Ru}$ . Applying the constraints of the Sabatier-Gibbs model reduce the catalytic rate with orders of magnitude from the top of volcano and to the right. This results in a shift in the catalytic activity ranking:  $\text{Pd} > \text{Pt} > \text{Rh} > \text{Ru} > \text{Ag} > \text{Au}$ .

In Figure 11 the Sabatier-Gibbs volcano is presented together with the experimental volcano. The Sabatier-Gibbs model describes the trend in catalytic activity through the transition metals quite well. Gervasini *et al.* [37] studied the catalytic activity of a number of transition metals (Pt, Pd, Rh and Ru) for the NO decomposition experimentally. They found platinum to be the most active catalyst and the order of activity  $\text{Pt} > \text{Rh} > \text{Ru} > \text{Pd}$ . However the experiments were performed under different experimental conditions from this study.

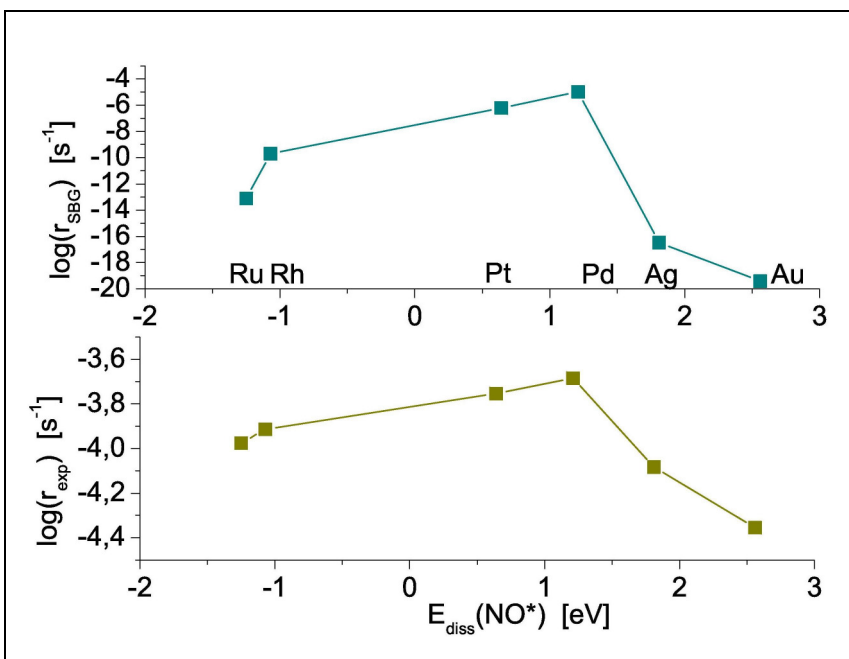


**Figure 11** The modelled decomposition rate versus experimental results for a range of different transition metal surfaces

While the model is designed to investigate trends and cannot be viewed as quantitative, it is noteworthy that the most active transition metal, palladium is within a factor of ten from the experimental activity. However, the model is not able to quantitatively predict the decomposition rate on the two sides of the volcano curve. For the noble metals, silver

and gold, on the right side of the volcano, the rate is underestimated by several orders of magnitude. However, the experimental activities are close to, what is observed for a blank sample.

### 5.3.4 Finding the optimal catalyst

An optimal catalyst for direct NO decomposition would be a surface that facilitates fast dissociation of NO and at the same time desorbs oxygen and nitrogen easily. In Figure 12 the theoretically calculated Sabatier-Gibbs direct NO decomposition rate is shown as a function of the dissociative chemisorption energies of  $N_2$  and  $O_2$ . It shows a 2-dimensional volcano with a maximum. Also the DFT-calculated reaction energies for the elemental metals are shown.

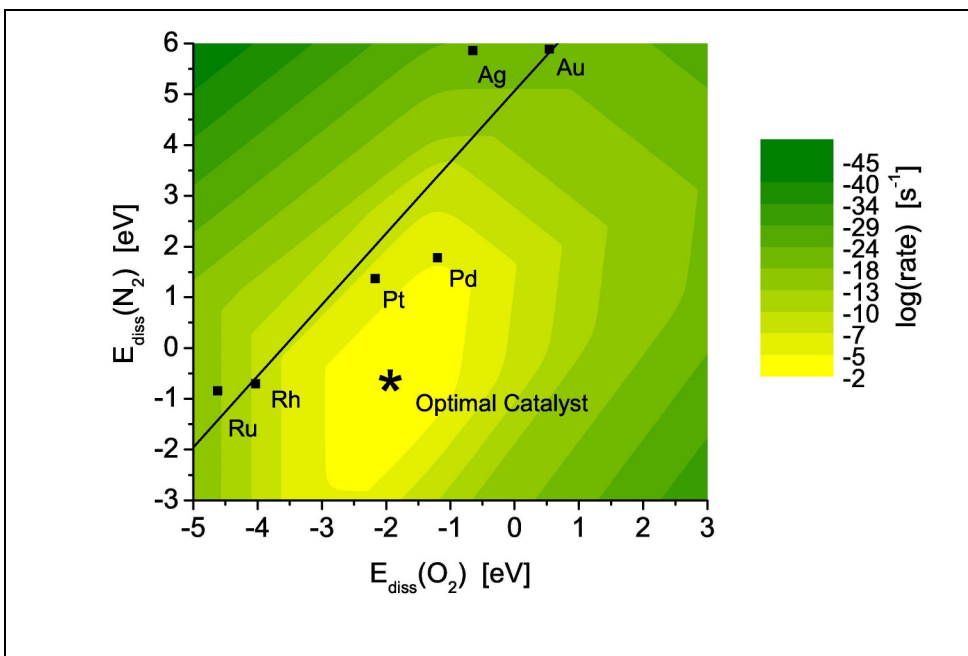


**Figure 12** The Sabatier-Gibbs activity is illustrated in green scale contours as a function of the dissociative chemisorption energies of  $O_2$  and  $N_2$ . The dissociation energy for NO is determined from its correlation with  $E_{\text{diss}}(O_2)$ . The positions of the transition metals from DFT calculations are indicated in the figure.

The dissociation energy of NO, necessary to construct the volcano, has been determined from the good linear correlation to the dissociation energy of  $O_2$ . It is interestingly observed that the line  $N_2$  and  $O_2$  dissociative chemisorption fitting the DFT point lays several eV above the optimal point of the two-dimensional volcano. However, since the dissociative chemisorption energy for these species is linearly related, no such transition

metal catalyst can be found. This suggests that one needs to look into entirely different classes of materials in order to find appropriate direct NO decomposition catalysts, and that a more appropriate class of materials should have the property that nitrogen and oxygen binds with a more equal strength to the surface.

## **5.4 Conclusion**

We have established a simple first-principle microkinetic analysis. The linear scaling relations enables us to describe the catalytic NO decomposition rate with just one descriptor for the catalytic activity. We have shown a good qualitative agreement between the experimental catalytic activities and the Sabatier-Gibbs activities of the transition metals in direct NO decomposition. The model enables us to understand the volcano curve for the direct NO decomposition where the activity is on one side limited by the ability to dissociate NO and on the other side the associative desorption of oxygen. Further we obtained from the Sabatier-Gibbs model an activity trend for the NO decomposition on stepped metal surfaces:  $\text{Pd} > \text{Pt} > \text{Rh} > \text{Ru} > \text{Ag} > \text{Au}$ . Furthermore the model clearly points out that the optimal catalyst for direct decomposition must be found in another kind of materials. The adsorption of oxygen is simply too strong compared to the adsorption of nitrogen and the linear relation between the adsorption energies prevents us from finding a transition metal close to the top of the volcano.

## Chapter 6

### Catalytic activity of surfaces and nanoparticles for CO oxidation

This chapter is based on the references [38, 39]. We here study trends in catalytic activity for the CO oxidation reaction on nanoparticles and extended surfaces. The CO oxidation reaction,  $\text{CO} + \frac{1}{2}\text{O}_2 \leftrightarrow \text{CO}_2$ , is regarded as the simplest and most general reaction for studying the activity of oxidation catalysts. For these reasons it is well studied both experimentally [40, 41, 42, 43, 44, 45, 46, 47, 48, 49, 50] and theoretically [51, 52, 53, 54, 55, 56, 57].

We start out by showing that gold nanoparticles are the best catalysts among the transition and noble metals for CO oxidation at low temperatures. We also show that platinum is the best catalyst for the closedpacked surfaces at elevated temperatures and gold is practically inactive. In order to understand the enhanced catalytic activity of small gold particles we compare the catalytic activity of the nanoparticles with the catalytic activity for higher coordinated extended surfaces; closed-packed, stepped and surfaces with kinks and discuss the origin of the “nano-effect”.

The study is based on combining DFT calculations on the full reaction pathway with microkinetic modeling within the framework of the “Sabatier Analysis”. We obtain scaling relations between adsorption energies of the reaction intermediates and between adsorption and transition state energies for the elementary reactions. This enables us to model the CO oxidation rate by limiting the numbers of independent variables within the microkinetic model.



## 6.1 Introduction

Gold is traditionally considered among the most noble metals [17], where even  $O_2$  does not adsorb [58]. Therefore it was a surprise, when Haruta *et al* in 1987 [59] showed that gold nanoparticles smaller than 5 nm are catalytically very active for the CO oxidation reaction below room temperature. The reasons for the enhanced catalytic activity of gold nanoparticles are widely debated. The explanations include quantum size effects [45], charge transfer [60, 61, 62, 63], support interactions [64, 65, 59], and the role of low coordinated sites [51, 54, 66, 67, 68, 69, 70]. The enhanced catalytic activity is not only interesting for the CO oxidation reaction. Also gold nanoparticles have shown to be active catalysts for acetylene hydrochlorination [71], alcohol oxidation to acids [72, 73] and aldehydes [74], and direct formation of hydrogen peroxide [75].

One special thing about nanoparticles is their large relative fraction of low coordinated corner atoms to surface atoms [55, 54, 76, 51]. The fraction of low coordinated sites at a given nanoparticle depends on the size and the shape of the particle. In Figure 13 the fraction of corner (CN=6), edge (CN=7) and surface atoms (CN=8 or 9) on a nanoparticle shaped as the top half of an octahedron is shown for decreasing particle size.

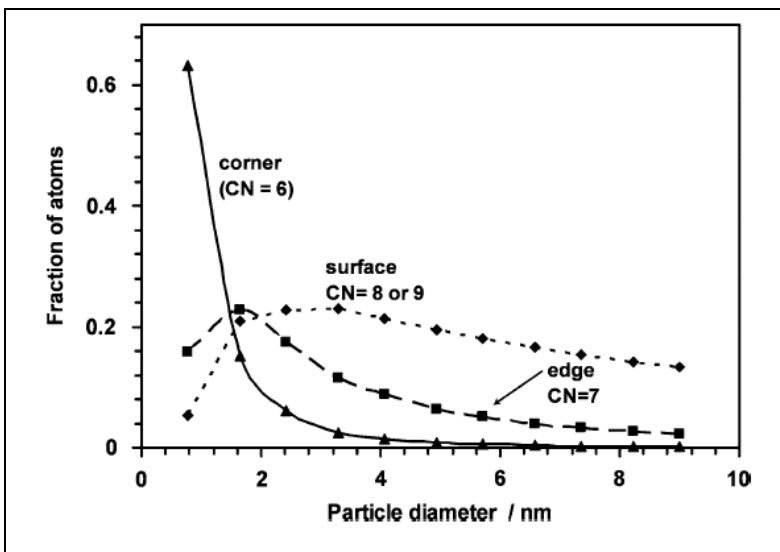


**Figure 13** Calculated fractions of atoms at corners, edges, and faces in uniform nanoparticle. Adapted from ref. [55]

Clearly the amount of low coordinated sites increases rapidly for nanoparticles with diameters less than 5 nm; whereas the fraction of high coordinated surface metal atoms is more or less constant for particles with diameters above 2 nm. In Figure 14 a compilation of data of the CO oxidation activities at 273 K on gold nanoparticles as a function of the particle size is presented. The data are from experimental studies [77, 78, 79, 80, 54, 47, 81, 82, 83, 84, 85].

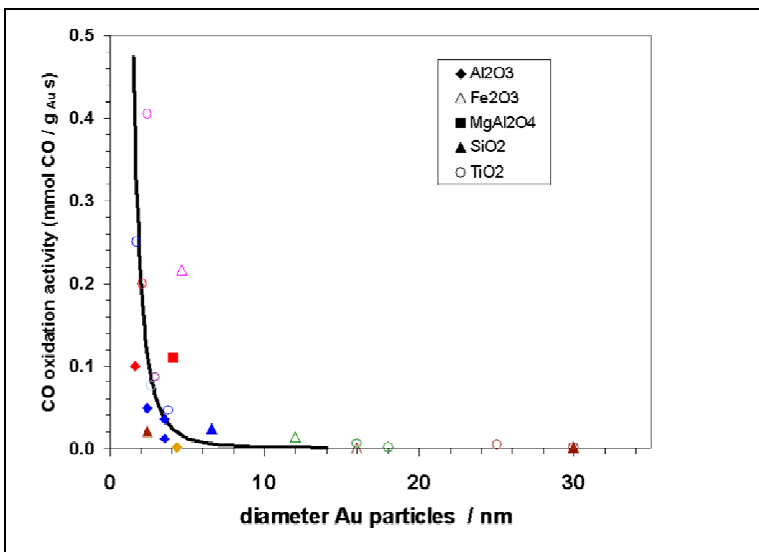


**Figure 14** Reported catalytic activities for CO oxidation at 273 K over different Au-based catalysts as a function of the Au particle size. Adapted from ref. [54]

Obviously the catalytic activity of gold particles is very dependent on the size of the nanoparticle. This is clear experimental evidence that the particle size of gold is an important parameter for the catalytic activity of supported catalysts. It is also observed that the catalytic activity depends on the choice of support, however to a minor extent. The black line is the calculated fraction of corner sites from Figure 13. From this it is evident, that there is a strong correlation between the fraction of low coordinated corner sites and the catalytic activity of gold nanoparticles.

## 6.2 Method

### 6.2.1 Computational details

Adsorption, transition state, and gas phase energies are calculated using the plane wave DFT code DACAPO [15]. Kohn-Sham one-electron valence states are expanded in a basis of plane waves with kinetic energies up to 30 Ry. Vanderbilt nonlocal ultrasoft pseudopotentials are used to describe the core electrons [16]. The exchange-correlation (xc)-energy is described employing the RPBE generalized gradient correction self-consistently. [15] For all surfaces, a  $6 \times 6 \times 1$  Monkhorst-Pack k-point sampling in the irreducible Brillouin zone was used. The occupation of the one electron states was calculated at a temperature of  $k_B T = 0.1$  eV, and all energies were extrapolated to  $T = 0$  K. Lattice constants have been determined by separate calculations on the bulk metals. The (111) surfaces were modeled by  $(2 \times 2)$  surface unit cells with slab thicknesses of four layers and the two topmost layers were allowed to fully relax. The (211) and (532) surfaces were modeled by  $(2 \times 1)$  and  $(1 \times 1)$  surface unit cells, respectively, with three close packed layer slabs, where only the topmost layer was allowed to relax. For all types of surfaces, the neighboring slabs are separated by more than  $10 \text{ \AA}$  of vacuum. For the M12 cluster structure,  $\Gamma$  point calculations were performed within unit cells with more than  $10 \text{ \AA}$  of vacuum between structures, with a Fermi temperature of  $k_B T = 0.01$  eV. All of the atoms in the 12 atom clusters were kept fixed in order to mimic the geometrically constrained corner of a larger particle with a lattice constant corresponding to the bulk value.

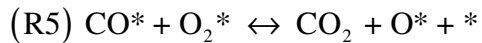
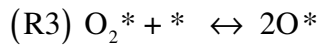
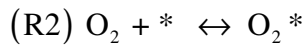
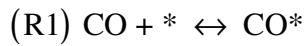
We have included energy corrections for the adsorption of CO to avoid the overbinding of CO by DFT, which yields lower binding energies on bridge sites than atop sites, in contradiction to experiment [86]. Oxygen adsorption energies are calculated relative to the  $O_2$  energy from  $H_2O$  splitting using the experimental reaction energy and that for  $H_2$  and  $H_2O$  in the gas phase [87]. This avoids difficulties associated with a DFT treatment of the triplet state of gas phase  $O_2$  [88].

### 6.3 Microkinetic modeling

We here describe the microkinetic models employed for the CO oxidation reaction. First a detailed description of a simplified kinetic treatment within the “Sabatier analysis” is given. Next the analytical steady state solution is described. The steady state solution is for used for validation of the Sabatier rate.

#### 6.3.1 The Sabatier Analysis

The CO oxidation is assumed to take place via the following reaction steps:



The reaction mechanism presents two possible routes for formation of  $\text{CO}_2$ . In the first route the oxidation of CO happens after  $\text{O}_2$  is dissociated, where the second route to CO oxidation takes place via associatively oxidation by  $\text{O}_2$ . The single adsorbed oxygen left over will react with CO following the last half of the first route. This is illustrated in Figure 15.

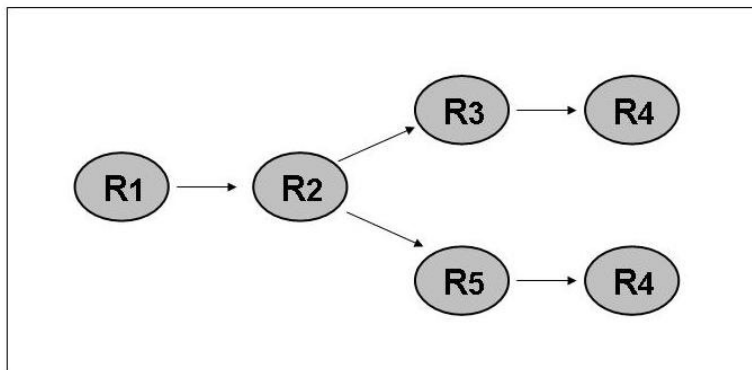


**Figure 15** Schematics of  $\text{CO}_2$  formation pathways

Here we assume that reactions (R1) and (R2) have reached equilibrium. The net-rates for these adsorption steps are therefore  $r_1 \approx r_2 \approx 0$ . Overall the Sabatier rate for the CO<sub>2</sub> production is the sum of the rates for reaction (R4) and (R5). However reaction (R4) is limited if there is no atomic oxygen present on the catalyst from reaction (R3) or reaction (R5). On the other hand reaction (R5) will be limited if by poisoning of oxygen on the catalyst, and therefore it can not be faster than (R4).

The overall reaction rate according to the Sabatier analysis is then:

$$r_s = \max \left\{ 2 \min \{ r_5, r_4 \}, \min \{ 2r_3, r_4 \} \right\} \quad (49)$$

The rates for elementary reactions (R3)-(R5) are maximized if we only consider the forward reactions:

$$r_3 = \theta_{O_2} \theta_* k_3^+ \quad (50)$$

$$r_4 = \theta_O \theta_{CO} k_4^+ \approx \theta_{CO} k_4^+ \quad (51)$$

$$r_5 = \theta_{O_2} \theta_{CO} k_5^+ \quad (52)$$

Where  $\theta_{CO}$ ,  $\theta_{O_2}$ ,  $\theta_O$  and  $\theta_*$  are the coverages of CO, O<sub>2</sub>, O and free surface sites respectively. The activation barriers are obtained from  $E_{ai} = \max \left[ (E_{TS} - E_{IS}, 0) \right]$ , where  $E_{TS}$  is the transition state energy and  $E_{IS}$  the initial state energy. Adsorption and transition state energies are given with respect to the gas phase molecules. The gas phase entropies are taken from ref. [89]. For elementary reaction (R4) we make the further assumption that the rate is independent of the coverage of atomic oxygen, which still makes it an upper bound.

Since reactions (R1) and (R2) are assumed to be in equilibrium the surface activities,  $\lambda_i$ , of CO and O<sub>2</sub> satisfy  $\lambda_{CO} = K_1 p_{CO}$  and  $\lambda_{O_2} = K_2 p_{O_2}$  respectively. From the conservation of

sites,  $\sum \theta_x = 1$ , we can express the coverage of free surface sites from the surface activities of the adsorbed species:

$$\theta_*^{\max} = 1 / (1 + \lambda_{\text{CO}} + \lambda_{\text{O}_2}) = 1 / (1 + K_1 p_{\text{CO}} + K_2 p_{\text{O}_2}) \quad (53)$$

We have neglected the coverage of surface oxygen. Note that this assumption makes the surface coverages an upper bound. The coverages of the reaction intermediates and the forward rate constants, hence The Sabatier rate, is fully determined from the six metal-dependent parameters:  $E_{\text{CO}}$ ,  $E_{\text{O}_2}$ ,  $E_{\text{O}}$ ,  $E_{\text{TS}_3}$ ,  $E_{\text{TS}_4}$  and  $E_{\text{TS}_5}$ .

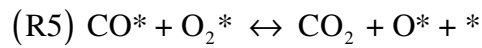
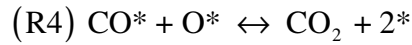
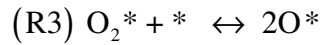
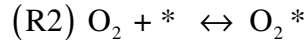
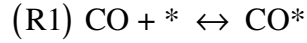
For the (111)-surfaces the  $\text{CO}^* + \text{O}_2^* \leftrightarrow \text{CO}_2 + \text{O}^* + *$  is neglected, due to a weak bonding of  $\text{O}_2$  combined with the reaction barrier for the process makes it unimportant for platinum [90] and less reactive metals.[91]. The Sabatier rate for producing  $\text{CO}_2$  is the minimum of the rates for elementary reaction (R3) and (R4):

$$r_s = \min \{2r_3, r_4\} \quad (54)$$

The Sabatier rate for the CO oxidation reaction on (111) surfaces are now fully determined from the five parameters:  $E_{\text{CO}}$ ,  $E_{\text{O}_2}$ ,  $E_{\text{O}}$ ,  $E_{\text{TS}_3}$  and  $E_{\text{TS}_4}$ .

### 6.3.2 The analytical steady state solution

We here set up an analytical solution based on the assumption that the system has reached steady state. At steady state the coverage of the adsorbed species does not change in time. Again we consider the following elementary steps in the CO oxidation reaction:



The CO oxidation rate is the rate of forming  $\text{CO}_2$ . The  $\text{CO}_2$  forming steps are R4 and R5 and the  $\text{CO}_2$  oxidation rate is  $r_{\text{CO}_2} = r_4 + r_5$ .

The rates for the adsorption of CO and O are:

$$r_1 = k_1^+ p_{\text{CO}} \theta_* - k_1^- \theta_{\text{CO}} \quad (55)$$

$$r_2 = k_2^+ p_{\text{O}_2} \theta_* - k_2^- \theta_{\text{O}_2} \quad (56)$$

Since reactions (R1) and (R2) are assumed to be in equilibrium the surface activities,  $\lambda_i$ , of CO and  $\text{O}_2$  satisfies  $\lambda_{\text{CO}} = K_1 p_{\text{CO}}$  and  $\lambda_{\text{O}_2} = K_2 p_{\text{O}_2}$ .

The rates for the elementary reactions R3-R5 are:

$$r_3 = k_3^+ \theta_{\text{O}_2} \theta_* - k_3^- \theta_{\text{O}}^2 = x_3 \theta_*^2 - y_3 \theta_{\text{O}}^2 \quad (57)$$

$$r_4 = k_4^+ \theta_{\text{CO}} \theta_{\text{O}} - k_4^- p_{\text{CO}_2} \theta_*^2 = x_4 \theta_* \theta_{\text{O}} - y_4 \theta_*^2 \quad (58)$$

$$r_5 = k_5^+ \theta_{\text{O}_2} \theta_{\text{CO}} - k_5^- p_{\text{CO}_2} \theta_{\text{O}} \theta_* = x_5 \theta_*^2 - y_5 \theta_{\text{O}} \theta_* \quad (59)$$

To simplify the expressions the constants  $x_i$  and  $y_i$ ,  $i=3,4,5$  have been defined.

Since we are at steady state the coverage of the intermediates are conserved. Therefore:

$$R(O^*) = 0 \Rightarrow 2r_3 - r_4 + r_5 = 0 \quad (60)$$

By solving the second order equation obtained from inserting equations (57)-(59) in equation (60), and noting that all constants,  $x_i$  and  $y_i$ , and the coverages are positive we obtain:

$$\theta_o = \frac{-B \pm \sqrt{D}}{2A} = \theta_* \left( \frac{x_4 + y_5}{4y_3} \left( -1 + \sqrt{1 + \frac{8y_3(2x_3 + y_4 + x_5)}{(x_4 + y_5)^2}} \right) \right) \quad (61)$$

We define the constant W as  $\theta_o = \theta_* W$ . Using the sum-rule  $\theta_* + \theta_o + \theta_{CO} + \theta_{O_2} = 1$ , we can now calculate  $\theta_*$ :

$$\theta_* = \frac{1}{1 + W + K_1 p(CO) + K_2 p(O_2)} \quad (62)$$

Thereby we have expressions for the surface coverages of each reaction intermediate and the coverage of empty site.



## 6.4 Results

We start out by studying the CO oxidation reaction on a corner model of a larger nanoparticle for a number of transition and noble metals.

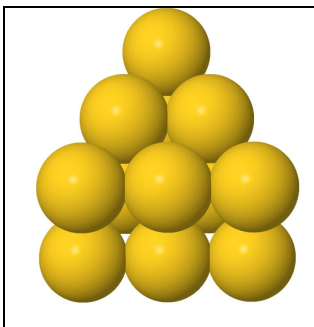


**Figure 16** Schematics of the corner model of a nanoparticle

We compare the catalytic activity of the corner model with the catalytic activity for closed-packed surfaces. We show how scaling relations between adsorption energies, and between adsorption and transition state energies ((BEP) relations) limit the number of independent variables characterizing a particular metal and structure to  $E_O$  and  $E_{CO}$ . For the closed-packed surfaces, we show that platinum is the most active transition metal for CO oxidation at high temperature conditions and that at low-temperature conditions the gold is the most active of the metal nanoparticles.

### 6.4.1 Scaling relations

The goal is to use the calculated adsorption energies and activation energies for the CO oxidation reaction to study trends in catalytic rates. Therefore we begin by studying trends in these energies.

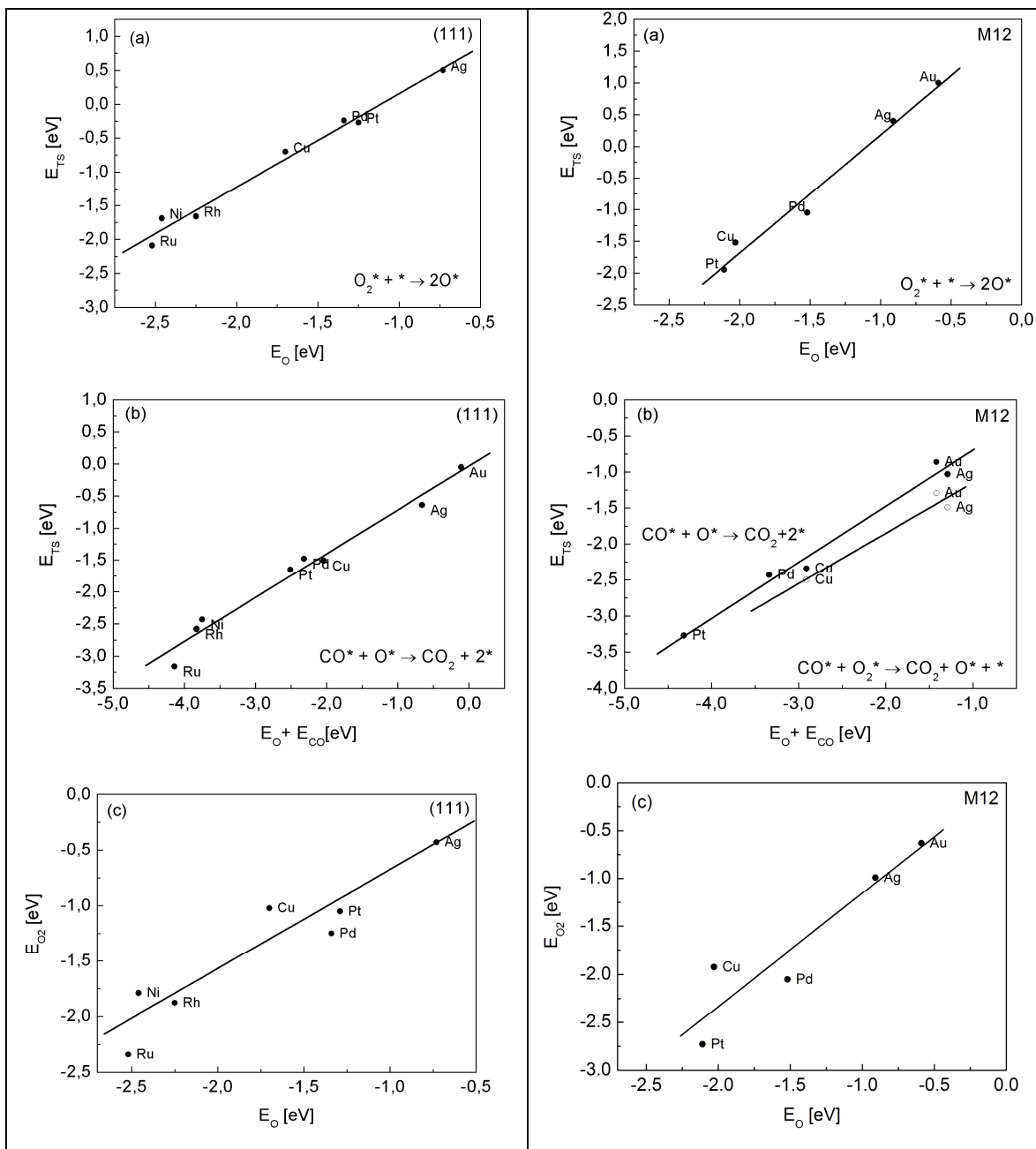


**Figure 17** The scaling and BEP relations for (111) surfaces and M12 clusters (a) Calculated transition state energies for  $O_2$  dissociation  $E_{TS3}$  (R3) as a function of O adsorption energy  $E_O$ . (b) Calculated transition state energies for adsorbed CO reacting with adsorbed O,  $E_{TS4}$  (R4), as a function of the sum of the O and CO adsorption energies,  $E_O + E_{CO}$ . For the M12 clusters also calculated transition state energies for adsorbed CO reacting with adsorbed  $O_2$ ,  $E_{TS5}$  (R5), as a function of the sum of the O and CO adsorption energies,  $E_O + E_{CO}$  (c) The scaling of the  $O_2$  adsorption energy,  $E_{O_2}$ , with the O adsorption energy,  $E_O$ .

In Figure 17 we present the scaling and BEP relations obtained for the CO oxidation reaction on the M12 clusters and for the (111) surfaces. For the both the (111) surfaces and M12 corner model, BEP-relations for the dissociation of  $O_2$  and the  $CO + O$  reaction,

are presented. Also a linear scaling between the adsorption energy of  $O_2$ ,  $E_{O_2}$ , and the adsorption energy of  $O$ ,  $E_O$ , is presented. Note that for the corner models we also present the BEP relation for the  $CO + O_2$  reaction.

The scaling and BEP relations on the two types of structures, (111) surfaces and M12 corner models, are similar. However the energy axis has shifted and the adsorption of  $CO$ ,  $O$  and  $O_2$  are all substantially stronger on the M12 corner model than on the (111) surfaces. In fact oxygen binds about 0.5 eV stronger on the M12 corner model than on the extended (111) surfaces. The same trend is seen for molecular adsorption of  $CO$  and  $O_2$ . This is in agreement with Lopez *et al* [54]. They found that the adsorption energy of  $O$  and  $CO$  increase significantly from the adsorption on a gold closed packed surface to a gold nanoparticle. The obtained linear relations, shown in Figure 21, mean that of the original six (five for (111) surfaces) metal-dependent variables;  $E_{CO}$ ,  $E_{O_2}$ ,  $E_O$ ,  $E_{TS3}$ ,  $E_{TS4}$ , and  $E_{TS5}$ , only two are independent. We choose  $E_{CO}$  and  $E_O$  as descriptors of the catalytic activity. In Chapter 6.4.2 we show the catalytic activity of the M12 clusters and the (111) surfaces for the  $CO$  oxidation reaction as a function of the adsorption energy of  $O$ ,  $E_O$ , and the adsorption energy of  $CO$ ,  $E_{CO}$ .

## 6.4.2 Volcanoes

In Figure 18 we present a two dimensional volcano plot of the Sabatier activity for CO oxidation on closed packed surfaces versus the descriptors,  $E_O$  and  $E_{CO}$ , for high temperature conditions ( $T=600$  K,  $P_{O_2}=0.33$  bar and  $P_{CO}=0.67$  bar). The Sabatier activity is given as  $A_S = k_B T \ln \left[ r_S / (k_B T h^{-1}) \right]$ , where  $r_S$  is the Sabatier rate.

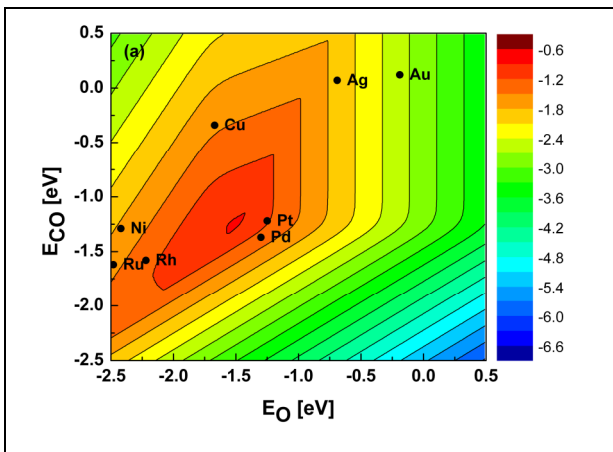


**Figure 18** Contour plot of the Sabatier activity over (111) as a function of  $E_{CO}$  and  $E_O$  under high temperature conditions. The values for the transition and noble metals are indicated.

The result is a two-dimensional volcano shows that of the elemental metals platinum and palladium are closest to the maximum of the volcano. This agrees very well with experimental evidence [92]. Furthermore Grabow *et al* [93] have shown that for low temperature CO oxidation Pt without strain has a higher activity than either compressed (weaker bond energies) or expanded (stronger bond energies) Pt surfaces. The catalytic activity of gold and silver extended surfaces is very low.

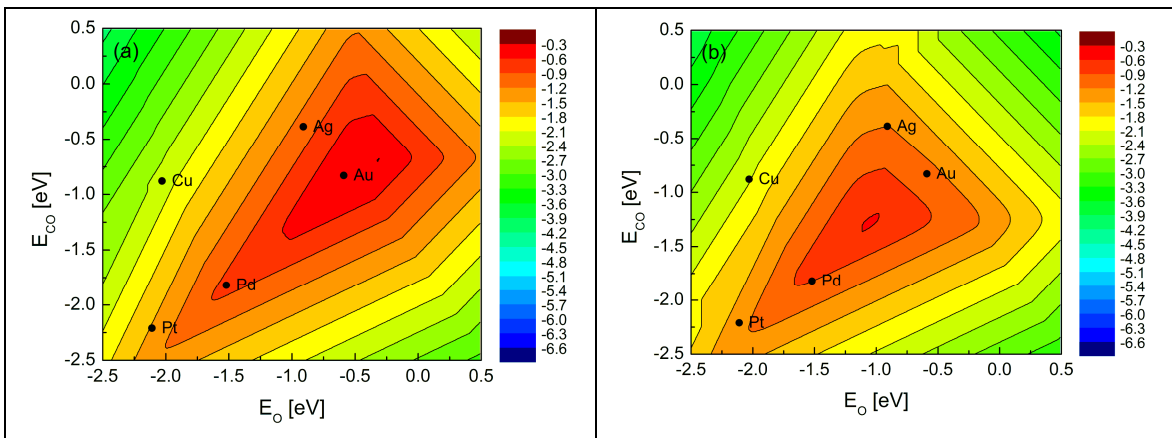


**Figure 19** Contour plot of the Sabatier rate as a function of the CO and O adsorption energies on the 12-atom clusters. The values for some elemental metals are shown. (a) is the activity under typical experimental conditions for CO oxidation by gold nanoparticles ( $T=273\text{ K}$ ,  $P_{O_2}=0.21\text{ bar}$  and  $P_{CO}=0.01$ ) and (b) is the activity under high temperature conditions ( $T=600\text{ K}$ ,  $P_{O_2}=0.33\text{ bar}$  and  $P_{CO}=0.67\text{ bar}$ ).

In Figure 19(a) we present the Sabatier activity for the CO oxidation on the M12 corner models at low temperature conditions ( $T=273\text{ K}$ ,  $P_{O_2}=0.21\text{ bar}$  and  $P_{CO}=0.01$ ). For the nanoparticles gold is at the pinnacle, followed by palladium and silver. The obtained trends in catalytic activity for the closed-packed surfaces and the M12 clusters in Figure 18 and Figure 19, are in good agreement with available experimental observations [59, 76]. It shows that we are able to estimate trends in activities for different metals from combining DFT with micro-kinetic modeling.

When comparing the volcanoes in Figure 18 and Figure 19 we see that the catalytic activity of Au nanoparticles is many orders of magnitudes larger than for the Au closed-packed surface. Therefore the gold corner atoms will dominate over the closed-packed surface even for quite large particles. On the other hand for Pt the catalytic activity for the closed-packed surface is about an order of magnitude larger than for the corner atoms on the nanoparticle. Note that the small Pt nanoparticles can still be more active, because the surface area for catalysis is larger than for surfaces.

And most importantly, the adsorption energy for the reaction intermediates shift substantially depending on the surface structure. This is true for all the metals considered and it is the dominant reason for gold becoming the best elemental catalyst for the low coordinated sites. The shift is of the same order of magnitude as the difference between

neighboring metals in the Periodic Table explaining, why it appears as if the top of the volcano has shifted by a little less than one place to the right from Figure 18 and Figure 19.

The present analysis suggests that the more noble metals move to the maximum in the volcano, when lower coordinated metal atoms are as active sites for the reaction. The volcanoes give us a clear picture of which catalyst properties, in terms of adsorption energies of CO and O, we should chase in order to obtain the best catalyst.

### 6.5 Validation of the microkinetic model

In order to validate the micro-kinetic model in chapter 6.3.1 we set up an analytical steady-state solution. In Figure 20 we show the Sabatier volcano and the volcano for the analytical solution for the CO oxidation on nanoparticles at low temperatures. The simplified Sabatier model describes the trends in catalytic activity in good agreement with the analytical solution.

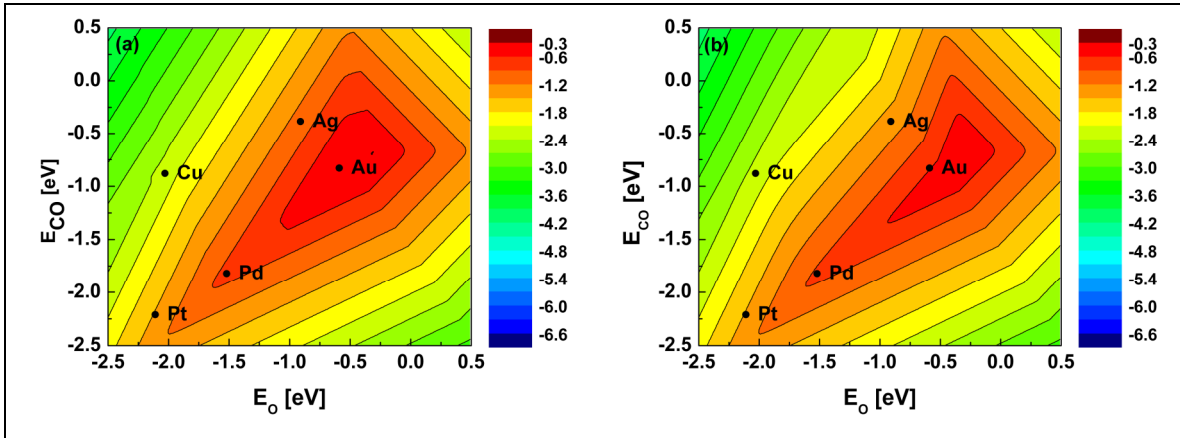


**Figure 20** Contour plot of the catalytic Activity  $A=k_B T \ln \left( r/k_B T h^{-1} \right)$  in eV for nanoparticles

$\left( T=273 \text{ K}, p_{O_2}=0.21 \text{ bar}, p_{CO}=0.01 \text{ bar} \right)$  (a) The Sabatier Activity and (b) The Steady State Activity.

The simplified Sabatier volcano is for all data points an upper bound to the analytical solution.

## 6.6 The complete picture

In the previous part we showed that we are able to estimate trends in the catalytic activity of the CO oxidation reaction from combining DFT with microkinetic modeling. We found that gold is the catalytic most active nanoparticle, due to a significant stronger binding on the M12 clusters than on the closed-packed surfaces, and that Pt is the most catalytic active for the closedpacked surfaces at high temperatures.

We now complete the picture by including the stepped and kinked surfaces to our analysis. By doing so, we have a unique chance to study the role of surface structure and the role of low-coordinated sites, in this study for the CO oxidation reaction, and to analyze the origin of the “nanoeffect”.

## 6.6.1 Scaling Relations

In Figure 21a-d, scaling relations obtained for the CO oxidation reaction on the different surface structures of transition and noble metals are shown.

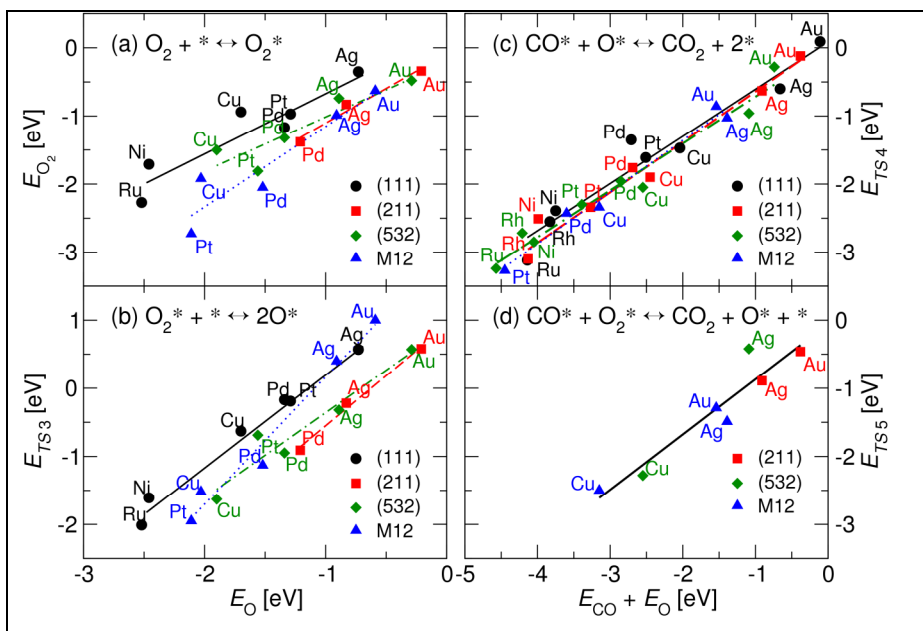


**Figure 21** The scaling and BEP relations for (111) surfaces (black), (211) surfaces (red), (532) surfaces (green), and M12 clusters (blue). (a) The scaling of the  $O_2$  adsorption energy,  $E_{O_2}$ , with the O adsorption energy  $E_O$ . (b) Calculated transition state energies for  $O_2$  dissociation ETS<sub>3</sub> (R3) as a function of O adsorption energy  $E_O$ . (c) Calculated transition state energies for adsorbed CO reacting with adsorbed O ETS<sub>4</sub> (R4) as a function of the sum of the O and CO adsorption energies,  $E_O + E_{CO}$ . (d) Calculated transition state energies for adsorbed CO reacting with adsorbed  $O_2$ , ETS<sub>5</sub> (R5) as a function of the sum of the O and CO adsorption energies,  $E_O + E_{CO}$ , with surface averaged BEP relation.

In Figure 21 BEP-relations for the dissociation of  $O_2$  (R3), the CO + O reaction, (R4) and the CO +  $O_2$  reaction (R5), are presented for all the surface structures and the M12 corner model. Also a linear scaling between the adsorption energy of  $O_2$ ,  $E_{O_2}$ , and the adsorption energy of O,  $E_O$ , is shown for the different structures.

In general, the data falls into families of linear relations, with one linear relation for each structure of the catalyst. The differences in the BEP-lines show the structure dependence of the different adsorption energies and transition state energies. For the CO + O and CO +  $O_2$  reactions the BEP-relations fall on the same line. There are still large differences in



the adsorption and activation energies, but the move along the general BEP line.  
Therefore the structure dependence of the catalytic activity is mainly electronic in nature.

## 6.6.2 Volcanoes

The Sabatier activity is here presented for (111), (211) and (532) surfaces together with the Sabatier activity for the M12 corner model. In the microkinetic model we here also include the BEP-relation for elementary reaction (R5) for the closedpacked surfaces and use the general BEP-relation obtained from Figure 21d. Therefore volcano for the (111) surfaces differ slightly from Figure 18.

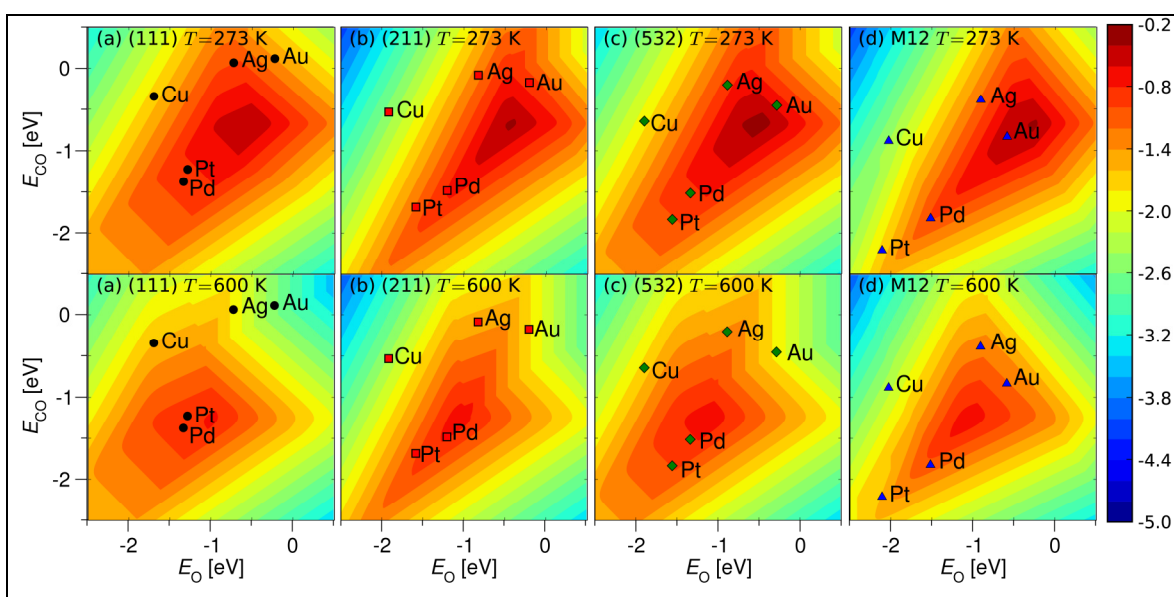


**Figure 22** Contour plot of the catalytic Activity  $A = k_B T \ln(r/k_B \text{Th}^{-1})$  in eV (top) low temperature ( $T = 273 \text{ K}$ ,  $p_{\text{O}_2} = 0.21 \text{ bar}$ ,  $p_{\text{CO}} = 0.01 \text{ bar}$ ) and (bottom) high temperature ( $T = 600 \text{ K}$ ,  $p_{\text{O}_2} = 0.33 \text{ bar}$ ,  $p_{\text{CO}} = 0.67 \text{ bar}$ ), as a function of the CO and O adsorption energies on the (a) (111) surfaces (b) (211) surfaces (c) (532) surfaces and (d) M12 clusters. The values for the elemental metals are shown.

First we note that the Sabatier volcano for the different geometries does not change substantially. However the CO oxidation rate for the elemental metals is a function of the surface geometry. This is caused by a shift to stronger binding energies of the reaction intermediates going from (111)  $\rightarrow$  (211)  $\rightarrow$  (532)  $\rightarrow$  M12 sites. For Au, Ag and Cu this leads to a significant increase in the catalytic activity, most pronounced for Au. This is in good agreement with experimental observations [94]. The opposite picture is true for Pd and Pt; here the closed-packed surfaces are the most active. The binding of the reaction intermediates is simply too strong on the nanoparticle.

Also observed from Figure 22 it is clear that an increase in temperature shifts the top of the volcano to stronger adsorption energies, hence in the direction of the platinum metals.

In summary, at the low temperature conditions the Au particles are the most active. At higher temperatures the CO oxidation is highest on the closed-packed surfaces of Pd and Pt. The volcano functions for the different structures in Figure 22 are not very different, and hence the shift in catalytic activity for the elemental metals is not a geometrical effect. It is connected to the variation in the adsorption energy of the intermediates as the structure is changed.

### 6.6.3 Electronic structure effect

It was shown above that the structure induced change in the catalytic activity for CO oxidation on transition metals and noble metals is determined by the structure dependence on the adsorption strength.

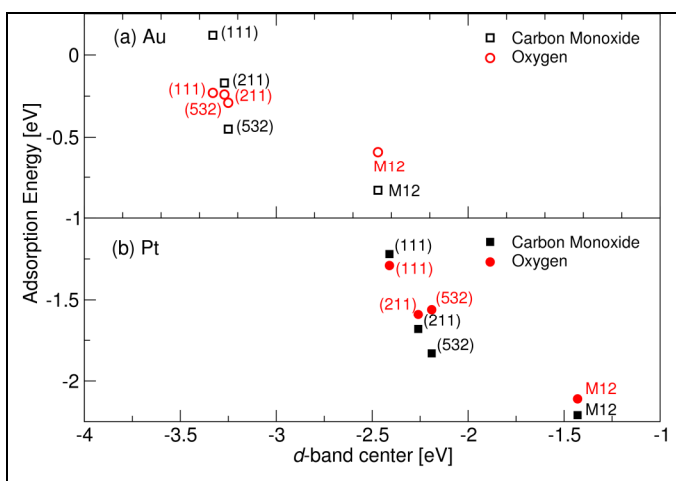


**Figure 23** Adsorption energy  $E_{CO}$  and  $E_O$  versus d-band center for (111) surfaces, (211) surfaces, (532) surfaces, and M12 clusters of

In Figure 23 we show the variation in the adsorption energy of CO and O against the d-band center of the surface atoms. In general we expect low-coordinated surface atoms to have higher lying d-states and be more reactive than highly coordinated surface atoms.

This is also the picture we see in Figure 23 for both the Pt and the Au. The d-band center shifts up and the adsorption of CO and O are stronger on the low-coordinated sites. This is in agreement with the d-band model described in Chapter 3.2.

## 6.7 Conclusion

We have studied the trends in catalytic CO oxidation over a range of metal surfaces by combining DFT and microkinetic modeling. We have shown that the scaling relations between different adsorption energies ( $E_{\text{O}}$  and  $E_{\text{O}_2}$ ) and between activation energies and adsorption energies (BEP-relations) are structure dependent. By studying different close-packed, stepped and kinked surfaces as well as very small clusters, we have showed that the coordination number of the metal atoms at the active site is responsible for this structure dependence. We have also provided detailed evidence that this effect is electronic in nature: the low coordinated metal atoms that bind the reactants most strongly have the highest lying metal d states.

We found that the catalytic activity of gold increases strongly, when the metal coordination number of Au decreases. This provides part of the explanation for the unusual high catalytic activity of Au. The present analysis has identified the intrinsic structural effect associated with the metal for the CO oxidation reaction. This effect will always be present, but may be further augmented by additional effects, such as quantum size [45], charge transfer [60, 61, 62], support interactions [64, 65, 59].

In summary, the catalytic properties of nano-sized particles observed experimentally, were modeled. We analyzed the origin of this effect. The ability of the metal atoms to activate reactants change substantially as the coordination number of the active metal site is reduced at corners of metal particles.

## Summary and Outlook

In this thesis we have combined density functional theory calculations with microkinetic modeling to describe trends in catalytic activity of transition metals for the direct NO decomposition reaction and the CO oxidation reaction. From density functional theory calculations adsorption energies and transition state energies have been obtained. Linear scaling between adsorption energies of reaction intermediates and between transition state energies and adsorption energies have enabled us to describe catalytic activities with few descriptors; One for the NO decomposition and two for the CO oxidation.

First, an improved microkinetic model within The Sabatier Analysis, the Sabatier-Gibbs description of the surface coverage, was described. The Sabatier-Gibbs Analysis is restricted to reactions, where there is exactly one reactant and product channel for each reaction intermediate. It would be great to develop a simple kinetic framework similar to the Sabatier-Gibbs analysis, for reactions with parallel elementary reactions, like the CO oxidation reaction.

For the NO decomposition on stepped transition metal surfaces we obtained the following activity trend:  $\text{Pd} > \text{Pt} > \text{Rh} > \text{Ru} > \text{Ag} > \text{Au}$ . We also showed that for the more noble on the right leg of the volcano the NO dissociation reaction is rate limiting, whereas on the left leg the associative desorption of  $\text{O}_2$  limits the NO decomposition rate. Finally the 3D volcano showed that (211) transition metals bind oxygen too strongly compared to nitrogen and because of linear scaling between them, the optimal catalyst should be found in a different class of materials.

For the CO oxidation reaction on transition metal nanoparticles, kinks, steps and closed packed surfaces. We found that the catalytic activity of gold increases strongly, when the metal coordination number of Au decreases. This provides part of the explanation for the unusual high catalytic activity of Au. We showed that the coordination number of the metal atoms on the active site is responsible for the structural effects observed and that the active sites with the lowest coordinated metal atoms have the highest lying d-states. We concluded that the observed structural effect in CO oxidation on different catalyst

structures is electronic in nature. It is therefore possible that pronounced nano-effects in catalysis is not restricted to Au. For reactions with less reactive molecules, we would expect that the best nanoparticle catalysts would not be Au, but metals to the right in the Periodic table of the best extended surface catalyst. This opens up for the possibility of for enhancing the catalytic activity for all sorts of reactions by using nanoparticle catalysts.

## Bibliography

- [1] Smil, V. *Nature* **400**(6743), 415 JUL 29 (1999).
- [2] Lang, B., Joyner, R., and Somorjai, G. *Surf. Sci.* **30**(2), 454 (1972).
- [3] Kohn, W. *Rev. Mod. Phys.* **71**(5), 1253–1266 (1999).
- [4] Greeley, J., Norskov, J., and Mavrikakis, M. *Annual Review of Physical Chemistry* **53**, 319–348 (2002).
- [5] Bronsted, J. *Chem. Rev.* **5**(3), 231–338 (1928).
- [6] Evans, M. and Polanyi, M. *Trans. Far. Soc.* **34**(1), 0011–0023 (1938).
- [7] Parr, R. and Yang, W. *Density-Functional Theory of Atoms and Molecules*. Oxford University Press, (1989).
- [8] Dreizler, R. and Gross, E. *Density Functional Theory, An Approach to the Quantum Many-Body Problem*. Springer-Verlag, (1990).
- [9] Callaway, J. and March, N. *Solid State Physics - Advances in Research and Applications* **38**, 135–221 (1984).
- [10] Kohn, W., Becke, A., and Parr, R. *J. Phys. Chem.* **100**(31), 12974–12980 (1996).
- [11] <https://wiki.fysik.dtu.dk/dacapo>.
- [12] Born, M. and Oppenheimer, R. *Annalen der Physik* **84**(20), 0457–0484 (1927).
- [13] Hohenberg, P. and Kohn, W. *Phys. Rev. B* **136**(3B), 864 (1964).
- [14] KOHN, W. and SHAM, L. *Phys Rew.* **140**(4A), 1133 (1965).
- [15] Hammer, B., Hansen, L. B., and Nørskov, J. K. *Phys. Rev. B* **59**(11), 7413–7421 (1999).
- [16] Vanderbilt, D. *Phys. Rev. B* **41**(11), 7892–7895 (1990).
- [17] Hammer, B. and Nørskov, J. K. *Nature* **376**(6537), 238–240 (1995).
- [18] Hammer, B. and Nørskov, J. K. *Surf. Sci.* **343**(3), 211–220 (1995).
- [19] Hammer, B. and Nørskov, J. K. *Adv. Catal.* **45**, 71–129 (2000).
- [20] Bligaard, T. and Nørskov, J. K. *Electrochim. Acta* **52**(18), 5512–5516 (2007).
- [21] Nørskov, J. K., Bligaard, T., Logadottir, A., Bahn, S., Hansen, L. B., Bollinger, M., Benggaard, H., Hammer, B., Slijivancanin, Z., Mavrikakis, M., Xu, Y., Dahl, S., and Jacobsen, C. J. H. *J. Catal.* **209**(2), 275–278 (2002).
- [22] Sabatier, P. *Ber. Deutsch. Chem. Gesellschaft* **44**, 1984 (1911).

- [23] Bligaard, T., Nørskov, J. K., Dahl, S., Matthiesen, J., Christensen, C. H., and Sehested, J. *J. Catal.* **224**(1), 206–217 (2004).
- [24] Bligaard, T., Honkala, K., Logadottir, A., Nørskov, J., Dahl, S., and Jacobsen, C. *J. Phys. Chem. B* **107**(35), 9325–9331 (2003).
- [25] Falsig, H., Bligaard, T., Christensen, C., and Nørskov, J. *Pure Appl. Chem.* **79**, 1895 (2007).
- [26] Falsig, H., Bligaard, T., Rass-Hansen, J., Kustov, A., Christensen, C., and Nørskov, J. K. *Top. Catal.* **45**, 117 (2007).
- [27] Mahzoul, H., Brillhac, J., and Gilot, P. *Appl. Catal. B-Environ.* **20**(1), 47–55 (1999).
- [28] Armor, J. *Appl. Catal. B-Environ.* **1**(4), 221–256 DEC 15 (1992).
- [29] Burch, R., Breen, J., and Meunier, F. *Appl. Catal. B-Environ.* **39**(4), 283–303 DEC 20 (2002).
- [30] Busca, G., Lietti, L., Ramis, G., and Berti, F. *Appl. Catal. B-Environ.* **18**(1-2), 1–36 (1998).
- [31] Goralski, C. and Schneider, W. *Appl. Catal. B-Environ.* **37**(4), 263–277 (2002).
- [32] Ge, Q. and Neurock, M. *J. Am. Chem. Soc.* **126**(5), 1551–1559 (2004).
- [33] Liu, Z., Jenkins, S., and King, D. *J. Am. Chem. Soc.* **125**(48), 14660–14661 (2003).
- [34] Hammer, B. *Top. Catal.* **37**(1), 3–16 (2006).
- [35] Rempel, J., Greeley, J., Hansen, L. B., Nielsen, O. H., Nørskov, J. K., and Mavrikakis, M. *J. Phys. Chem. C* **113**(48), 20623–20631 (2009).
- [36] Rainer, D., Vesecky, S., Koranne, M., Oh, W., and Goodman, D. *J. Catal.* **167**(1), 234–241 (1997).
- [37] Gervasini, A., Carniti, P., and Ragaini, V. *Appl. Catal. B-Environ.* **22**(3), 201–213 (1999).
- [38] Falsig, H., Hvolbæk, B., Kristensen, I. S., Jiang, T., Bligaard, T., Christensen, C. H., and Nørskov, J. K. *Angew. Chem. Int. Ed.* **47**, 4835–4839 (2008).
- [39] Jiang, T., Mowbray, D. J., Dobrin, S., Falsig, H., Hvolbaek, B., Bligaard, T., and Nørskov, J. K. *J. Phys. Chem. C* **113**(24), 10548–10553 JUN 18 (2009).
- [40] Engel, T. and Ertl, G. *Adv. Catal.* **28**, 1 (1979).



- [41] Campbell, C. T., Ertl, G., Kuipers, H., and Segner, J. *J. Chem. Phys.* **73**, 5862 (1980).
- [42] Goodman, D. W. and Peden, C. H. F. *J. Phys. Chem.* **90**, 4839 (1986).
- [43] Xu, J. Z. and Yates, J. T. *J. Chem. Phys.* **99**, 725 (1993).
- [44] Szanyi, J. and Goodman, D. W. *J. Chem. Phys.* **114**, 6382 (2001).
- [45] Valden, M., Lai, X., and Goodman, D. W. *Science* **281**(5383), 1647–1649 (1998).
- [46] Chen, M. and Goodman, D. *Science* **306**(5694), 252–255 (2004).
- [47] Janssens, T. V. W., Carlsson, A., Puig-Molina, A., and Clausen, B. *J. Catal.* **240**(2), 108–113 (2006).
- [48] Xu, C., Su, J., Xu, X., Liu, P., Zhao, H., Tian, F., and Ding, Y. *J. Am. Chem. Soc.* **129**(1), 42–43 (2007).
- [49] Xu, C., Xu, X., Su, J., and Ding, Y. *J. Catal.* **252**(2), 243–248 (2007).
- [50] Grisel, R., Weststrate, K.-J., Gluhoi, A., and Nieuwenhuys, B. E. *Gold Bull.* **35**(2), 39–45 (2002).
- [51] Mavrikakis, M., Stoltze, P., and Nørskov, J. K. *Catal. Lett.* **64**(2), 101–106 (2000).
- [52] Reuter, K. and Scheffler, M. *Phys. Rev. B* **65**(3), 035406 (2002).
- [53] Liu, Z.-P., Hu, P., and Alavi, A. *J. Am. Chem. Soc.* **124**(49), 14770–14779 (2002).
- [54] Lopez, N., Janssens, T. V. W., Clausen, B. S., Xu, Y., Mavrikakis, M., Bligaard, T., and Nørskov, J. K. *J. Catal.* **223**(1), 232–235 (2004).
- [55] Janssens, T. V. W., Clausen, B. S., Hvolbæk, B., Falsig, H., Christensen, C. H., Bligaard, T., and Nørskov, J. K. *Top. Catal.* **44**(1–2), 15–26 (2007).
- [56] Broqvist, P., Molina, L., Gronbeck, H., and Hammer, B. *J. Catal.* **227**(1), 217–226 (2004).
- [57] Hellman, A., Klacar, S., and Groenbeck, H. *J. Am. Chem. Soc.* **131**(46), 16636 (2009).
- [58] Saliba, N. and Koel, B. E. *Surf. Sci.* **410**(2–3), 270–282 (1998).
- [59] Haruta, M., Kobayashi, T., Sano, H., and Yamada, N. *Chem. Lett.* (2), 405–408 (1987).
- [60] Ricci, D., Bongiorno, A., Pacchioni, G., and Landman, U. *Phys. Rev. Lett.* **97**, 036106 (2006).

- [61] van Bokhoven, J., Louis, C., Miller, J., Tromp, M., Safonova, O., and Glatzel, P. *Angew. Chem. Int. Ed.* **45**(28), 4651–4654 (2006).
- [62] Sanchez, A., Abbet, S., Heiz, U., Schneider, W., Hakkinen, H., Barnett, R., and Landman, U. *J. Phys. Chem. A* **103**(48), 9573–9578 (1999).
- [63] Frondelius, P., Hellman, A., Honkala, K., Hakkinen, H., and Gronbeck, H. *Phys. Rev. B* **78**(8) (2008).
- [64] Bond, G. C. and Thompson, D. T. *Gold Bull.* **33**(2), 41–51 (2000).
- [65] Bond, G. C., Louis, C., and Thompson, D. T. *Catalysis by Gold*. Imperial College Press, 1. edition, (2006).
- [66] Grunwaldt, J.-D., Kiener, C., Wögerbauer, C., and Baiker, A. *J. Catal.* **181**, 223–232 (1999).
- [67] Shaikhutdinov, S., Meyer, R., Naschitzki, M., Baumer, M., and Freund, H.-J. *Catal. Lett.* **86**(4), 211–219 (2003).
- [68] Lemire, C., Meyer, R., Shaikhutdinov, S., and Freund, H.-J. *Angew. Chem. Int. Ed.* **43**(1), 118–121 (2004).
- [69] Zanella, R., Giorgio, S., Shin, C., Henry, C., and Louis, C. *J. Catal.* **222**(2), 357–367 (2004).
- [70] Deng, X., Min, B., Guloy, A., and Friend, C. *J. of Am. Chem. Soc.* **127**(25), 9267–9270 (2005).
- [71] Hutchings, G. *J. Catal.* **96**(1), 292–295 (1985).
- [72] Prati, L. and Rossi, M. *J. Catal.* **176**(2), 552–560 (1998).
- [73] Christensen, C., Jorgensen, B., Rass-Hansen, J., Egeblad, K., Madsen, R., Klitgaard, S., Hansen, S., Hansen, M., Andersen, H., and Riisager, A. *Angew. Chem. Int. Ed.* **45**(28), 4648–4651 (2006).
- [74] Abad, A., Concepcion, P., Corma, A., and Garcia, H. *Angew. Chem. Int. Ed.* **44**(26), 4066–4069 (2005).
- [75] Landon, P., Collier, P., Papworth, A., Kiely, C., and Hutchings, G. *Chem. Commun.* (18), 2058–2059 (2002).
- [76] Carlsson, A., Puig-Molina, A., and Janssens, T. V. W. *J. Phys. Chem. B* **110**(11), 5286–5293 (2006).
- [77] Haruta, M. *Stud. Surf. Sci. Catal.* **110**, 123 (1997).

- [78] Schimpf, S., Lucas, M., Mohr, C., Rodemerck, U., Bruckner, A., Radnik, J., Hofmeister, H., and Claus, P. *Catal. Today* **72**(1-2), 63–78 (2002). International Conference on Catalytic Gold 2001, CAPE TOWN, SOUTH AFRICA, 2001.
- [79] Okumura, M., Nakamura, S., Tsubota, S., Nakamura, T., Azuma, M., and Haruta, M. *Catal. Lett.* **51**(1–2), 53–58 (1998).
- [80] Schubert, M., Hackenberg, S., van Veen, A., Muhler, M., Plzak, V., and Behm, R. *J. Catal.* **197**(1), 113–122 (2001).
- [81] Yuan, Y., Asakura, K., Wan, H., Tsai, K., and Iwasawa, Y. *Catal. Lett.* **42**(1-2), 15–20 (1996).
- [82] Ando, M., Kobayashi, T., and Haruta, M. *Catal. Today* **36**(1), 135–141 (1997).
- [83] Lee, S.-J. and Gavriilidis, A. *J. Catal.* **206**(2), 305–313 (2002).
- [84] Calla, J., Bore, M., Datye, A., and Davis, R. *J. Catal.* **238**(2), 458–467 (2006).
- [85] Overbury, S. H., Schwartz, V., Mullim, D. R., Yan, W., and Dai, S. *J. Catal.* **241**(1), 56–65 (2006).
- [86] Abild-Pedersen, F. and Andersson, M. P. *Surf. Sci.* **601**(7), 1747–1753 (2007).
- [87] Nørskov, J. K., Rossmeisl, J., Logadottir, A., Lindqvist, L., Kitchin, J. R., Bligaard, T., and Jonsson, H. *J. Phys. Chem. B* **108**(46), 17886–17892 (2004).
- [88] Kurth, S., Perdew, J. P., and Blaha, P. *Int. J. Quant. Chem.* **75**, 889–909 (1999).
- [89] Atkins, P. and de Paula, J. *Physical Chemistry*. Oxford University Press, Oxford, 8 edition,(2006).
- [90] Wintterlin, J., Volkening, S., Janssens, T., Zambelli, T., and Ertl, G. *Science* **278**(5345), 1931–1934 (1997).
- [91] Molina, L. and Hammer, B. *Phys. Rev. B* **69**(15), 155424 (2004).
- [92] Nieuwenhuys, B. E. *Surf. Rev. Lett.* **3**, 1869–1888 (1996).
- [93] Grabow, L., Xu, Y., and Mavrikakis, M. *Phys. Chem. Chem. Phys.* **8**(29), 3369–3374 (2006).
- [94] Walther, G., Mowbray, D. J., Jiang, T., Jones, G., Jensen, S., Quaade, U., and Horch, S. *J. Catal.* **280**, 86–92 (2008).

## **Paper I**

### **Trends in catalytic NO decomposition over transition metal surfaces**

**Hanne Falsig, Thomas Bligaard, Jeppe Rass-Hansen, Arkady L. Kustov, Claus H. Christensen and Jens K. Nørskov**  
*Topics in Catalysis* 45 117 (2007)

# Trends in catalytic NO decomposition over transition metal surfaces

Hanne Falsig<sup>a</sup>, Thomas Bligaard<sup>b</sup>, Jeppe Rass-Hansen<sup>a</sup>, Arkady L. Kustov<sup>a</sup>, Claus H. Christensen<sup>a</sup>,  
and Jens K. Nørskov<sup>b,\*</sup>

<sup>a</sup>Department of Chemistry, Center for Sustainable and Green Chemistry, NanoDTU, Technical University of Denmark, Lyngby, 2800 Denmark

<sup>b</sup>Department of Physics, Center for Atomic-Scale Materials Design, NanoDTU, Technical University of Denmark, Lyngby, 2800 Denmark

The formation of NO<sub>x</sub> from combustion of fossil and renewable fuels continues to be a dominant environmental issue. We take one step towards rationalizing trends in catalytic activity of transition metal catalysts for NO decomposition by combining microkinetic modelling with density functional theory calculations. We show specifically why the key problem in using transition metal surfaces to catalyze direct NO decomposition is their significant relative overbinding of atomic oxygen compared to atomic nitrogen.

**KEY WORDS:** NO; NO<sub>x</sub>; decomposition; trends; microkinetic; volcano.

## 1. Introduction

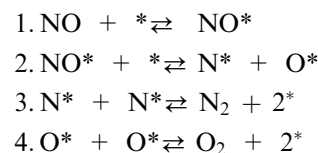
Nitrogen oxides (NO<sub>x</sub>) are formed from combustion of fossil and renewable fuels, and nitrogen monoxide (NO) accounts for more than 95% of these nitrogen emissions. NO<sub>x</sub> contribute to a wide range of environmental problems; the most significant being the formation of acid rain and photochemical smog. From a thermodynamic point of view, NO is unstable in the sense that it should spontaneously decompose into N<sub>2</sub> and O<sub>2</sub>. However, a high activation barrier of 3.8 eV inhibits this gas phase decomposition process [1]. A catalyst is therefore required in order to facilitate the reaction [2,3]. In this study, we describe the catalytic activity of a series of pure transition metal surfaces for the direct decomposition of NO by combining first principle calculations with microkinetic modelling. The theoretical modelling leads to a volcano curve for the activity, where the rate for the more noble surfaces is limited by how fast the catalyst can dissociate NO and for the more reactive surfaces by how fast desorption of O<sub>2</sub> occurs. We validate the modelled results by carrying out independent NO decomposition measurements. Our study provides insight into why transition metals in general perform poorly as direct NO decomposition catalysts. It is also shown which surface properties need modification in order to establish a catalyst with a useful level of activity.

## 2. Method

### 2.1. Microkinetic modelling

We aim to describe the trend in the catalytic activity of various transition metals in decomposing NO using a microkinetic model. Bligaard *et al.* [4] has described the

Sabatier analysis, which is closely related to the principle of Sabatier [5]. The Sabatier principle states that the catalytic activity for a given reaction follows a volcano curve through the Periodic Table, because an intermediate binding of reaction intermediates to the surface will give an optimal catalyst. The method is a simple microkinetic framework for analysing trends in the catalytic activity for processes where several (possibly competing) reaction steps take place. Decomposition of NO is here assumed to proceed in four elementary reaction steps,



Overall the decomposition is the sum of the elementary reactions



In addition we assume that reaction step 1 has a barrier, which for all the considered transition metals is dominated by the dissociation and association barriers of the strongly bound diatomics NO, N<sub>2</sub>, and O<sub>2</sub>. Under these assumptions, the entire thermochemistry of the NO decomposition reaction can be deduced from the available database [4]. Furthermore, since the dominant reaction steps 2–4 all are dissociation or association reactions of diatomic molecules, their transition state potential energies are described by the universal Brønsted–Evans–Polanyi relation described in Ref. [6]. Due to the significantly higher reactivity of steps compared to flat surfaces [7], we will in the present study assume that the key association and dissociation reac-

\* To whom correspondence should be addressed.  
E-mail: kustov@kemi.dtu.dk

tions occur at step sites. At these sites, the relation between the transition state potential energy and the dissociative chemisorption energy on a transition metal is  $E_{\text{TS}} = \alpha E_{\text{diss}} + \beta$ , where  $\alpha = 0.87$  and  $\beta = 1.34$  eV [6].

To calculate the prefactors in the forward rate constants of the four reaction steps, which is required to establish the Sabatier analysis, there is a need to specify the entropy of each state. Only entropy for molecules in the gas-phase is taken into account, whereas for adsorbed species and transition states we assume that all entropy has been lost upon adsorption. This is justified by the fact that the dominant entropy terms stem from the gas phase translational degrees of freedom, especially since the adsorbates considered here only have one or two atoms (and therefore few vibrational degrees of freedom).

For many heterogeneous catalytic processes carried out in a high coverage regime it turns out that the upper bound on the reaction rate provided by Sabatier analysis is too optimistic to yield quantitative agreement. This is caused by the Sabatier analysis being based on “optimal coverages” for each forward reaction [4]. Often the coverage of a species entering the microkinetic expression of a forward rate is much smaller than “optimal”. This can be due to either weak adsorption of the given species, or due to other species adsorbing so strongly that the coverage of the key species is suppressed. For reactions where all atoms of a given kind is only present in one form in the reactant and one form in the product, a more realistic strict upper bound to the steady-state solution of the microkinetic model can be found. This can be done simply by observing that the steady-state approximation forces the chemical potential of all reaction intermediates to be inside the interval defined by the reactant and product chemical potentials. This implies strict upper and lower bounds on the coverage of all adsorbed intermediates. The slight modification of the Sabatier analysis including these tighter bounds on the coverages of intermediates, we refer to as the Sabatier–Gibbs analysis [8].

Unless stated otherwise, the modelling has been made at  $T = 600$  °C, with a NO conversion of 5% and with an initial pressure of NO of 0.01 bar. The equilibrium constant for NO dissociation has been set to the value determined from the DFT energetics and standard tables for the reaction entropy.

### 3. Experimental

The catalysts were prepared by incipient wetness impregnation of metal solutions on a  $\text{MgAl}_2\text{O}_4$  support, with a surface area of  $70 \text{ m}^2/\text{g}$  and using metal concentrations of  $92 \text{ } \mu\text{mol}/\text{g}$ . Of each catalyst, 300 mg, was

placed in a quartz tube reactor. A flow of  $25 \text{ mL}/\text{min}$  of 1 vol.% NO in He was then admitted to the reactor at ambient pressure. The activity was measured at  $600\text{--}650$  °C. At each temperature, the measurement was performed for two hours to achieve stable conversions. The concentrations of NO,  $\text{N}_2$  and  $\text{O}_2$  were monitored using gas chromatography with a Thermal Conductivity Detector and a molecular sieve packed column. In all experiments, no traces of  $\text{N}_2\text{O}$  or other products were detected.

### 4. Results and discussion

In Figure 1, the dissociative chemisorption energies for NO,  $\text{O}_2$ , and  $\text{N}_2$  on the transition metals are presented. The dissociative chemisorption energies for  $\text{O}_2$  and  $\text{N}_2$  are plotted against the dissociation energy for bound NO. In the upper right corner, the energies are positive and therefore dissociation of NO is energetically uphill, and desorption of nitrogen and oxygen from the surface is favoured. The opposite situation appears in the lower left corner; here desorption of nitrogen and oxygen is energetically uphill, and dissociation of NO is favoured. On all the considered metal surfaces, oxygen binds stronger than nitrogen. Linear best fits of the energies show that the dissociation energy for bound NO is described very well with the dissociative chemisorption energy for  $\text{O}_2$  and less well with the corresponding energy for  $\text{N}_2$  dissociation.

Since the reaction energies of the elementary steps are highly correlated, we can in principle choose just one reaction energy as the descriptor for the catalyst activity. In Figure 2, the modelled Sabatier rates for each elementary reaction, together with the Sabatier and the Sabatier–Gibbs volcano curves are presented as a function of the dissociation energy of adsorbed NO.

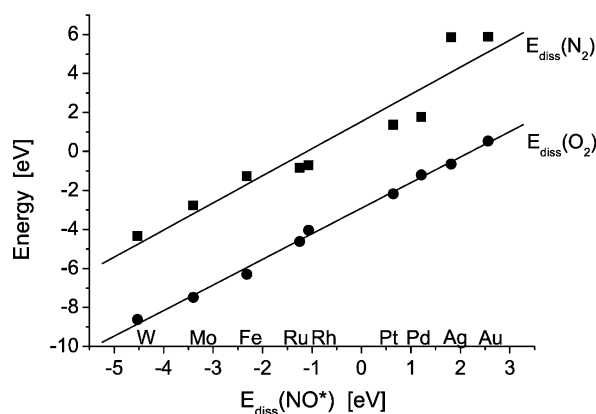


Figure 1. The figure shows the dissociative chemisorption energies for  $\text{N}_2$  and  $\text{O}_2$  versus the dissociation energy of adsorbed NO. Correlation equations are obtained from linear best fits,  $E_{\text{diss}}(\text{O}_2) = 1.31 E_{\text{diss}}(\text{NO}^*) - 2.91$  eV,  $R^2 = 0.99$   $E_{\text{diss}}(\text{N}_2) = 1.39 E_{\text{diss}}(\text{NO}^*) + 1.54$  eV,  $R^2 = 0.91$ .

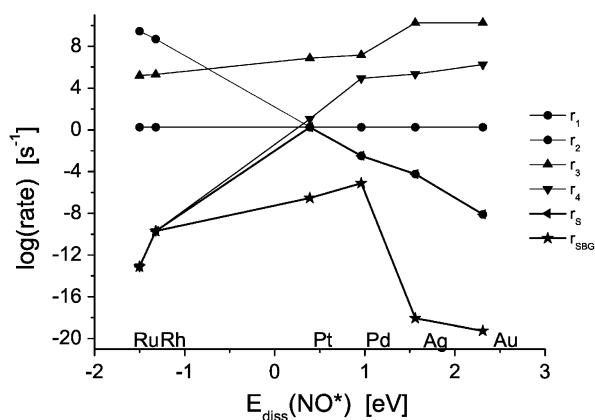


Figure 2. Sabatier rates for each elementary reaction, the Sabatier and the Sabatier-Gibbs volcano curves versus the dissociation energy of adsorbed NO. Where  $r_1$  is the rate for adsorption of NO,  $r_2$  is the rate for dissociation of NO,  $r_3$  is the rate for associative desorption of  $N_2$  and  $r_4$  is the rate for associative desorption of  $O_2$ .

The Sabatier volcano is determined by the rate of the NO dissociation on the right leg and by the desorption rate of oxygen on the left leg of the volcano in agreement with the Sabatier principle [5]. This is also the picture one would expect from the discussion of the correlated reaction energies. The activity ranking can be compiled: Pt > Pd > Ag > Au > Rh > Ru. Applying the constraints of the Sabatier-Gibbs model reduce the catalytic rate with orders of magnitude from the top of volcano and to the right. This results in a shift in the catalytic activity ranking: Pd > Pt > Rh > Ru > Ag > Au. In order to validate the Sabatier-Gibbs analysis, we compare activities with experimentally obtained activities in Figure 3. The Sabatier-Gibbs rates are calculated using the experimental conditions for the initial partial pressure, and 5% conversion of

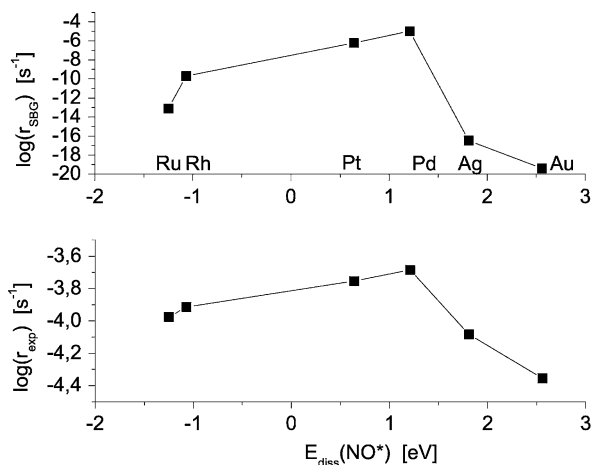


Figure 3. The Sabatier-Gibbs microkinetic model compared to the experimental activities versus the dissociation energy of adsorbed NO.

NO corresponding to average experimental conversion. Gervasini *et al.* [9] studied the catalytic activity of Pt, Pd, Rh and Ru experimentally. They found platinum to be the most active catalyst and the order of activity Pt > Rh > Ru > Pd using different experimental conditions from this study. The Sabatier-Gibbs model describes the trend in catalytic activity through the transition metals quite well. While the model is designed to investigate trends and cannot be viewed as quantitative, it is noteworthy that the most active transition metal, palladium is within a factor of ten from the experimental activity. However, the model is not able to quantitatively predict the decomposition rate on the two sides of the volcano curve. For the noble metals, silver and gold, on the right side of the volcano, the rate is underestimated by several orders of magnitude. However, the experimental activities are close to, what is observed for a blank sample. For the more reactive metals on the left side of the volcano, oxygen binds very strongly and desorption of oxygen is rate limiting. Here the surface is completely covered with oxygen. The adsorption energies used in this work are obtained from low coverage calculations. Therefore the lateral interactions taking place at high coverage are underestimated. We have performed a test of the difference in the differential adsorption energy, when adsorbing two oxygen atoms next to each other at the step edge bridge site on a Rh(211) surface. It turns out that the differential adsorption energy for the first oxygen atom is  $-2.03$  eV and for the second oxygen atom it is reduced to  $-1.06$  eV. This destabilizing interaction between oxygen atoms at high coverage leads to less oxygen poisoning of the reactive catalyst and can perhaps explain our underestimation of the catalytic activity for ruthenium and rhodium.

## 5. Determining the optimal catalyst

An optimal catalyst for direct NO decomposition would be a surface that facilitates fast dissociation of NO and at the same time desorbs oxygen and nitrogen easily. The linear relation between the activation barrier for NO dissociation and the binding energy of the reaction intermediates implies that one is not likely to find really good NO decomposition catalysts among the transition metals. In Figure 4, the catalytic activity in form of the Sabatier-Gibbs rate for varying dissociative chemisorption energies for  $N_2$  and  $O_2$  is presented. The figure shows a 2-dimensional volcano with a maximum. The DFT-calculated energies for the transition metals are also shown in the figure. The dissociation energy of NO, necessary to construct the volcano, has been determined from the good linear correlation to the dissociation energy of  $O_2$ . It is clear that the transition metals are far away from the optimal range. The adsorption energy of oxygen is simply too strong

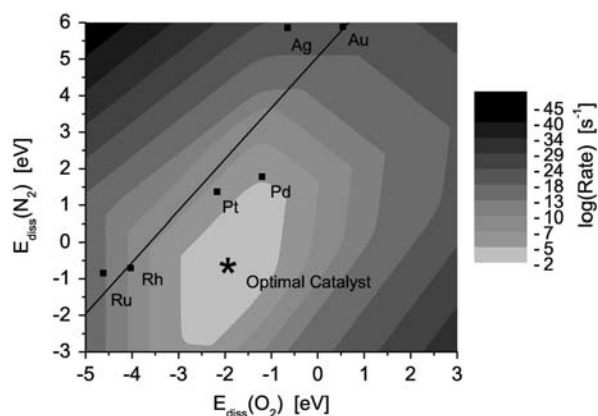


Figure 4. The Sabatier–Gibbs activity is illustrated in greyscale contours as a function of the dissociative chemisorption energies of  $O_2$  and  $N_2$ . The dissociation energy for NO is determined from its correlation with  $E_{\text{diss}}(O_2)$ . The positions of the transition metals from DFT calculations are indicated in the figure.

compared to the adsorption energy of nitrogen and the linear relation between these (see Figure 1) prevents the possibility of finding a transition metal in the vicinity of the volcano top.

## 6. Conclusion

We have established a simple first-principle qualitatively microkinetic analysis for direct NO decomposition over stepped transition metal surfaces. The Sabatier–Gibbs model shows (perhaps fortuitously) good qualitative agreement with experimental measurements. Our

analysis suggests that in order to find a direct NO decomposition catalyst with appreciable activity, one should search among classes of materials, which provide a stronger adsorption of nitrogen compared to oxygen.

## Acknowledgments

The Center for Sustainable and Green Chemistry is sponsored by the Danish National Research Foundation. The authors acknowledge support from the Danish Research Agency (grant 26-04-0047) and the Danish Center for Scientific Computing (grant HDW-1103-06).

## References

- [1] H. Glick, J.J. Klien and W. Squire, *J. Chem. Phys.* 27 (1957) 850.
- [2] F. Garin, *Appl. Catal. B: Env* 222 (2001) 183.
- [3] V.I. Pârvulescu, P. Grange and B. Delmon, *Cat. Today* 46 (1998) 316.
- [4] T. Bligaard, J.K. Nørskov, S. Dahl, J. Matthiesen, C.H. Christensen and J. Sehested, *J. Catal* 224 (2004) 206.
- [5] P. Sabatier, *Ber. Deutsch. Chem. Gesellschaft* 44 (1911) 1984.
- [6] J.K. Nørskov, T. Bligaard, A. Logadottir, S. Bahn, L.B. Hansen, M. Bollinger, H. Bengaard, B. Hammer, S. Sljivančanin, M. Mavrikakis, Y. Xu, S. Dahl and C.H. Jacobsen, *J. Catal* 209 (2002) 275.
- [7] S. Dahl, A. Logadottir, R.C. Egeberg, J.H. Larsen, I. Chorkendorff, E. Törnqvist and J.K. Nørskov, *Phys. Rev. Lett* 83 (1999) 1814.
- [8] T. Bligaard *et al.*, to be published.
- [9] A. Gervasini, P. Carniti and V. Ragaini, *Appl. Catal. B: Env* 22 (1999) 201.



## **Paper II**

### **Direct NO decomposition over stepped transition-metal surfaces**

**Hanne Falsig Thomas Bligaard, Claus H. Christensen and Jens K. Nørskov**

**Pure and Applied Chemistry 79 1895 (2007)**

## Direct NO decomposition over stepped transition-metal surfaces\*

Hanne Falsig<sup>1</sup>, Thomas Bligaard<sup>2</sup>, Claus H. Christensen<sup>1</sup>, and Jens K. Nørskov<sup>2,‡</sup>

<sup>1</sup>Center for Sustainable and Green Chemistry, Department of Chemistry, Building 206, NanoDTU, Technical University of Denmark, DK-2800 Lyngby, Denmark;

<sup>2</sup>Center for Atomic-Scale Materials Design, Department of Physics, Building 311, NanoDTU, Technical University of Denmark, DK-2800 Lyngby, Denmark

**Abstract:** We establish the full potential energy diagram for the direct NO decomposition reaction over stepped transition-metal surfaces by combining a database of adsorption energies on stepped metal surfaces with known Brønsted–Evans–Polanyi (BEP) relations for the activation barriers of dissociation of diatomic molecules over stepped transition- and noble-metal surfaces. The potential energy diagram directly points to why Pd and Pt are the best direct NO decomposition catalysts among the 3d, 4d, and 5d metals. We analyze the NO decomposition reaction in terms of a Sabatier–Gibbs-type analysis, and we demonstrate that this type of analysis yields results that to within a surprisingly small margin of error are directly proportional to the measured direct NO decomposition over Ru, Rh, Pt, Pd, Ag, and Au. We suggest that Pd, which is a better catalyst than Pt under the employed reaction conditions, is a better catalyst only because it binds O slightly weaker compared to N than the other metals in the study.

**Keywords:** NO; NO decomposition; Brønsted–Evans–Polanyi; activation barriers; dissociation; decomposition catalyst.

### INTRODUCTION

Heterogeneous catalysis is one of the major industries worldwide. Catalysis is used to facilitate the production of many chemicals and materials that we use every day. It provides a range of products from fuels and fertilizers to plastics and pharmaceuticals. Catalysts are also utilized for the cleaning of exhaust from cars, power plants, and industrial production.

The proliferation of heterogeneous catalysis during the 20<sup>th</sup> century has indeed led to a significant improvement in the living standard of a large fraction of the world's population. It is perhaps therefore natural that one of the hundreds of important heterogeneous catalytic reactions was selected as the most important invention of the 20<sup>th</sup> century, ahead of the discovery of penicillin, the construction of the first transistor and the design of the integrated semiconductor circuit [1].

The increasingly stringent emission requirements for diesel engines require NO<sub>x</sub> abatement technology, which is effective under lean-burn conditions. Various technologies such as NO<sub>x</sub> traps [2] and

---

\**Pure Appl. Chem.* **79**, 1831–2100. An issue of reviews and research papers based on lectures presented at the 1<sup>st</sup> International IUPAC Conference on Green–Sustainable Chemistry, held in Dresden, Germany, 10–15 September 2006.

‡Corresponding author

selective catalytic reduction (SCR) exist [3], but it would be preferable if a simpler process could be developed based on direct NO decomposition. In the direct NO decomposition reaction, the exhaust containing NO is flowed over a heterogeneously catalytic surface, where the NO bond is split, and N atoms recombine to  $N_2$  while the O atoms recombine to  $O_2$ . The direct NO decomposition reaction is thermodynamically favored at low temperatures, but it has proven difficult to find a catalyst that is both active and oxidation-resistant [4]. Here, we study the direct decomposition of NO over stepped transition-metal surfaces, since such step sites are known from theoretical calculations to be significantly more active for NO decomposition than the corresponding close-packed surfaces [5–9]. This enhanced reactivity of steps also explains why smaller transition-metal particles show enhanced activity for NO decomposition [10].

The way we normally perform such studies is by establishing a total energy diagram for each of the catalytic surfaces in question, as schematically shown in Fig. 1. The figure shows the energy levels for a catalytic reaction. The energies of transition-state structures and reaction intermediates on the surface are determined by employing density functional theory (DFT) in a plane wave/pseudopotential implementation. This methodology gives a very reasonable trade-off between accuracy and computational cost. The total energy diagrams are then analyzed in terms of harmonic transition-state theory to yield rates for individual elementary reactions, and these rates are then analyzed using microkinetic modeling to establish the overall catalytic rate per active site, the so-called turnover frequency. Often, it occurs that there is a correlation between the energies of transition-state structures corresponding to the activation of reactants and the key reaction intermediates ( $E_a$  and  $\Delta E$  in Fig. 1).

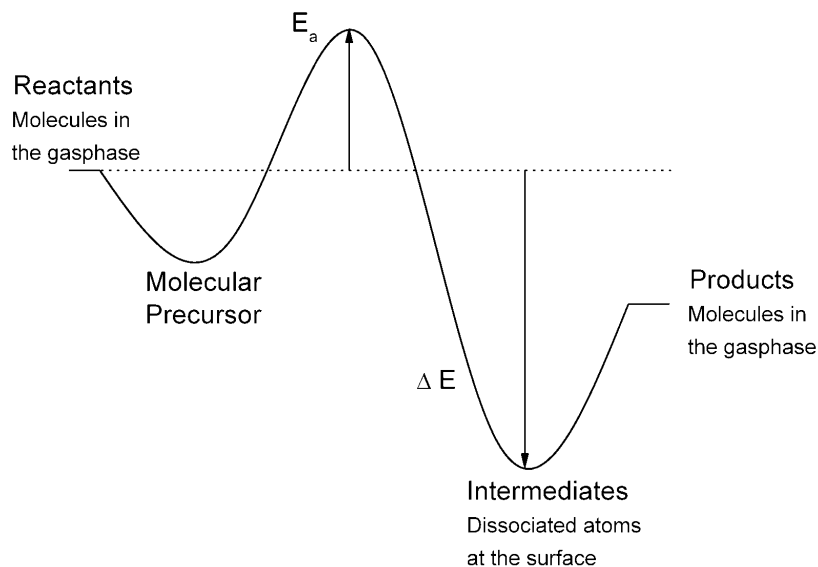


**Fig. 1** Schematic energy diagram for a heterogeneously catalytic reaction.

When such a correlation appears, the trend in catalytic activity for metals of different reactivity in the periodic table can be understood directly based on a single descriptor, which we often choose to be the dissociative chemisorption energy of the key reactant. An activity trend such as the schematic plot shown in Fig. 2 will often appear (a volcano relation). For more reactive metals ( $\Delta E$  further to the left), the removal of the dissociated reactants from the surface into the product gas phase will usually limit the catalytic rate. For the less reactive metals (to the right in Fig. 2), this desorption process is fast, and the dissociation barrier is high, so the catalytic rate is limited by the activation of the key reactants.

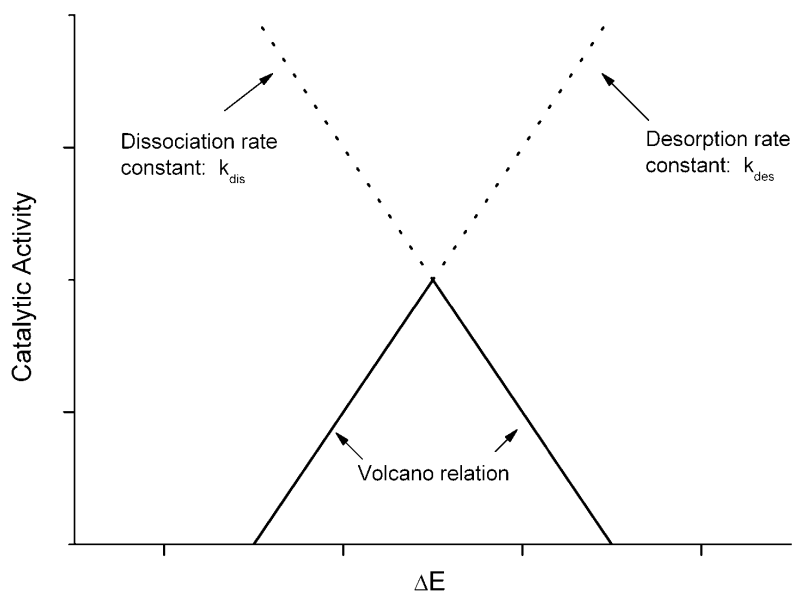


**Fig. 2** Catalytic activity vs. the reaction energy of the dissociation reaction. More negative reaction energy (left) signifies that the adsorption reaction is more exothermic.

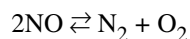
The optimal catalyst will be one having intermediate reaction energies, and the catalyst will be located at the top of the volcano curve. Sabatier realized this as early as 1911 [11].

### DIRECT DECOMPOSITION OF NO OVER STEPPED TRANSITION-METAL SURFACES

The direct decomposition of NO is assumed to take place through four elementary reactions over a catalyst:

1.  $\text{NO} + * \rightleftharpoons \text{NO}^*$
2.  $\text{NO}^* + * \rightleftharpoons \text{N}^* + \text{O}^*$
3.  $\text{N}^* + \text{N}^* \rightleftharpoons \text{N}_2 + 2*$
4.  $\text{O}^* + \text{O}^* \rightleftharpoons \text{O}_2 + 2*$

A species denoted with an asterisk is adsorbed on an active site of the catalyst. An asterisk without a molecular or atomic species denotes a vacant active site on the surface. The full direct decomposition reaction is given by summing over the elementary reactions, and is given by



The decomposition reaction has two main parts: The first is the adsorption and dissociation of NO (elementary reactions 1 and 2), and the second part is recombination and the removal of  $\text{N}_2$  and  $\text{O}_2$  from the metal surface (elementary reactions 3 and 4).

In Fig. 3, images from the dissociation of NO on a stepped Rh surface are shown. The images show the initial, the transition, and the final state of the dissociation.

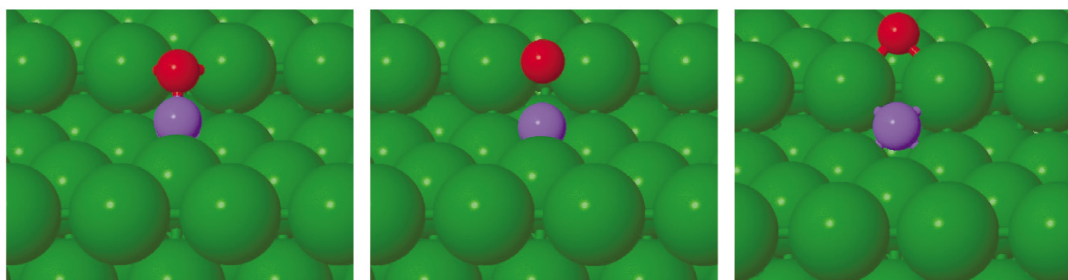


**Fig. 3** Illustration of the dissociation of NO over a stepped (211) Rh surface as determined from DFT calculations. Left: initial state. Middle: transition state. Right: final state.

It has long been assumed that a linear relation between the activation energy and the reaction energy exists. Such relations are called Brønsted–Evans–Polanyi (BEP) relations [12–14]. For the key reactants and products in the direct decomposition of NO over transition-metal surfaces, such a relation indeed appears. In Fig. 4, the activation barriers for dissociation of NO, O<sub>2</sub>, and N<sub>2</sub> over a range of transition metals are shown as a function of their respective dissociative chemisorption energies [6].

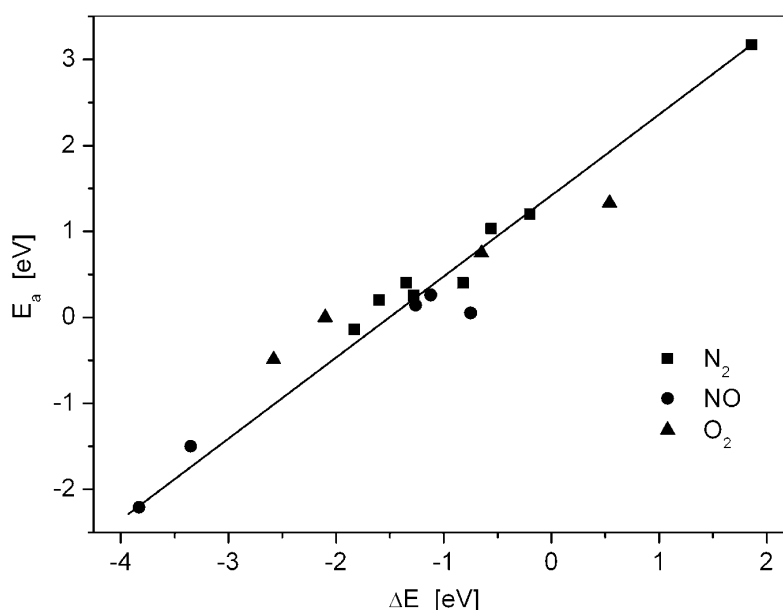


**Fig. 4** “Universal” BEP relation for activation of diatomic molecules. (NO, N<sub>2</sub>, and O<sub>2</sub>). Adapted from ref. [6].

It appears that the correlation between transition states and dissociation energies is linear, and that the correlations for each of the diatomic molecules follow the same exact relationship. The relation also shows that the dissociation of NO will take place fast, when O and N are adsorbed strongly to the metal surface.

A good catalyst is a catalyst that lowers the activation barriers for each of the elementary reactions in the overall decomposition reaction. Therefore, according to Fig. 4, a good catalyst for the first part of the decomposition is a transition metal to which N and O adsorb strongly, since this will lower the activation barrier for dissociation of NO. The second part of the overall reaction is removal of N and O from the surface. This happens via associative desorption, elementary reactions 3 and 4. N<sub>2</sub> and O<sub>2</sub>

associate at the surface and desorb immediately hereafter. This reaction is just the opposite of dissociative chemisorption and accordingly is favored by a weak adsorption of N and O. This rationale is what leads to the volcano curve in heterogeneous catalysis. Where the first part of the direct decomposition is favored by a strong adsorption of the reaction intermediates, the second part is favored by a weak adsorption. This suggests that intermediate surface reactivity will provide an optimal compromise and result in a fast overall rate.

When the correlation shown in Fig. 4 is combined with a set of adsorption energies on stepped transition- and noble-metal surfaces [15], a set of potential energy diagrams for the whole NO decomposition pathway over some of the most important stepped surfaces can be constructed. These energy diagrams are shown in Fig. 5. Of the pure transition- and noble-metal surfaces, it can be seen by inspection that the best catalysts must be Pt and Pd, since these do not over-bind intermediates to the same extent as Rh and Ru, while at the same time they do not present the same problems of unstable reaction intermediates on the surface as Ag and Au.

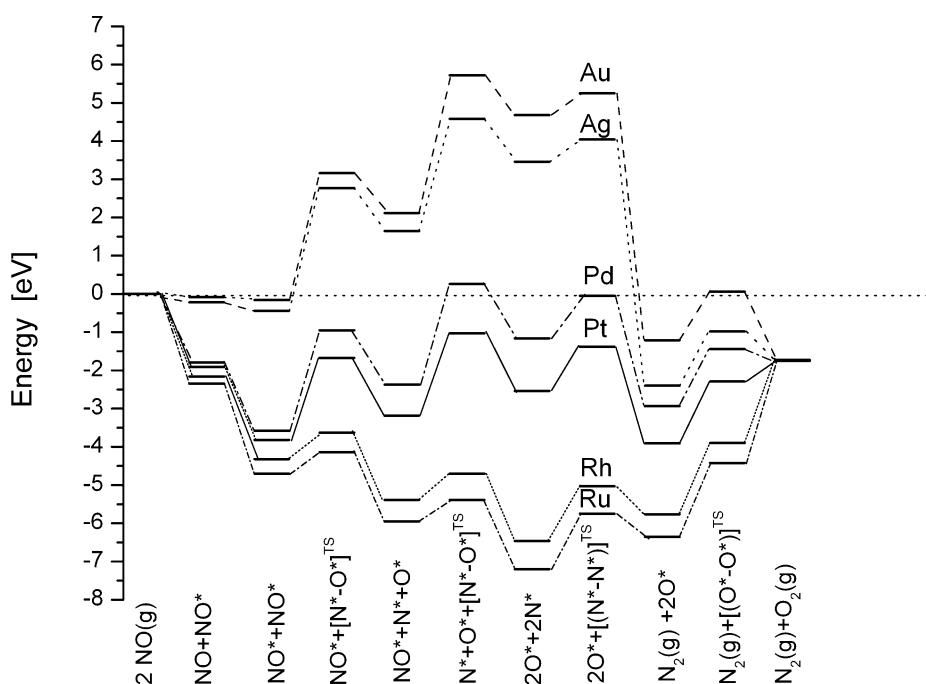
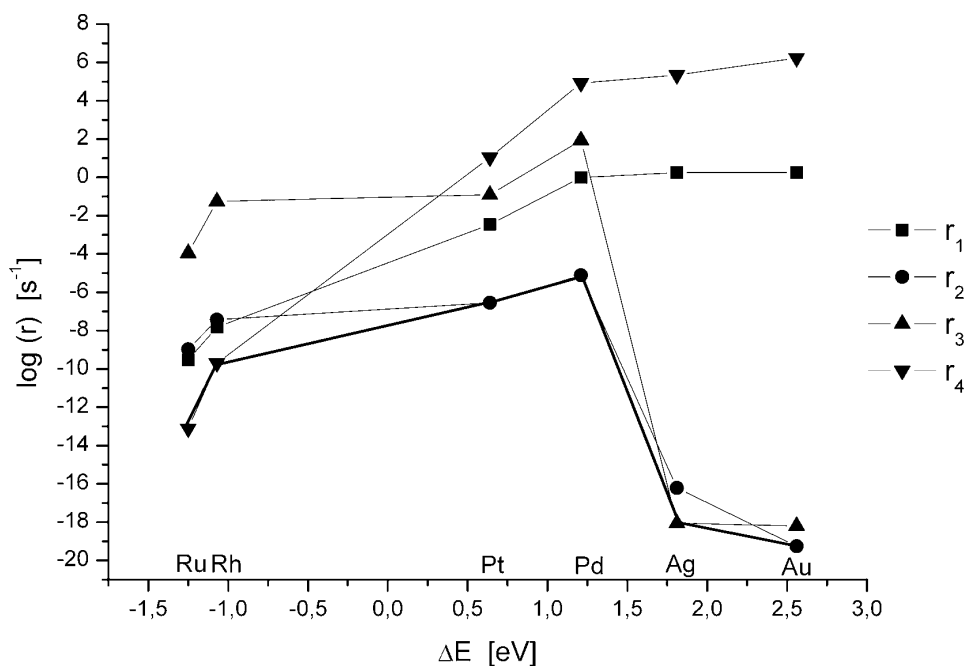


Fig. 5 Potential energy diagrams for the direct NO decomposition reaction over transition-metal surfaces.

### WHICH CATALYST IS OPTIMAL? A DFT STUDY

In the previous section, we described the characteristics a catalyst must possess in order to decompose NO directly to  $N_2$  and  $O_2$ . We will now demonstrate how we are able to determine, by the use of DFT and microkinetic modeling, the rate on a more quantitative yet still analytical form [16]. The reaction energy for each elementary reaction was obtained using a plane-wave pseudopotential implementation of DFT. The publicly available program Dacapo [17] was employed. From the BEP relation shown in Fig. 4, we can obtain the activation barrier for each elementary reaction. For each elementary reaction, the rate has been obtained using the Sabatier–Gibbs model [18]. The temperature was 600 K, and the initial pressure of NO was 0.01 bar [16]. This model is particularly useful when looking at catalytic trends in systems which are inhibited by high coverages of some key intermediates. In the Sabatier–Gibbs analysis, we start from the assumption that the catalyst is running in the steady state,

meaning time-independent average mean-field coverages. It can be proven that the chemical potential of any species in the reaction is constrained to be in the interval between the chemical potentials defined by the equilibrium between that species and the reactants and the products, respectively. The boundaries on the chemical potential of each intermediate then yield boundaries on the coverage of all the different intermediates. The boundaries on the coverages yield boundaries on the catalytic rate, and the maximal possible rate obtainable under these constraints we refer to as the Sabatier–Gibbs rate. The Sabatier–Gibbs rate for the decomposition of NO to N<sub>2</sub> and O<sub>2</sub>, is then the minimum of the individual rates. In Fig. 6, the rates for the individual elementary reactions are shown together with the Sabatier–Gibbs rate.



**Fig. 6** Sabatier–Gibbs rates for each elementary reaction and the Sabatier–Gibbs volcano curve vs. the dissociation energy of adsorbed NO. Here,  $r_1$  is the rate for adsorption of NO,  $r_2$  is the rate for dissociation of NO,  $r_3$  is the rate for associative desorption of N<sub>2</sub>, and  $r_4$  is the rate for associative desorption of O<sub>2</sub>.

The first elementary reaction is adsorption of NO to the metal surface. The rate of this process is denoted  $r_1$ . The model predicts that the adsorption is faster on the more noble metals such as, for example, Ag and Au, than on more reactive metals, such as Rh and Ru. The surfaces of the more reactive metals (Rh, Ru) will be entirely covered by oxygen due to the significant negative adsorption energy. Therefore, an extremely limited amount of free sites will be available for adsorption of NO. On the noble metals, the adsorption of O<sub>2</sub> is less facile, and many free sites are available for adsorption of NO on these surfaces. The next step is dissociation of NO. The dissociation is most activated on the more reactive metals, due to the stronger adsorption of the intermediates. However, as shown in Fig. 3, in order for the dissociation to take place free sites must be available for the atomic N and O. The dissociation rate is fastest on Pd and slowest on Au, which is in good agreement with the fact that Pd is more reactive than Au. The Rh surface is, however, so reactive that it will be covered with oxygen. Therefore, the amount of free sites is very limited, and this is the reason why the dissociation of NO is slower on Rh than, e.g., Pd. The two final steps is associative desorption of N and O from the metal to the gas phase. Intuitively, we know that a strong adsorption will limit the desorption rate. This is also what is

observed. The associative desorption of  $O_2$  is slowest on Rh and fastest on Au. This is almost the same picture as for  $N_2$ , however, N hardly adsorbs to Au and Ag, and therefore N will not be present. On Fig. 6, a volcano curve is highlighted. The volcano curve is constructed of for each metal. It is seen that Pd is the most active metal for NO decomposition.

## EXPERIMENTAL VERIFICATION

In order to show that the model correctly describes the catalytic activity of the transition metals in NO decomposition, a comparison between theoretically predicted rates and experimentally obtained results is shown in Fig. 7.

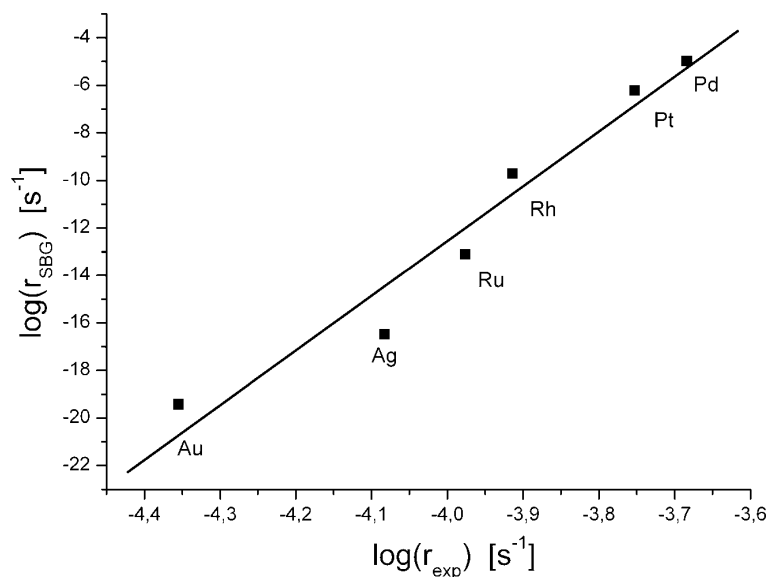


**Fig. 7** Modeled decomposition rate vs. experimental results for a range of different transition-metal surfaces (obtained from ref. [16]).

The Sabatier–Gibbs rate is compared to experimental measurements of the direct NO decomposition reaction rates over various surfaces, and the qualitative agreement is striking, even if the absolute magnitude of the theoretically determined rates is less well determined.

In Fig. 8, the theoretically calculated direct NO decomposition rates are shown as a function of the dissociative chemisorption energies of  $N_2$  and  $O_2$ . A two-dimensional overall volcano is formed. It is interestingly observed that the transition metals lay on a line that is situated several eVs above the optimal point of the two-dimensional volcano. This indicates that one could find a much better transition-metal catalyst for direct NO decomposition, if only a metal could be chosen, which binds N atoms much strongly compared to O atoms. However, since the dissociative chemisorption energy for these species is linearly related, no such transition-metal catalyst can be found. This suggests that one needs to look into entirely different classes of materials in order to find appropriate direct NO decomposition catalysts, and that a more appropriate class of materials should have the property that N and O binds with a more equal strength to the surface.



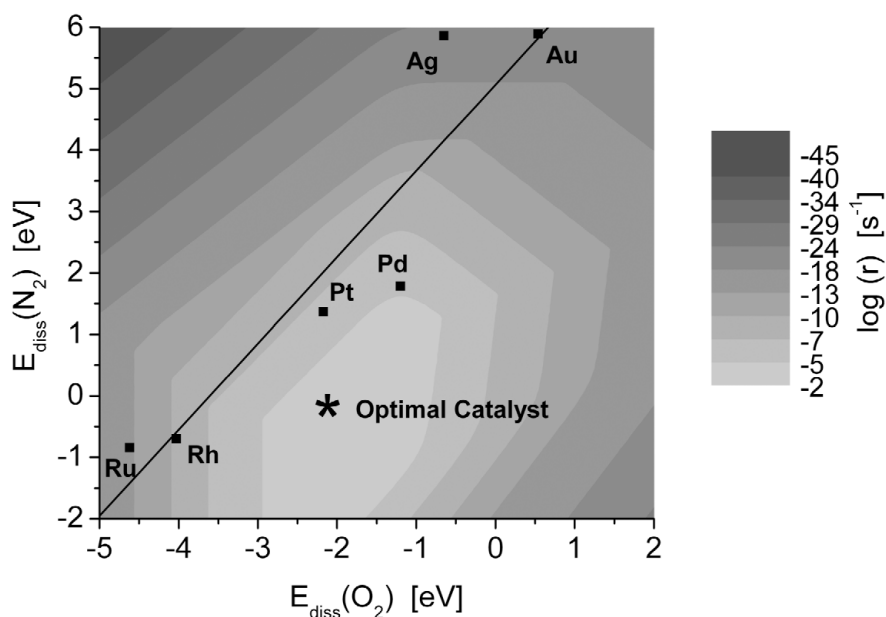


**Fig. 8** Theoretically predicted decomposition rate as a function of the dissociative chemisorption energies of  $\text{N}_2$  and  $\text{O}_2$ . The dissociative chemisorption energies for  $\text{N}_2$  and  $\text{O}_2$  over a range of stepped transition-metal surfaces are also shown. The line represents the linear relation between the dissociative chemisorption energies for the transition metals.

## CONCLUSION

The direct decomposition of NO on transition metals can be understood in detail from DFT studies. Linear correlations between reaction energies and activation barriers lead to clear trends, where Au and Ag have problems activating NO, while Rh and Ru rapidly becomes poisoned by strongly binding O atoms (especially on the most active step sites). Pd and Pt show the best catalytic activities among the pure metals treated in the present study, but the activity is still much too low in order for the pure metal surfaces to be useful direct NO decomposition catalysts for automotive purposes under lean-burn conditions. The model enables us to understand the volcano curve for decomposition of NO and thereby understand the trend in catalytic activity of the transition metals. Furthermore, the results are in good qualitative agreement with experimental results. The modeling clearly identifies one important underlying origin for the limited attainable catalytic activity of the stepped transition-metal surfaces with respect to direct NO decomposition, which is the too strong adsorption of O compared to N.

## ACKNOWLEDGMENTS

The Center for Sustainable and Green Chemistry is funded by the Danish National Research Foundation, and the Center for Atomic-scale Materials Design is funded by the Lundbeck Foundation. We wish to acknowledge support from the Danish Research Agency through the framework program number 26-04-0047 and the Danish Center for Scientific Computing through grant HDW-0107-07.

## REFERENCES

1. V. Smil. *Nature* **400**, 415 (1999).
2. H. Mahzoul, J. F. Brilhac, P. Gilot. *Appl. Catal., B* **20**, 47 (1999).
3. H. Burch, J. P. Breen, F. C. Meunier. *Appl. Catal., B* **39**, 283 (2002).
4. C. T. Goralski Jr., W. F. Schneider. *Appl. Catal., B* **37**, 263 (2002).
5. B. Hammer. *Phys. Rev. Lett.* **83**, 3681 (1999).
6. J. K. Nørskov, T. Bligaard, A. Logadottir, S. Bahn, L. B. Hansen, M. Bollinger, H. Benggaard, B. Hammer, S. Sljivancanin, M. Mavrikakis, Y. Xu, S. Dahl, C. J. H. Jacobsen. *J. Catal.* **209**, 275 (2002).
7. Q. Ge, M. Neurock. *J. Am. Chem. Soc.* **126**, 1551 (2004).
8. Z.-P. Liu, S. J. Jenkins, D. A. King. *J. Am. Chem. Soc.* **125**, 14660 (2003).
9. B. Hammer. *Top. Catal.* **37**, 3 (2006).
10. D. R. Rainer, S. M. Vesecky, M. Koranne, W. S. Oh, D. W. Goodman. *J. Catal.* **167**, 234 (1997).
11. P. Sabatier. *Ber. Dtsch. Chem. Ges.* **44**, 1911 (1984).
12. A. Logadottir, T. H. Rod, J. K. Nørskov, B. Hammer, S. Dahl, C. J. H. Jacobsen. *J. Catal.* **197**, 229 (2001).
13. N. Brønsted. *Chem. Rev.* **5**, 231 (1928).
14. M. G. Evans, M. Polanyi. *Trans. Faraday Soc.* **34**, 11 (1938).
15. T. Bligaard, J. K. Nørskov, S. Dahl, J. Matthiesen, C. H. Christensen, J. S. Sehested. *J. Catal.* **224**, 206 (2004).
16. H. Falsig, T. Bligaard, J. Rass-Hansen, A. L. Kustov, C. H. Christensen, J. K. Nørskov. *Top. Catal.* **45**, 117 (2007).
17. B. Hammer, L. B. Hansen, J. K. Nørskov. *Phys. Rev. B* **741**, 359 (1999).
18. T. Bligaard, H. Falsig, C. H. Christensen, J. K. Nørskov. "Sabatier-Gibbs Analysis of Microkinetic Models", in preparation.

## **Paper III**

### **Trends in CO Oxidation Rates for Metal Nanoparticles and Close-Packed, Stepped, and Kinked Surfaces**

**Tao Jiang, Duncan J. Mowbray, Sergey Dobrin, Hanne Falsig, Britt Hvolbæk, Thomas Bligaard, Jens K. Nørskov**

**J. Phys. Chem. C 113 10548 (2009)**

# Trends in CO Oxidation Rates for Metal Nanoparticles and Close-Packed, Stepped, and Kinked Surfaces

T. Jiang, D. J. Mowbray, S. Dobrin, H. Falsig, B. Hvolbæk, T. Bligaard, and J. K. Nørskov\*

Center for Atomic-Scale Materials Design, Department of Physics, Technical University of Denmark, DK-2800 Kgs. Lyngby, Denmark

Received: December 18, 2008; Revised Manuscript Received: April 15, 2009

Using density functional theory calculations, we study trends in the CO oxidation activity for different metals and surfaces. Specifically, we show how the activity of (111) close-packed surfaces, (211) stepped surfaces, (532) kinked surfaces, 55 atom cuboctahedral clusters, and 12 atom cluster models changes with the coordination number of atoms at the active sites. This effect is shown to be electronic in nature, as low coordinated metal atoms, which bind reactants most strongly, have the highest energy metal d states.

## Introduction

The CO oxidation reaction,  $\text{CO} + \frac{1}{2}\text{O}_2 \rightarrow \text{CO}_2$ , often serves as a prototypical reaction in heterogeneous catalysis. Its importance is exemplified by its use to remove toxic CO from the exhaust of motor vehicles, where Pt, Pd, and Rh are the catalysts of choice.<sup>1,2</sup> Yet the reaction is relatively simple, with only two reactants and one product. For these reasons it is very well studied, both experimentally<sup>3–13</sup> and theoretically.<sup>14–18</sup> The CO oxidation reaction has also served as a test reaction in the recent exploration of the catalytic activity of nanoparticle Au.<sup>8,9,18–31</sup> Interestingly, small Au nanoparticles ( $d \lesssim 5$  nm) were found to be catalytically active, whereas larger Au particles and close-packed extended surfaces are much less so. This has been variously attributed to quantum size effects,<sup>8</sup> support interactions,<sup>22,23,32</sup> charge transfer,<sup>24,25,33</sup> and the role of low-coordinated sites.<sup>14,17,26–30,34</sup>

Unlike most previous studies of the CO oxidation reaction, we will concentrate in the present paper on the broad trends in reactivity. We will use density functional theory (DFT) calculations to describe the variation of bond energies and activation energies with metal and surface structures. As we are interested in broader trends, we have chosen not to consider coverage dependence or surface oxidation at certain conditions.<sup>1</sup> Instead, we will compare metals under idealized conditions where the surface coverages are optimal. While these conditions may not be realizable in practice, the present work may be viewed as a comparison of the intrinsic catalytic activity of different metals (in their metallic states) and different surface structures.

We begin with a short description of the structure models and calculation method used. This is followed by an introduction to the microkinetic model and Sabatier analysis used to compare reaction rates for different metals. We will show that to a first approximation the rate is a volcano-shaped function of the adsorption energy of O and CO. In so doing, we extend and elaborate on the work started in ref 35. By calculating the volcano function for various stepped and kinked surfaces as well as for nanoparticles, we show that the peak location does not depend strongly on the surface geometry. However, the rate itself is strongly dependent on the geometry. This is because the adsorption energies, and hence the activation energies, are geometry dependent. In spite of its simplicity, this analysis yields

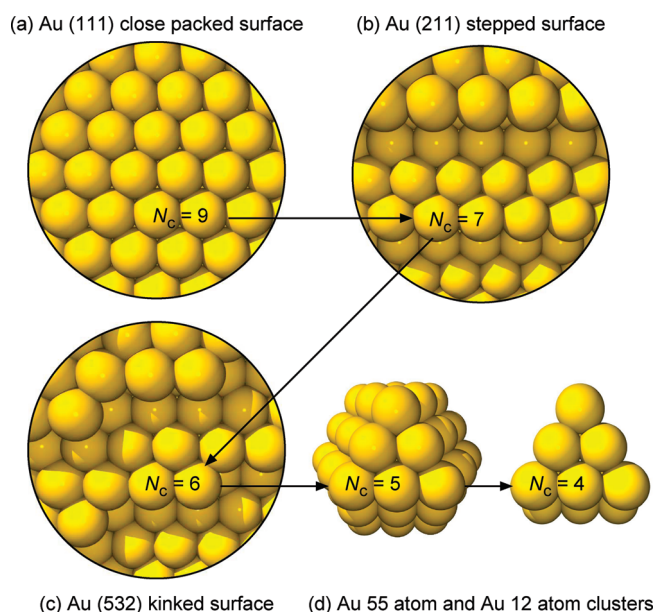


**Figure 1.** Structural schematics and lowest coordination number  $N_c$  for the (a) Au (111) close-packed surface, (b) Au (211) stepped surface, (c) Au (532) kinked surface, and (d) Au 55 atom cuboctahedral cluster and Au 12 atom cluster corner model.

results in qualitative agreement with available experimental data, including the special catalytic activity of Au nanoparticles. This model also provides a simple picture of geometrical effects in the CO oxidation reaction. Finally, we use these calculations to identify the electronic origin of the structure dependence of the chemical activity.

## Method

**Surface Structures.** Surface geometry is known to play an important role in the catalytic properties of metals. Here we compare the catalytic activity of the five different surface structures shown in Figure 1a–d. We begin by studying the activity of a close-packed surface (111), a stepped surface (211), and a surface with both steps and kinks (532). To better describe highly under-coordinated surface structures, we also study a 12 atom cluster chosen to model a sharp corner on a large nanoparticle with the metal atoms kept fixed at the bulk lattice

\* To whom correspondence should be addressed. E-mail: norskov@fysik.dtu.dk.

constant values (M12). Further, to describe the influence of decreasing size on adsorption energies we have used a “magic size” 55 atom cuboctahedral cluster model. Although not necessarily the most stable structure, cuboctahedral Au and Pt clusters have been found experimentally.<sup>36–38</sup> Also, unlike other cluster types, such as icosahedral, cuboctahedral clusters have a bulk fcc structure. This aids in the comparison of energies and occupation sites with those for bulk surface structures.

**Calculation Method.** Adsorption, transition state, and gas phase energies are calculated using the plane wave DFT code DACAPO.<sup>39</sup> Kohn–Sham one-electron valence states are expanded in a basis of plane waves with kinetic energies up to 30 Ry. Vanderbilt nonlocal ultrasoft pseudopotentials are used to describe the core electrons. The exchange–correlation (xc)-energy is described employing the RPBE generalized gradient correction self-consistently.<sup>39</sup>

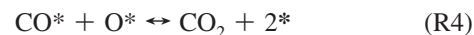
For all surfaces, a  $6 \times 6 \times 1$  Monkhorst-Pack  $\mathbf{k}$ -point sampling in the irreducible Brillouin zone was used. The occupation of the one electron states was calculated at a temperature of  $k_B T = 0.1$  eV, and all energies were extrapolated to  $T = 0$  K. Lattice constants have been determined by separate calculations on the bulk metals. The (111) surfaces were modeled by  $(2 \times 2)$  surface unit cells with slab thicknesses of four layers and the two topmost layers were allowed to fully relax. The (211) and (532) surfaces were modeled by  $(2 \times 1)$  and  $(1 \times 1)$  surface unit cells, respectively, with three close packed layer slabs, where only the topmost layer was allowed to relax. For all types of surfaces, the neighboring slabs are separated by more than 10 Å of vacuum. For both cluster structures,  $\Gamma$  point calculations were performed within unit cells with  $\geq 10$  Å of vacuum between structures, with a Fermi temperature of  $k_B T = 0.01$  eV. All of the atoms in the 12 atom clusters were kept fixed in order to mimic the geometrically constrained corner of a larger particle, with a lattice constant corresponding to the bulk value. On the other hand, the M55 cluster has a realistic nanoparticle structure,<sup>36–38</sup> so all atomic positions were relaxed.

We have included energy corrections for the adsorption of CO to avoid the overbinding of CO by DFT, which yields lower binding energies on bridge sites than atop sites, in contradiction to experiment.<sup>40</sup> Oxygen adsorption energies are calculated relative to the  $O_2$  energy from  $H_2O$  splitting using the experimental reaction energy and that for  $H_2$  and  $H_2O$  in the gas phase.<sup>41</sup> This avoids difficulties associated with a DFT treatment of the triplet state of gas phase  $O_2$ .<sup>42</sup>

**Microkinetic Modeling.** In order to link the calculated adsorption energies and activation energies with catalytic activity, we will employ a simplified microkinetic model, built on the analysis presented in ref 35. Such a model, based on adsorption energies and activation barriers for Au corner sites, has recently been shown to quantitatively reproduce the temperature dependent reactivity of Au nanoparticles.<sup>31</sup>

A simplified kinetic treatment, termed the “Sabatier analysis”, is used to estimate reaction rates.<sup>43</sup> In this analysis, the coverages of free sites and adsorbed species are assumed optimal for each reaction step. Although this may not be realizable under experimental conditions, the Sabatier rate yields an exact upper bound so long as the state of the surface does not change due to oxidation or reconstruction. The Sabatier analysis thus provides a measure of the intrinsic ability of a metal surface to catalyze a given reaction.

We begin by assuming a Langmuir–Hinshelwood type mechanism for CO oxidation, so that the reaction may be described using the following elementary steps:



Here we have assumed that reactions R1 and R2 have reached equilibrium, so that the net rates  $r_1 \approx r_2 \approx 0$ . Overall, the Sabatier rate for  $CO_2$  production is the sum of the rates for reactions R4 and R5. However reaction R4 is limited if no atomic oxygen is present from reactions R3 or R5. On the other hand, reaction R5 will be limited by a poisoning by atomic oxygen of the catalyst, and can therefore not be faster than reaction R4. Hence the overall reaction rate according to the Sabatier analysis is then

$$r_S = \max\{2\min\{r_5^+, r_4^+\}, \min\{2r_3^+, r_4^+\}\}$$

since the rates for reactions R3–R5 will be maximized if we consider only the forward rates  $r_i^+$ .

Following the procedure outlined in ref 35, the forward rates are given by

$$\begin{aligned} r_3^+ &= \theta_{O_2} \theta_* k_3^+ \\ r_4^+ &= \theta_O \theta_{CO} k_4^+ \approx \theta_{CO} k_4^+ \\ r_5^+ &= \theta_{O_2} \theta_{CO} k_5^+ \end{aligned}$$

where  $\theta_{CO}$ ,  $\theta_{O_2}$ ,  $\theta_O$ , and  $\theta_*$  are the coverages of CO,  $O_2$ , O, and unoccupied sites respectively. Note that we have assumed the rate for (R4) is independent of the O coverage, which was shown to give a good approximation to the fully self-consistently solved microkinetic model in ref 35. The rate constant  $k_i$  for the elementary reaction step,  $i$ , is given by

$$\begin{aligned} k_i &= \nu_i \exp\left[\frac{-\Delta G_{ai}}{k_B T}\right] \\ &= \nu_i \exp\left[\frac{-(E_{ai} + \Delta ZPE_{ai} - T\Delta S_{ai})}{k_B T}\right] \end{aligned}$$

where  $\nu_i$  is the prefactor,  $E_{ai}$  is the activation barrier for the reaction,  $\Delta ZPE_{ai}$  is the zero-point energy change,  $\Delta S_{ai}$  is the entropy change,  $k_B$  is the Boltzmann constant, and  $T$  is the temperature. We assume the prefactors are metal independent, so that  $\nu_i = k_B T/h$ , and that the change in zero-point energy is negligible compared to the activation barrier ( $\Delta ZPE_{ai} \ll E_{ai}$ ). Further, we assume the entropy of adsorbed species is much smaller than that in the gas phase ( $S_{ads} \ll S_{gas}$ ), so that  $\Delta S_{ai} \approx \mp S_{gas}$  for adsorption/desorption, where gas phase entropies are taken from ref 44. Activation barriers are found as the energy difference between the transition and initial state, ( $E_a = \max(E_{TS} - E_{IS}, 0)$ ).

Since reaction steps R1 and R2 are assumed to be in equilibrium, the coverages of CO and  $O_2$  satisfy  $\theta_{CO} = K_1 p_{CO} \theta_*$  and  $\theta_{O_2} = K_2 p_{O_2} \theta_*$ . The coverage of unoccupied adsorption sites

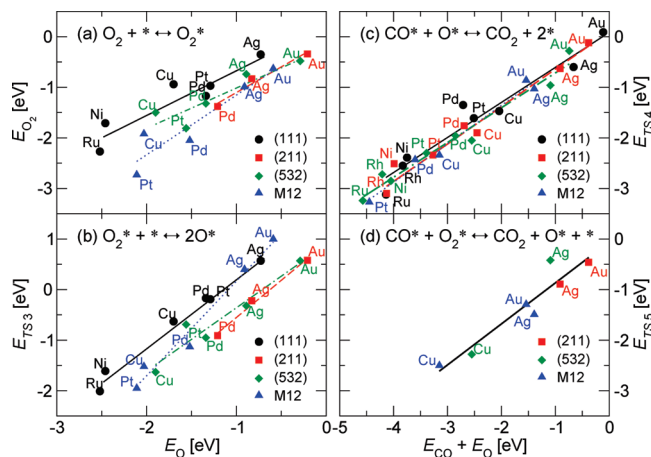


**Figure 2.** The scaling and BEP relations for (111) surfaces (●, — [black]), (211) surfaces (■, - - - [red]), (532) surfaces (◆, - · - [green]), and M12 clusters (▲, · · · [blue]). (a) The scaling of the  $O_2$  adsorption energy  $E_{O_2}$  with the O adsorption energy  $E_O$ . (b) Calculated transition state energies for  $O_2$  dissociation  $E_{TS3}$  (R3) as a function of O adsorption energy  $E_O$ . (c) Calculated transition state energies for adsorbed CO reacting with adsorbed O  $E_{TS4}$  (R4) as a function of the sum of the O and CO adsorption energies,  $E_O + E_{CO}$ . (d) Calculated transition state energies for adsorbed CO reacting with adsorbed  $O_2$   $E_{TS5}$  (R5) as a function of the sum of the O and CO adsorption energies,  $E_O + E_{CO}$ , with surface averaged BEP relation (—).

is then

$$\theta_*^{\max} \approx \frac{1}{1 + K_1 p_{CO} + K_2 p_{O_2}}$$

where we have assumed  $\theta_O \ll \theta_{CO}$ ,  $\theta_{O_2}$ , and  $\theta_*$ , which provides upper bounds for the respective coverages. Here  $p_{CO}$  and  $p_{O_2}$  are the partial pressures of  $O_2$  and CO in the gas phase, and the equilibrium constants  $K_i = k_i^+/k_i^-$  are determined from  $K_i = \exp(-(\Delta E_i - TS_i)/(k_B T))$ , where  $\Delta E_i$  is the chemisorption energy of CO,  $O_2$ , and O respectively.

## Results and Discussion

**Scaling Relations.** Our goal is to use the calculated adsorption energies and activation energies to study trends in catalytic rates. Therefore we begin by studying trends in these energies. We will show how scaling relations between different adsorption energies and between activation energies and adsorption energies (Brønsted–Evans–Polanyi (BEP) relations) limit the number of independent variables characterizing a particular metal and structure.<sup>45</sup>

In Figure 2a–d, scaling relations obtained for the CO oxidation reaction on the different surface structures of transition and noble metals are shown. In Figure 2a, we present the linear scaling between the adsorption energy of  $O_2$  and atomic oxygen, O. Further, we obtain BEP relations in Figure 2b–d showing a linear scaling between the adsorption energies of CO and O,  $E_{CO}$  and  $E_O$ , and the transition state energy for reactions R3–R5. In general, the data falls into families of linear relations, with one approximately linear relation for each structure of the catalyst. The differences in the lines reflect the structure-dependence of the different adsorption energies and reaction barriers. For the CO + O and CO +  $O_2$  reactions the different BEP lines are nearly indistinguishable. This implies that geometrical effects may be neglected. Note that even if there is only one BEP line for a particular elementary reaction for all

structures, there are still large differences in the adsorption and hence the activation energy for a given metal from one structure to the next. For instance, for Au the CO adsorption energy varies by  $\approx 1.0$  eV from the (111) surface to the M12 cluster.

The linear relations shown in Figure 2 mean that of the original six metal-dependent variables ( $E_{CO}$ ,  $E_{O_2}$ ,  $E_O$ ,  $E_{TS3}$ ,  $E_{TS4}$ , and  $E_{TS5}$ ) only two are independent. We choose for these two independent variables  $E_{CO}$  and  $E_O$ . We may thus calculate the Sabatier rate for CO oxidation as a function of these two parameters alone for each of the structures studied. This means that we rely on the linear relations in Figure 2 in the kinetics. These relations are not exact, but they clearly describe the trends for metals and structures quite well. We suggest that this provides a good basis for a study of trends in the catalytic activity.

**Volcanoes.** Figure 3a–d shows the Sabatier activity  $A_S = k_B T \ln(r_S/k_B T h^{-1})$  as a function of the adsorption energies of CO and O for the close-packed (111), stepped (211), and step-kinked (532) surfaces as well as for the M12 cluster. A 2D volcano results with a maximum for a particular value of  $E_{CO}$  and  $E_O$ , which represents the adsorption properties of the best catalyst. Note that the CO adsorption energy on Pd(111) has been corrected from the value reported in ref 35. An important observation is that in spite of the differences in the scaling relations in Figure 2, the volcanoes are all very similar for a given temperature. In particular, the position of the maximum in terms of  $E_{CO}$  and  $E_O$  hardly changes from one structure to the next. One reason for this structure independence is related to the relevant energy scale. It may be seen in Figure 3 that the maxima are quite broad. The width of the maximum, defined as the width of the contour where the rate is 1 order of magnitude lower than the maximum, is on the order of 0.5 eV. This gives a certain insensitivity of the results to the details of the energetics.

For each structure we have shown in Figure 3, the position of the different metals is defined by their  $(E_{CO}, E_O)$  coordinate. It should be observed that the Au point moves closer to the maximum in the order (111)  $\rightarrow$  (211)  $\rightarrow$  (532)  $\cdot \cdot$  (M12), while the Pt and Pd points move away in the same order. This is made even clearer in Figure 4, where we show how the  $(E_{CO}, E_O)$  points for different structures wander on an average of the different volcanoes. Here we have also added the points  $(E_{CO}, E_O)$  for the Pt55 and Au55 clusters. They clearly adhere very well to the same trends.

There are two main conclusions from this analysis. First, the rate of CO oxidation (under the idealized conditions considered here) is a clear function of the local geometry. At the low temperature conditions considered in Figure 3, Au steps, kinks, and small particles have a higher calculated rate than the close-packed surface.<sup>14</sup> This is in good agreement with experimental observations.<sup>31</sup> We note here that additional effects due to supports may also contribute to the enhanced catalytic activity of small Au particles. The present calculations suggest that there is also an intrinsic size dependence relating to the availability of the most reactive structures involving low-coordinated Au atoms. For the other metals there is also a dependence on size. At low temperature it is quite weak for Cu and Ag, and stronger for Pd and Pt. For the latter two metals the trend is that the intrinsic activity decreases with decreasing particle size. At higher temperatures the CO oxidation rate is largest on these metals. The increased temperature shifts the top of the volcano to stronger adsorption energies, hence in the direction of the platinum metals. Such effects have been observed both experimentally and theoretically.<sup>46–49</sup> This effect on the reactivity is,

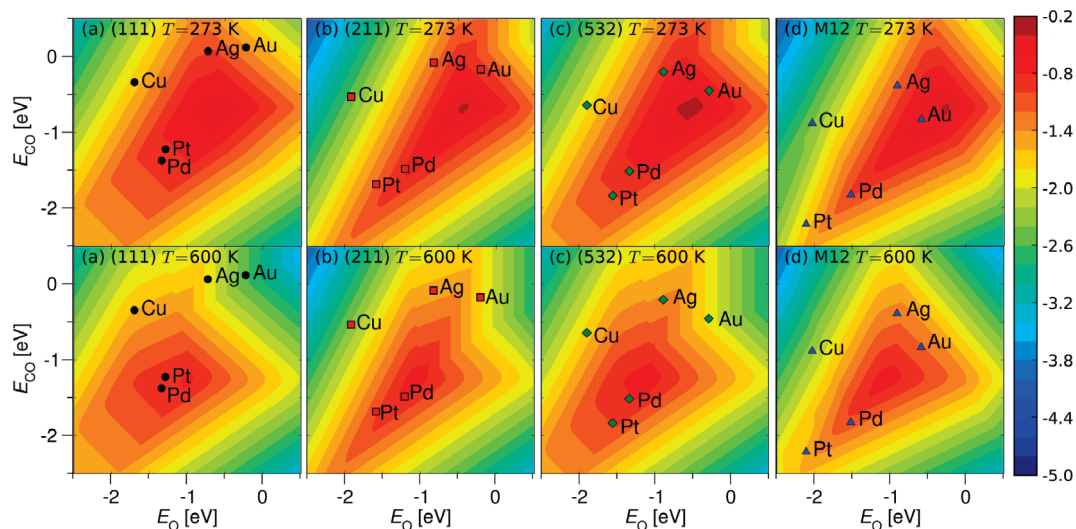


**Figure 3.** Contour plot of the Sabatier activity  $A_S = k_B T \ln(rs/k_B T h^{-1})$  in eV at (top) low temperature ( $T = 273$ ,  $p_{O_2} = 0.21$  bar,  $p_{CO} = 0.01$  bar) and (bottom) high temperature ( $T = 600$  K,  $p_{O_2} = 0.33$  bar,  $p_{CO} = 0.67$  bar), as a function of the CO and O adsorption energies on the (a) (111) surfaces (●, black), (b) (211) surfaces (■, red), (c) (532) surfaces (◆, green), and (d) M12 clusters (▲, blue). The values for several elemental metals are shown. The activity is calculated under typical experimental conditions for gold nanoparticles.

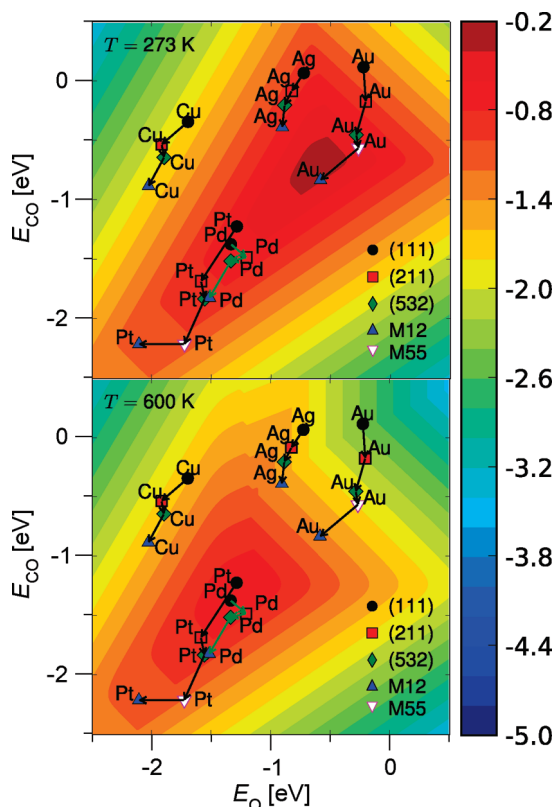


**Figure 4.** Contour plot of the “average” Sabatier activity  $A_S = k_B T \ln(rs/k_B T h^{-1})$  in eV at (top) low temperature ( $T = 273$  K,  $p_{O_2} = 0.21$  bar,  $p_{CO} = 0.01$  bar) and (bottom) high temperature ( $T = 600$  K,  $p_{O_2} = 0.33$  bar,  $p_{CO} = 0.67$  bar) from Figure 3 as a function of the CO and O adsorption energies on (111) surfaces (●, black), (211) surfaces (■, red), (532) surfaces (◆, green), M12-clusters (▲, blue), and M55-clusters (▼, magenta). The values for several elemental metals are shown. The activity is calculated under typical experimental conditions for gold nanoparticles.

however, quite weak. For platinum metals, the reaction rate for small nanoparticles may still be higher due to a significantly larger surface area per unit mass of catalyst. Additionally, mass and heat transfer could play an important role.

The other conclusion is that the main effect behind the structure variation is related to the strength of the adsorbate-

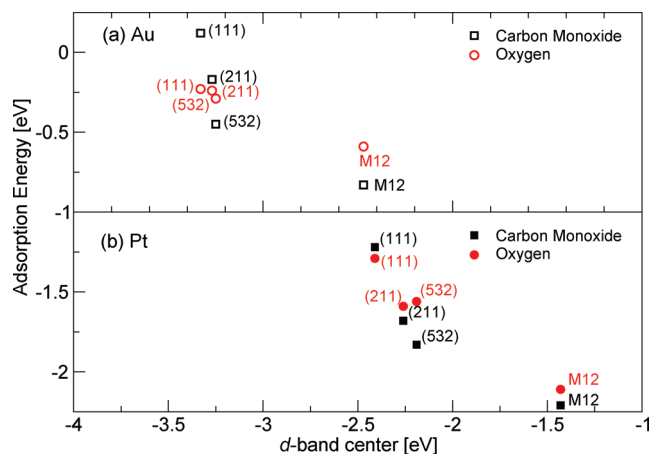


**Figure 5.** Adsorption energy  $E_{CO}$  and  $E_O$  versus d-band center for (111) surfaces, (211) surfaces, (532) surfaces, and M12 clusters of (a) Au (open black square, open red circle) and (b) Pt (solid black square, solid red circle).

metal bond at different structures. This effect is not geometrical, since the volcanoes for different structures are not very different. Rather it is connected to the variation in the bond strength of the different adsorbates as the structure is changed.

**Electronic Effects.** It was shown above that the structure-induced change in the intrinsic catalytic activity for CO oxidation on a number of metals is determined by the structure dependence in the adsorbate–surface interactions. We will now discuss the electronic origin of this effect.

In Figure 5 we show the variation in the adsorption energy of O and CO with the d-band center of the surface atoms. The d-band center is the average energy of the d states. Here it is defined as the density of states of the metal atoms to which CO and O bind, projected onto the d states of these metal atoms. The energy is taken relative to the Fermi energy. According to the d-band model<sup>50</sup> the strength of the adsorption bond should increase as the d states are shifted up in energy. This is also what is observed in Figure 5, for both the Pt and the Au clusters. The effect is stronger for Pt, since here the d states are higher up in energy and the bond strength is larger. The results illustrate the simple rule of thumb that the lower the metal coordination

number, the higher the d states are in energy, and the stronger they interact with adsorbates.

## Conclusion

The main conclusions of the present computational study are the following. For the CO oxidation reaction over a range of metal surfaces, we have shown that the scaling relations between different adsorption energies and between activation energies and adsorption energies are structure dependent. By studying different close-packed, stepped and kinked surfaces as well as very small clusters, we have shown that the main difference in catalytic activity between different surface geometries is related to the “openness” of the surface. More precisely, the coordination number of metal atoms at active sites provides this structure dependence. By including the stepped and kinked surfaces, we have filled the gap between close packed surfaces and nanoparticles discussed in ref 35. Further, the activity is found to be a quasicontinuous function of the openness of the surface. We have also provided detailed evidence that this effect is electronic in nature: the low coordinated metal atoms that bind the reactants most strongly have the highest energy metal d states.

The present analysis has been explicitly aimed at understanding trends in reactivity for different metals and surface structures. As such, we have not included coverage effects, particularly the effects of high oxygen coverage and oxidation. Only the intrinsic metal activity has been studied.

The results of the present analysis may be used to understand structural effects in supported catalysts. Since the number of low coordinated metal sites is a strong function of particle size, the geometrical effects studied here will translate directly into particle size effects for supported catalysts. The finding that the catalytic activity of Au atoms increases strongly as the metal coordination number of the Au atoms decreases may provide part of the explanation for the unusually high catalytic activity of Au nanoparticles. Since the number of low-coordinated Au atoms should scale with particle size,  $d$ , as  $d^{-2}$  (edges) or  $d^{-3}$  (corners), our analysis explains why such scaling has been found experimentally.<sup>18,46</sup>

In supported catalysts one effect of the support is to determine the particle size for a given catalyst preparation and a given set of reaction conditions. As discussed above, this will determine the activity of the catalyst. The support may also affect the shape of the active metal catalysts. This can also change the number of most active sites. The support may also interact so strongly with the catalysts that the most reactive sites are covered by it. This can decrease the number of low-coordinated sites. Finally, the support may play an active role by activating some of the reactants or by providing new sites at the perimeter between the metal and the support. While all these effects may contribute, the present analysis has identified the intrinsic geometrical effect associated with the metal for the CO oxidation reaction. This effect will always be present, but may be further augmented by additional effects.

**Acknowledgment.** The Center for Sustainable and Green Chemistry is supported by the Danish National Research Foundation and the Center for Atomic-Scale Materials Design is supported by the Lundbeck Foundation. In addition we thank the Danish Research Council for the Technical Sciences and the NABIIT program for financial support, and the Danish Center for Scientific Computing for computer time.

## References and Notes

- (1) Chen, M. S.; Cai, Y.; Yan, Z.; Gath, K. K.; Axnanda, S.; Goodman, D. W. *Surf. Sci.* **2007**, *601*, 5326–5331.
- (2) Nieuwenhuys, B. E. *Surf. Rev. Lett.* **1996**, *3*, 1869–1888.
- (3) Engel, T.; Ertl, G. *Adv. Catal.* **1979**, *28*, 1.
- (4) Campbell, C. T.; Ertl, G.; Kuipers, H.; Segner, J. *J. Chem. Phys.* **1980**, *73*, 5862.
- (5) Goodman, D. W.; Peden, C. H. F. *J. Phys. Chem.* **1986**, *90*, 4839.
- (6) Xu, J. Z.; Yates, J. T. *J. Chem. Phys.* **1993**, *99*, 725.
- (7) Szanyi, J.; Goodman, D. W. *J. Chem. Phys.* **2001**, *114*, 6382.
- (8) Valden, M.; Lai, X.; Goodman, D. W. *Science* **1998**, *281*, 1647–1649.
- (9) Chen, M.; Goodman, D. *Science* **2004**, *306*, 252–255.
- (10) Janssens, T. V. W.; Carlsson, A.; Puig-Molina, A.; Clausen, B. J. *Catal.* **2006**, *240*, 108–113.
- (11) Xu, C.; Su, J.; Xu, X.; Liu, P.; Zhao, H.; Tian, F.; Ding, Y. *J. Am. Chem. Soc.* **2007**, *129*, 42–43.
- (12) Xu, C.; Xu, X.; Su, J.; Ding, Y. *J. Catal.* **2007**, *252*, 243–248.
- (13) Grisel, R.; Weststrate, K.-J.; Gluhoi, A.; Nieuwenhuys, B. E. *Gold Bull.* **2002**, *35*, 39–45.
- (14) Mavrikakis, M.; Stoltze, P.; Nørskov, J. K. *Catal. Lett.* **2000**, *64*, 101–106.
- (15) Reuter, K.; Scheffler, M. *Phys. Rev. B* **2002**, *65*, 035406.
- (16) Liu, Z.-P.; Hu, P.; Alavi, A. *J. Am. Chem. Soc.* **2002**, *124*, 14770–14779.
- (17) Lopez, N.; Janssens, T. V. W.; Clausen, B. S.; Xu, Y.; Mavrikakis, M.; Bligaard, T.; Nørskov, J. K. *J. Catal.* **2004**, *223*, 232–235.
- (18) Janssens, T. V. W.; Clausen, B. S.; Hvolbæk, B.; Falsig, H.; Christensen, C. H.; Bligaard, T.; Nørskov, J. K. *Top. Catal.* **2007**, *44*, 15–26.
- (19) Haruta, M.; Kobayashi, T.; Sano, H.; Yamada, N. *Chem. Lett.* **1987**, 405–408.
- (20) Bond, G. C.; Thompson, D. T. *Catal. Rev.* **1999**, *41*, 319–388.
- (21) Wickham, D. T.; Parker, D. H.; Kastanas, G. N.; Lazaga, M. A.; Koel, B. E. *Prepr. Am. Chem. Soc. Div. Pet. Chem.* **1992**, *37*, 1034.
- (22) Bond, G. C.; Thompson, D. T. *Gold Bull.* **2000**, *33*, 41–51.
- (23) Bond, G. C.; Louis, C.; Thompson, D. T. *Catalysis by Gold*, 1st ed.; Imperial College Press: London, 2006.
- (24) Ricci, D.; Bongiorno, A.; Pacchioni, G.; Landman, U. *Phys. Rev. Lett.* **2006**, *97*, 036106.
- (25) van Bokhoven, J.; Louis, C.; Miller, J.; Tromp, M.; Safonova, O.; Glatzel, P. *Angew. Chem., Int. Ed.* **2006**, *45*, 4651–4654.
- (26) Grunwaldt, J.-D.; Kiener, C. W.; Baiker, A. *J. Catal.* **1999**, *181*, 223–232.
- (27) Shaikhutdinov, S.; Meyer, R.; Naschitzki, M.; Baumer, M.; Freund, H.-J. *Catal. Lett.* **2003**, *86*, 211–219.
- (28) Lemire, C.; Meyer, R.; Shaikhutdinov, S.; Freund, H.-J. *Angew. Chem., Int. Ed.* **2004**, *43*, 118–121.
- (29) Zanella, R.; Giorgio, S.; Shin, C.; Henry, C.; Louis, C. *J. Catal.* **2004**, *222*, 357–367.
- (30) Deng, X.; Min, B.; Guloy, A.; Friend, C. *J. Am. Chem. Soc.* **2005**, *127*, 9267–9270.
- (31) Walther, G.; Mowbray, D. J.; Jiang, T.; Jones, G.; Jensen, S.; Quaade, U.; Horch, S. *J. Catal.* **2008**, *280*, 86–92.
- (32) Haruta, M. *Catal. Today* **1997**, *36*, 153–166.
- (33) Sanchez, A.; Abbet, S.; Heiz, U.; Schneider, W.; Hakkinen, H.; Barnett, R.; Landman, U. *J. Phys. Chem. A* **1999**, *103*, 9573–9578.
- (34) Mills, G.; Gordon, M.; Metiu, H. *J. Chem. Phys.* **2003**, *118*, 4198–4205.
- (35) Falsig, H.; Hvolbæk, B.; Kristensen, I. S.; Jiang, T.; Bligaard, T.; Christensen, C. H.; Nørskov, J. K. *Angew. Chem., Int. Ed.* **2008**, *47*, 4835–4839.
- (36) Abrams, B. L.; Wilcoxon, J. P. *Crit. Rev. Solid State Mater. Sci.* **2005**, *30*, 153–182.
- (37) Wilcoxon, J. P.; Abrams, B. L. *Chem. Soc. Rev.* **2006**, *35*, 1162–1194.
- (38) Turner, M.; Golovko, V. B.; Vaughan, O. P. H.; Abdulkina, P.; Berenguier-Murcia, A.; Tikhov, M. S.; Johnson, B. F. G.; Lambert, R. M. *Nature* **2008**, *454*, 981.
- (39) Hammer, B.; Hansen, L. B.; Nørskov, J. K. *Phys. Rev. B* **1999**, *59*, 7413–7421.
- (40) Abild-Pedersen, F.; Andersson, M. P. *Surf. Sci.* **2007**, *601*, 1747–1753.
- (41) Nørskov, J. K.; Rossmeisl, J.; Logadottir, A.; Lindqvist, L.; Kitchin, J. R.; Bligaard, T.; Jonsson, H. *J. Phys. Chem. B* **2004**, *108*, 17886–17892.
- (42) Kurth, S.; Perdew, J. P.; Blaha, P. *Int. J. Quantum Chem.* **1999**, *75*, 889–909.
- (43) Bligaard, T.; Nørskov, J. K.; Dahl, S.; Matthiesen, J.; Christensen, C. H.; Sehested, J. *J. Catal.* **2004**, *224*, 206–217.
- (44) Atkins, P.; de Paula, J. *Physical Chemistry*, 8th ed.; Oxford University Press: Oxford, 2006.



(45) Nørskov, J. K.; Bligaard, T.; Logadottir, A.; Bahn, S.; Hansen, L. B.; Bollinger, M.; Benggaard, H.; Hammer, B.; Sljivancanin, Z.; Mavrikakis, M.; Xu, Y.; Dahl, S.; Jacobsen, C. J. H. *J. Catal.* **2002**, *209*, 275–278.

(46) Rashkeev, S. N.; Lupini, A. R.; Overbury, S. H.; Pennycook, S. J.; Pantelides, S. T. *Phys. Rev. B* **2007**, *76*, 035438.

(47) Becker, C.; Henry, C. R. *Surf. Sci.* **1996**, *352–354*, 457–462.

(48) Guerin, S.; Hayden, B. E.; Lee, C. E.; Mormiche, C.; Owen, J. R.; Russel, A. E. D.; Thomsett, B. T. *J. Comb. Chem.* **2004**, *6*, 149.

(49) Hayden, B. E.; Pletcher, D.; Suchsland, J.-P.; Williams, L. J. *Phys. Chem. Chem. Phys.* **2009**, *11*, 1564.

(50) Hammer, B.; Nørskov, J. K. *Surf. Sci.* **1995**, *343*, 211–220.

JP811185G

## **Paper IV**

# **Trends in the catalytic CO oxidation activity of nanoparticles**

**Hanne Falsig, Britt Hvolbæk, Iben S. Kristensen, Tao Jiang, Thomas Bligaard, Claus H. Christensen, Jens K. Nørskov**  
**Angew. Chem. Int. Ed. 47 4835 (2008)**

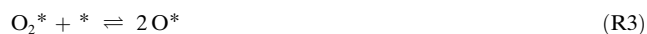
## Trends in the Catalytic CO Oxidation Activity of Nanoparticles\*\*

Hanne Falsig, Britt Hvolbæk, Iben S. Kristensen, Tao Jiang, Thomas Bligaard, Claus H. Christensen, and Jens K. Nørskov\*

Although extended gold surfaces are generally considered chemically inert<sup>[1,2]</sup> nanosized (< 5 nm) gold particles can be very effective catalysts for a number of oxidation reactions.<sup>[3–17]</sup> There are reports of similar size effects for silver catalysts.<sup>[18,19]</sup> The origin of the nanoeffects in the catalytic properties of these metals is widely debated,<sup>[15]</sup> and no consensus has been reached. Based on a set of density functional theory calculations of the full reaction pathway for CO oxidation over extended surfaces as well as over small nanoparticles of a number of metals, we show that although platinum and palladium are the most active catalysts for extended surfaces at high temperatures, gold is the most active for very small particles at low temperature. The calculations capture the special catalytic properties of nanosized particles observed experimentally, which allows the origin of the effect to be analyzed.

Herein, we focus on intrinsic metal effects; that is, we do not include additional possible effects that involve the support. It is not that such effects may not be important,<sup>[5,20,21]</sup> but it is useful to first establish the intrinsic metal effects,<sup>[15]</sup> in particular as it has been shown experimentally that nanostructured gold with no support is also catalytically active.<sup>[22,23]</sup> The key feature of our analysis is that we compare catalytic activities of different transition and noble metals for one specific reaction, the CO oxidation.

The CO oxidation reaction on close-packed fcc(111) surfaces was considered initially, which will give a dominant contribution to the total catalytic rate over large metal particles. We consider the following elementary reactions:



For the metals we consider herein, Reactions (R1) and (R2) are unactivated and fast, and we assume that these two reactions are in equilibrium. This means that we are limited to temperatures high enough that desorption is also fast. The possible formation of an oxide layer on the more reactive metals is neglected.

The forward and reverse rate constants of the Reactions (R3) and (R4) are given by  $k_i = \nu_i \exp[-\Delta G_{ai}/kT] = \nu_i \exp[-(E_{ai} - T\Delta S_{ai})/kT]$ , where  $\nu_i$  is a prefactor,  $E_{ai}$  is the activation energy,  $k$  is the Boltzmann constant, and  $T$  is the absolute temperature. The activation energies are  $E_a = \max(E_{\text{TS}} - E_{\text{IS}}, 0)$  where  $E_{\text{IS}}$  is the initial state energy and  $E_{\text{TS}}$  is the transition-state energy.  $\Delta S_{ai}$  is the entropy difference between the transition state and the initial state. The entropy of adsorbed species are assumed to be zero, and the gas-phase entropies are taken from Ref. [24]. The adsorption energies of the different species  $E_{\text{CO}}$ ,  $E_{\text{O}_2}$ , and  $E_{\text{O}}$  and the transition state energies are given with respect to the gas-phase molecules.

Assuming the prefactors and adsorption entropies are independent of the metal, there are five metal-dependent parameters determining the kinetics:  $E_{\text{CO}}$ ,  $E_{\text{O}_2}$ ,  $E_{\text{O}}$ ,  $E_{\text{TS3}}$ , and  $E_{\text{TS4}}$ . The transition-state energies are, however, found to scale linearly with the adsorption energies, as shown for  $E_{\text{TS3}}$  and  $E_{\text{TS4}}$  in Figure 1 a and b. Such Brønsted–Evans–Polanyi (BEP) relations are found quite generally for surface reactions.<sup>[25]</sup> Furthermore, the  $\text{O}_2$  adsorption energy scales with the O adsorption energy (Figure 1 c). This means that the adsorption energies  $E_{\text{CO}}$  and  $E_{\text{O}}$  can be viewed, to a first approximation, as the only independent variables characterizing the metal in the microkinetic model. Owing to the low number of elementary reactions, it is possible to find an analytical solution for this microkinetic model. Herein, we use instead the more general method of a so-called Sabatier analysis to find an upper bound to the overall reaction rate.<sup>[26]</sup>

The Sabatier rate<sup>[26]</sup> is the rate the reaction will have if all coverages are optimum for each elementary reaction step. Such conditions may not be obtainable in reality, but the Sabatier rate still provides an exact upper bound to the steady-state rate under any reaction conditions. The Sabatier rate is also an upper bound on the rate when islanding is included, as that will decrease the number of possible reaction centers to the length of the boundary between different phases.<sup>[27]</sup> The Sabatier rate thus forms a good measure of the intrinsic ability of a given metal surface to catalyze the reaction in question. The metal with the highest Sabatier rate is taken herein as being the best catalyst.

[\*] Dr. B. Hvolbæk, I. S. Kristensen, T. Jiang, Dr. T. Bligaard, Prof. J. K. Nørskov  
Center for Atomic-scale Materials Design, Department of Physics, Technical University of Denmark, DK-2800 Lyngby (Denmark)  
Fax: (+45)4593-2399  
E-mail: norskov@fysik.dtu.dk  
H. Falsig, Prof. C. H. Christensen  
Center for Sustainable and Green Chemistry, Department of Chemistry, Technical University of Denmark  
DK-2800 Lyngby (Denmark)

[\*\*] The Center for Sustainable and Green Chemistry is supported by the Danish National Research Foundation, and the Center for Atomic-scale Materials Design is supported by the Lundbeck Foundation. In addition we thank the Danish Research Council for the Technical Sciences and the NABIIT program for financial support, and Danish Center for Scientific Computing for computer time.

Supporting information for this article is available on the WWW under <http://dx.doi.org/10.1002/anie.200801479>.

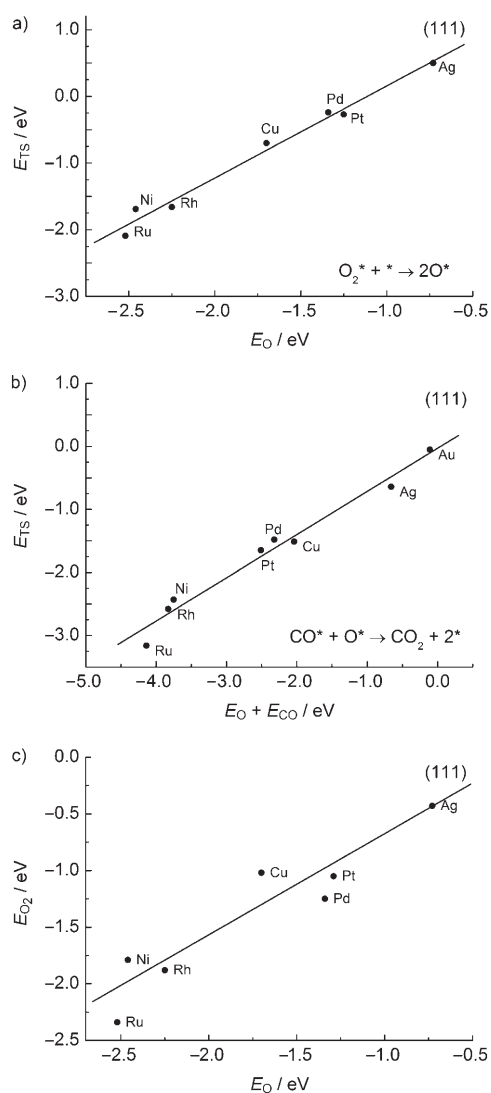


**Figure 1.** The BEP and scaling relations for different close-packed fcc(111)-surfaces. a) Calculated transition-state energies for  $\text{O}_2$  dissociation (R3) as a function of oxygen adsorption energy.  $E_{\text{TS}3} = 1.39 E_{\text{O}} + 1.56 \text{ eV}$ . b) Calculated transition-state energies for adsorbed CO reacting with adsorbed O (R4) as a function of the sum of the O and CO adsorption energies.  $E_{\text{TS}4} = 0.70(E_{\text{O}} + E_{\text{CO}}) + 0.02 \text{ eV}$ . c) The scaling of the  $\text{O}_2$  adsorption energy with the oxygen adsorption energy  $E_{\text{O}_2} = 0.89 E_{\text{O}} + 0.17 \text{ eV}$ . For Pt(111), the calculated reaction barrier  $E_{\text{a}} = E_{\text{TS}} - (E_{\text{CO}} + E_{\text{O}})$  for  $\text{CO}^* + \text{O}^* \rightarrow \text{CO}_2 + 2^*$  is 0.85 eV, in good agreement with calculations.<sup>[28,29]</sup>

The rate of reaction for (R3) and (R4) are maximized if the reverse reactions are neglected. The Sabatier rate is therefore calculated from the forward rates:

$$r_3^+ = \theta_{\text{O}_2} \theta_* k_3^+ = \theta_{\text{O}_2} \theta_* \nu_3 \exp[-(E_{\text{a}3} - T \Delta S_{\text{a}3})/k T] \quad (1)$$

$$r_4^+ = \theta_{\text{O}} \theta_{\text{CO}} k_4^+ = \theta_{\text{O}} \theta_{\text{CO}} \nu_4 \exp[-(E_{\text{a}4} - T \Delta S_{\text{a}4})/k T] \quad (2)$$

where  $\theta_{\text{O}_2}$  is the coverage of adsorbed oxygen molecules,  $\theta_{\text{O}}$  is the coverage of adsorbed atomic oxygen,  $\theta_{\text{CO}}$  is the coverage of adsorbed CO molecules, and  $\theta_*$  is the coverage of free sites of the surface. The coverages will depend on the

reaction conditions, temperature, reactant pressures, and conversion.

For the present case, the optimum coverages are found by first neglecting the coverage of atomic oxygen. Still assuming that (R1) and (R2) are in equilibrium, this gives:

$$\theta_*^{\text{max}} = \frac{1}{1 + K_1 p(\text{CO}) + K_2 p(\text{O}_2)} \quad (3)$$

where  $K_1$  and  $K_2$  are the equilibrium constants for (R1) and (R2), and  $p(\text{CO})$  and  $p(\text{O}_2)$  are the partial pressures of CO and  $\text{O}_2$ . The optimum coverages of CO and  $\text{O}_2$  have similar expressions, namely  $\theta_{\text{CO}}^{\text{max}} = K_1 p(\text{CO}) \theta_*$  and  $\theta_{\text{O}_2}^{\text{max}} = K_2 p(\text{O}_2) \theta_*$ .

The Sabatier rates of each of the Reactions (R3) and (R4) are found by using the forward rates from (1) and (2) with the coverages of  $\theta_*^{\text{max}}$ ,  $\theta_{\text{CO}}^{\text{max}}$  and  $\theta_{\text{O}_2}^{\text{max}}$  from (3), and the coverage of  $\theta_{\text{O}}^{\text{max}}$  set to one.

$$r_3^{\text{Smax}} = k_3^+ \theta_{\text{O}_2}^{\text{max}} \theta_*^{\text{max}} \quad (4)$$

$$r_4^{\text{Smax}} = k_4^+ \theta_{\text{CO}}^{\text{max}} \theta_{\text{O}}^{\text{max}} = k_4^+ \theta_{\text{CO}}^{\text{max}} \quad (5)$$

The Sabatier rate of forming  $\text{CO}_2$  is determined by the lowest of the Sabatier rates of Reaction (R3) and (R4):

$$r_s = \min\{2 r_3^{\text{Smax}}, r_4^{\text{Smax}}\} \quad (6)$$

where the factor of 2 stems from the stoichiometric number for (R3).

Figure 2 shows a contour plot of the Sabatier activity over close-packed surfaces. The Sabatier rate is calculated at  $T = 600 \text{ K}$ ,  $P_{\text{O}_2} = 0.33 \text{ bar}$  and  $P_{\text{CO}} = 0.67 \text{ bar}$ , corresponding to high-temperature CO oxidation conditions. The two-dimensional volcano plots show that, of the elemental metals, platinum and palladium are closest to the top. This agrees well with experimental evidence.<sup>[30]</sup> Platinum and palladium are

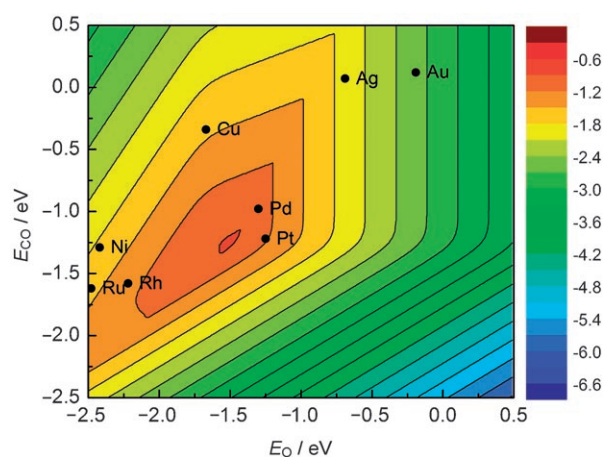
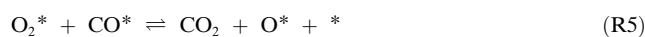


**Figure 2.** Contour plot of the Sabatier activity  $A_s = k T \ln[r_s/\nu]$  over close-packed surfaces as a function of  $E_{\text{CO}}$  and  $E_{\text{O}}$  ( $\nu$  is set to  $kT/h$ ) under high-temperature conditions ( $T = 600 \text{ K}$ ,  $P_{\text{O}_2} = 0.33 \text{ bar}$ , and  $P_{\text{CO}} = 0.67 \text{ bar}$ ). The values for different elemental metals can be taken from their indicated positions.

excellent CO oxidation catalysts, used for example in car exhaust after-treatment. This result is completely in line with DFT calculations and kinetic modeling by Grabow et al.<sup>[31]</sup> showing that at low temperatures, platinum without strain has a higher activity than either compressed (weaker bond energies) or expanded (stronger bond energies) platinum surfaces.

The reactivity of nanoparticles was then investigated. One important feature of nanoparticles is that the relative fraction of low-coordinate corner atoms to surface atoms is very large.<sup>[15,32]</sup> We concentrate herein on the reactivity of corner atoms, and model these by carrying out calculations for metal clusters containing twelve atoms, in the structure shown as inserts in Figure 3. All the twelve atoms in the cluster are held fixed with a lattice constant corresponding to the bulk value to mimic a geometrically constrained corner of a larger cluster, such as those in the range 2–5 nm studied experimentally. The calculations are thus more intended to model a general corner site on nanoparticles than specifically a twelve-atom cluster, as such small clusters will have much larger structural flexibility.<sup>[33]</sup>

It turns out that adsorption is considerably more exothermic on the twelve-atom clusters than on the close-packed surfaces. This makes it important to include another elementary reaction, as the coverage of molecular O<sub>2</sub> may be large enough such that an associative mechanism<sup>[34]</sup> may be important:



For the (111) surfaces, the weak bonding of O<sub>2</sub> combined with the reaction barrier for the process makes it unimportant for platinum<sup>[27]</sup> and less reactive metals.<sup>[35]</sup>

As for the fcc(111) surface, correlations between the transition state energies,  $E_{\text{TS3}}$ ,  $E_{\text{TS4}}$ , and  $E_{\text{TS5}}$ , and the binding energies,  $E_{\text{O}}$  and  $E_{\text{CO}}$ , are found for the twelve-atom cluster. A scaling between  $E_{\text{O}_2}$  and  $E_{\text{O}}$  is also found. These relations are shown in Figure 3. The linear relations are similar to those of the close-packed surfaces (Figure 1), except that the adsorption energy axis has shifted. The adsorption energy of both CO and O are substantially more negative (exothermic adsorption) on the corner sites than on the close packed surfaces; compare for example, the adsorption energy of O on the (111) surfaces to those on the twelve-atom cluster: on the latter the bond is stronger by of the order 0.5 eV. The same trend is seen for molecular CO adsorption.

The expressions for the optimum coverages and the Sabatier rate for (R3) and (R4) are the same as for the fcc(111) surface. For (R5), the Sabatier rate is:

$$r_5^{\text{Smax}} = k_5^+ \theta_{\text{CO}}^{\text{max}} \theta_{\text{O}_2}^{\text{max}} \quad (7)$$

Both Reaction (R3) and (R5) dissociate O<sub>2</sub>, and can be followed by Reaction (R4) creating CO<sub>2</sub>. The Sabatier activity is therefore given by:

$$r_5 = \max\{2 \min\{r_5^{\text{Smax}}, r_4^{\text{Smax}}\}, \min\{2 r_3^{\text{Smax}}, r_4^{\text{Smax}}\}\} \quad (8)$$

Figure 4 shows the contour plot of the Sabatier activity,

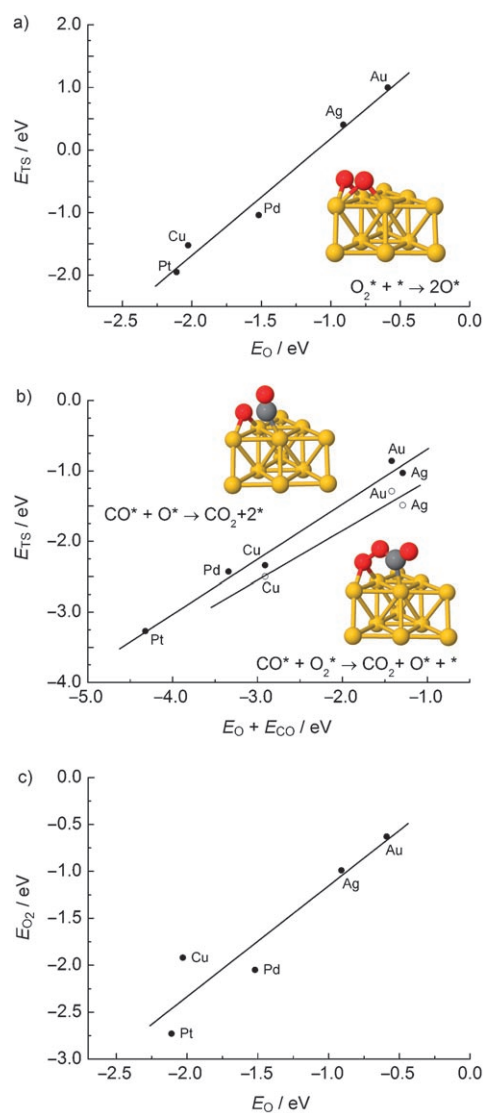


**Figure 3.** The BEP relations and scaling relation for different twelve-atom clusters. a) Calculated transition-state energies for O<sub>2</sub> dissociation (R3) as a function of oxygen adsorption energy.  $E_{\text{TS3}} = 1.87 E_{\text{O}} + 2.04$  eV. b) Calculated transition-state energies for adsorbed CO reacting with adsorbed O (R4) and O<sub>2</sub> (R5) as a function of the sum of the O and CO adsorption energies.  $E_{\text{TS4}} = 0.78 \cdot (E_{\text{O}} + E_{\text{CO}}) + 0.09$  eV and  $E_{\text{TS5}} = 0.70(E_{\text{O}} + E_{\text{CO}}) - 0.44$  eV. c) The scaling of the O<sub>2</sub> adsorption energy with the O adsorption energy  $E_{\text{O}_2} = 1.18 E_{\text{O}} + 0.03$  eV. Transition states for the reactions on the Au<sub>12</sub> cluster are shown as inserts.

$A_5 = k T \ln[r_5/\nu]$ . In this case, gold is closest to the top, followed by palladium and silver.

The results in Figure 2 and Figure 4 are in good agreement with available experimental observations.<sup>[3,32]</sup> It shows that the relative activities of different metals can be theoretically estimated, and it provides a clear picture of the catalyst properties determining the best catalysts in terms of the adsorption energies of the intermediates. The volcano plots of Figure 2 and Figure 4 can be viewed as an illustration of the Sabatier principle, with the important new feature that we know which adsorption energy that provides the optimum

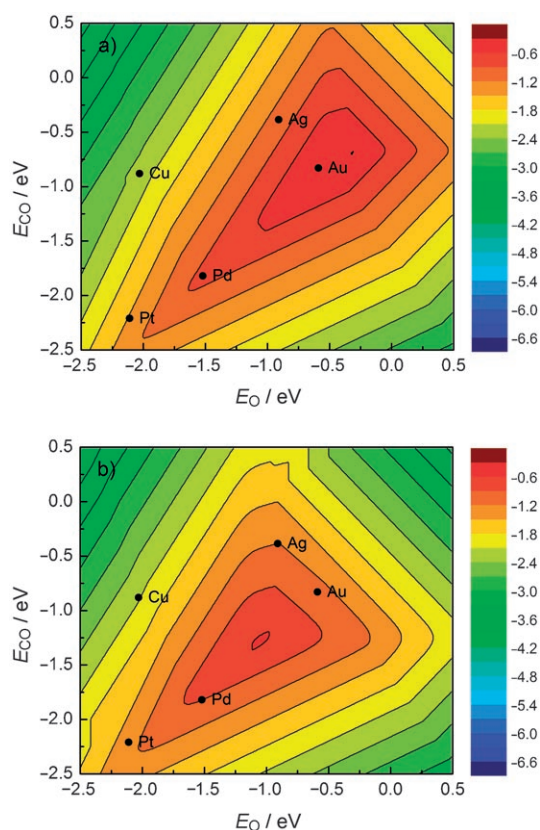


**Figure 4.** Contour plot of the Sabatier rate as a function of the CO and O adsorption energies on the twelve-atom clusters. The values for some elemental metals are shown. a) The activity under typical experimental conditions for CO oxidation by gold nanoparticles ( $T=273$  K,  $P_{O_2}=0.21$  bar, and  $P_{CO}=0.01$ ) and b) the activity under high-temperature conditions ( $T=600$  K,  $P_{O_2}=0.33$  bar, and  $P_{CO}=0.67$  bar).

catalyst. The position of the maximum in terms of adsorption energies depends slightly on the structure, which is related to the fact that the relationship between adsorption energy and activation energy is somewhat structure dependent. More importantly, it can be seen that the metals corresponding to a particular adsorption energy shift substantially depending on the coordination number of the metal atom. This is true for all the metals considered, and it is the dominant reason for gold becoming the best elemental catalyst for the low-coordinate sites. The shift is of the same order of magnitude as the difference between neighboring metals in the periodic table, explaining why it appears as if the top of the volcano has shifted by a little less than one place to the right in the periodic table from Figure 2 to Figure 4.

Comparing the volcanoes in Figure 2 and Figure 4, it is clear that for gold, the corner atoms will dominate over the close-packed surfaces for even quite large particles, as the value of  $r_5$  is many orders of magnitude larger in this case. For platinum, on the other hand, the difference is only about an order of magnitude. It should be noted that even for platinum, small particles could still be more active than larger ones, but only because the surface area per mass of catalyst is larger (scaling as  $d^{-1}$ ).

The present analysis suggests that the more noble metals move to the maximum in the reactivity volcano when lower-coordinated metal atoms serve as active sites for the reaction. It suggests that similar results could be found for other reactions. For oxidation reactions, the best extended surface catalysts are already quite noble: platinum and palladium, and gold is the next, less reactive metal. For reactions involving less reactive molecules, such as  $N_2$ , we would expect that the best nanoparticle catalysts would not be gold but metals just to the right in the periodic table of the most active metals (ruthenium, iron) for this reaction, for example, cobalt or nickel. It is therefore possible that pronounced nanoeffects in catalysis is not restricted to gold.

In summary, we have modeled the special catalytic properties of nanosized particles observed experimentally, and analyzed the origin of the effect. The ability of the metal atoms to activate reactants change substantially as the coordination number of the active metal site is reduced at corners of metal particles. This model supports the hypothesis that part of the observed reactivity of gold nanoparticles is independent of the substrate.

Received: March 23, 2008

Published online: May 21, 2008

**Keywords:** carbon monoxide · density functional calculations · gold · heterogeneous catalysis · nanostructures

- [1] D. T. Wickham, D. H. Parker, G. N. Kastanas, M. A. Lazaga, B. E. Koel, *Prepr. Am. Chem. Soc. Div. Pet. Chem.* **1992**, 37, 1034.
- [2] B. Hammer, J. K. Nørskov, *Nature* **1995**, 376, 238–240.
- [3] M. Haruta, T. Kobayashi, H. Sano, N. Yamada, *Chem. Lett.* **1987**, 405–408.
- [4] M. Valden, X. Lai, D. W. Goodman, *Science* **1998**, 281, 1647–1650.
- [5] G. C. Bond, D. T. Thomson, *Catal. Rev. Sci. Eng.* **1999**, 41, 319–388.
- [6] M. A. P. Dekkers, M. J. Lippits, B. E. Nieuwenhuys, *Catal. Today* **1999**, 54, 381.
- [7] S. Carrettin, P. McMorn, P. Johnston, K. Griffin, G. J. Hutchings, *Chem. Commun.* **2002**, 696–697.
- [8] S. Schimpf, M. Lucas, C. Mohr, U. Rodemerck, A. Brückner, J. Radnik, H. Hofmeister, P. Claus, *Catal. Today* **2002**, 72, 63–78.
- [9] S. Carrettin, P. McMorn, P. Johnston, K. Griffin, C. J. Kiely, G. A. Attard, G. J. Hutchings, *Top. Catal.* **2004**, 27, 131–136.
- [10] R. Meyer, C. Lemire, S. Shaikhutdinov, H. J. Freund, *Gold Bull.* **2004**, 37, 72–133.
- [11] A. Abad, P. Concepcion, A. Corma, H. Garcia, *Angew. Chem.* **2005**, 117, 4134–4137; *Angew. Chem. Int. Ed.* **2005**, 44, 4066–4069.
- [12] A. C. Gluhoi, N. Bogdanchikova, B. E. Nieuwenhuys, *J. Catal.* **2005**, 229, 154–162.
- [13] M. D. Hughes et al., *Nature* **2005**, 437, 1132–1135.
- [14] T. A. Nijhuis, M. Makkee, J. A. Moulijn, B. M. Weckhuysen, *Ind. Eng. Chem. Res.* **2006**, 45, 3447–3459.
- [15] a) T. V. W. Janssens, B. S. Clausen, B. Hvolbæk, H. Falsig, C. H. Christensen, T. Bligaard, J. K. Nørskov, *Top. Catal.* **2007**, 44, 15–26; b) N. Lopez, T. V. W. Janssens, B. S. Clausen, Y. Xu, M. Mavrikakis, T. Bligaard, J. K. Nørskov, *J. Catal.* **2004**, 223, 232–235.
- [16] C. H. Christensen, B. Jørgensen, J. Rass-Hansen, K. Egeblad, R. Madsen, S. K. Klitgaard, S. M. Hansen, M. R. Hansen, H. C.

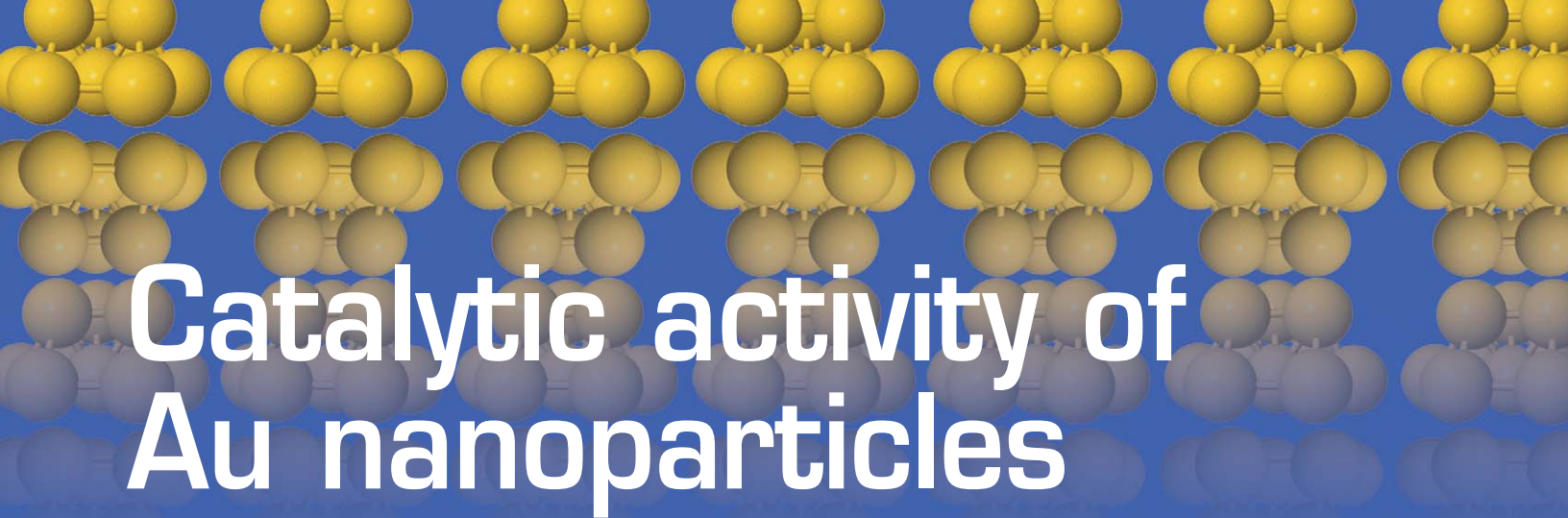
- Andersen, A. Riisager, *Angew. Chem.* **2006**, *118*, 4764–4767; *Angew. Chem. Int. Ed.* **2006**, *45*, 4648–4651.
- [17] R. Burch, *Phys. Chem. Chem. Phys.* **2006**, *8*, 5483–5500.
- [18] M. J. Lippits, A. C. Gluhoi, B. E. Nieuwenhuys, *Top. Catal.* **2007**, *44*, 159–165.
- [19] L. Gang, B. G. Anderson, J. van Grondelle, R. A. van Santen, *Appl. Catal. B* **2003**, *40*, 101–110.
- [20] M. Haruta, *Catal. Today* **1997**, *36*, 153–166.
- [21] B. Hammer, *Top. Catal.* **2006**, *37*, 3–16.
- [22] C. Xu, J. Su, X. Xu, P. Liu, H. Zhao, F. Tian, Y. Ding, *J. Am. Chem. Soc.* **2007**, *129*, 42–43.
- [23] B. Jürgens, C. Kübel, C. Schultz, T. Nowitzki, V. Zielasek, J. Biener, M. M. Biener, A. V. Hamza, M. Bäumer, *Gold Bull.* **2007**, *40*, 142–148.
- [24] P. Atkins, J. de Paula, *J. Physical Chemistry*, 8th ed. Oxford University Press, Oxford, **2006**.
- [25] J. K. Nørskov et al., *J. Catal.* **2002**, *209*, 275–278.
- [26] T. Bligaard, J. K. Nørskov, S. Dahl, J. Matthiesen, C. H. Christensen, J. Sehested, *J. Catal.* **2004**, *224*, 206–217.
- [27] J. Wintterlin, S. Völkening, T. V. W. Janssens, T. Zambelli, G. Ertl, *Science* **1997**, *278*, 1931–1933.
- [28] Z.-P. Liu, P. Hu, *Top. Catal.* **2004**, *28*, 71–78.
- [29] A. Eichler, J. Hafner, *Surf. Sci.* **1999**, *433*, 58–62.
- [30] B. E. Nieuwenhuys, *Surf. Rev. Lett.* **1996**, *3*, 1869–1888.
- [31] L. Grabow, Y. Xu, M. Mavrikakis, *Phys. Chem. Chem. Phys.* **2006**, *8*, 3369–3374.
- [32] A. Carlsson, A. Puig-Molina, T. V. W. Janssens, *J. Phys. Chem. B* **2006**, *110*, 5286–5293.
- [33] G. Mills, M. S. Gordon, H. Metiu, *J. Chem. Phys.* **2003**, *118*, 4198–4205.
- [34] Z.-P. Liu, P. Hu, A. Alavi, *J. Am. Chem. Soc.* **2002**, *124*, 14770–14779.
- [35] L. M. Molina, B. Hammer, *Phys. Rev. B* **2004**, *69*, 155424.

## **Paper V**

### **Catalytic activity of Au nanoparticles**

**Britt Hvolbæk, Ton V. W. Janssens, Bjerne S. Clausen, Hanne Falsig, Claus H. Christensen, Jens K. Nørskov, NANO TODAY 2 14 (2007)**





# Catalytic activity of Au nanoparticles

**Au is usually viewed as an inert metal, but surprisingly it has been found that Au nanoparticles less than 3–5 nm in diameter are catalytically active for several chemical reactions. We discuss the origin of this effect, focusing on the way in which the chemical activity of Au may change with particle size. We find that the fraction of low-coordinated Au atoms scales approximately with the catalytic activity, suggesting that atoms on the corners and edges of Au nanoparticles are the active sites. This effect is explained using density functional calculations.**

**Britt Hvolbæk<sup>1</sup>, Ton V. W. Janssens<sup>2</sup>, Bjerne S. Clausen<sup>2</sup>, Hanne Falsig<sup>3</sup>, Claus H. Christensen<sup>3</sup>, and Jens K. Nørskov<sup>1\*</sup>**

<sup>1</sup>Center for Atomic-scale Materials Design, Department of Physics, NanoDTU, Technical University of Denmark, DK-2800 Lyngby, Denmark

<sup>2</sup>Haldor Topsøe A/S, Nymøllevej 55, DK-2800 Lyngby, Denmark

<sup>3</sup>Center for Sustainable and Green chemistry, Department of Chemistry, NanoDTU, Technical University of Denmark, DK-2800 Lyngby, Denmark.

\*E-mail: [norskov@fysik.dtu.dk](mailto:norskov@fysik.dtu.dk)

Catalysts are widely used in the large-scale manufacture of chemicals and in the production of fine chemicals and pharmaceuticals. Fuel processing is a good example: the gasoline that we use in our cars requires at least ten different catalysts during its transformation from crude oil. Environmental technologies also rely heavily on catalysts; the best known example being the catalytic converter in the exhaust of every car. It is estimated that more than 20% of the gross national product (GNP) of industrial countries relies in one way or another on catalysis<sup>1</sup>.

In heterogeneous catalysis, the reacting molecules adsorb on the catalytically active solid surface. Chemical bonds are broken and formed on the surface and eventually the products are released back into the liquid or gas phase. Many of the heterogeneous catalysts used in industry today consist of small particles of a catalytically

active material, typically with a diameter of 1–10 nm, anchored on a porous support. The use of nanoparticles results in a large contact area between the active material of the catalyst and the surrounding gas or liquid phase. This ensures that the catalytic material is used effectively. One of the interesting scientific and technological challenges associated with the use of nanoparticles as catalysts is the understanding of how the composition and atomic-scale structure of nanoparticles produce the best catalytic activity. The second challenge is to synthesize these particles with maximum control over the composition and structure. Modern nanotechnology methods clearly offer great potential for future developments in both characterization and synthesis of heterogeneous catalysts based on supported nanoparticles.

Maximizing the surface area is not the only reason for using nanoparticles as heterogeneous catalysts. Au is usually considered

chemically inert<sup>2-4</sup>, but in 1987 Haruta *et al.*<sup>5</sup> showed that nanosized (<5 nm) Au particles can be very effective catalysts. This indicates that the catalytic properties of a particular material can be dramatically influenced by the particle size. The fact that Au particles with diameters of about 5 nm or less have unique catalytic properties has initiated a search both for an explanation of this quite unexpected effect and for chemical reactions that are catalyzed by Au<sup>5-34</sup>. In some cases, catalysts based on nanosized Au particles allow a significantly lower reaction temperature than used in existing processes, which is promising for the development of energy efficient processes<sup>35-38</sup>.

Here we discuss some of the reasons why small Au particles are catalytically active. Several explanations for the catalytic activity of such particles have been proposed, including quantum size effects<sup>10,11,39-41</sup>, charge transfer to and from the support<sup>42-44</sup> or support-induced strain<sup>45</sup>, oxygen spill-over to and from the support<sup>12,46-55</sup>, the Au oxidation state<sup>27,56-72</sup>, and the role of very low-coordinated Au atoms in nanoparticles<sup>34,38,45,73-84</sup>. It is likely that several of the aforementioned effects occur simultaneously. In this review, we concentrate on some of the effects that are associated with the particle size alone. These will always be present, independent of the support material.

## The reactivity of Au and Au nanoparticles

The ability of a metal surface to form bonds with a gas is a measure of how noble it is. The nobility of a metal is well illustrated by the ability of the surface of the metal to oxidize, that is, to chemisorb oxygen dissociatively. Fig. 1 shows calculated oxygen chemisorption energies on a selection of transition metals<sup>85</sup>. It can be seen that the metals located above and to the left of Au in the periodic table have increasingly large chemisorption energies, and that the metals neighboring Au bind oxygen weakly. Au is the only metal with an

<b>Cr</b>	<b>Mn</b>	<b>Fe</b>	<b>Co</b>	<b>Ni</b>	<b>Cu</b>
		-6,30	-5,07	-3,90	-2,51
<b>Mo</b>	<b>Tc</b>	<b>Ru</b>	<b>Rh</b>	<b>Pd</b>	<b>Ag</b>
-7,48		-4,62	-4,03	-1,20	-0,65
<b>W</b>	<b>Re</b>	<b>Os</b>	<b>Ir</b>	<b>Pt</b>	<b>Au</b>
-8,62			-4,65	-2,17	+0,54

Fig. 1 The dissociative chemisorption energies for oxygen on transition metal surfaces with respect to a molecule in vacuum calculated by density functional theory (DFT). All results are for adsorption at either a body-centered cubic (210) surface (for Fe, Mo, W) or a face-centered cubic (211) surface (other metals)<sup>85</sup>.

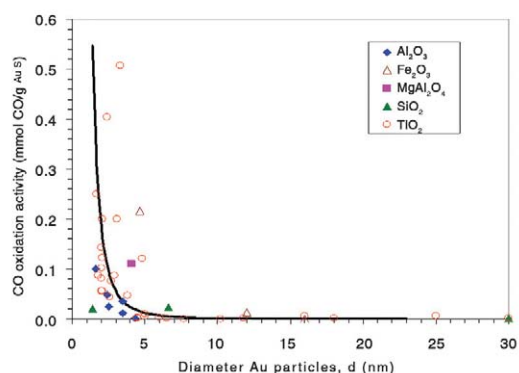


Fig. 2 Reported catalytic activities (in  $\text{mmol/g}_{\text{Au}} \text{ s}$ , left axis) for CO oxidation at 273 K as a function of Au particle size ( $d$ , in nanometers) for different support materials<sup>14,23,53,55,80,83,88-94</sup>. The supports are indicated by the symbol shape: open symbols correspond to reducible supports, closed symbols to irreducible supports. The solid curve shows the calculated fraction of atoms located at the corners of nanoparticles as a function of particle diameter for uniform particles shaped as the top half of a regular cuboctahedron (see also Fig. 5). (Adapted from<sup>34,80</sup>.)

endothermic chemisorption energy, which implies that it does not bind oxygen at all. This illustrates the well-known fact that Au is inert in an oxygen atmosphere<sup>86</sup>.

The trends in Fig. 1 can be understood by considering the chemical bond that forms as a result of the coupling of the oxygen valence states and the metal  $d$ -states in the so-called  $d$ -band model<sup>4,87</sup>. Au has  $d$ -states so low in energy that the interaction with oxygen  $2p$ -states is net repulsive. It is therefore unlikely that Au should be a good catalyst for an oxidation reaction. Nevertheless, the oxidation of CO (as it takes place over Pt-based catalysts in an automotive exhaust system) is one of the reactions where Au nanoparticles are a very good catalyst, even at room temperature. This is illustrated in Fig. 2, which is a compilation of experimental data of the CO oxidation activity as a function of the size of Au nanoparticle catalysts with different support materials<sup>14,23,53,55,80,83,88-94</sup>. It is clear that the activity is strongly dependent on the size of the Au nanoparticles, and that only catalysts with Au particles below 5 nm show catalytic activity. Furthermore, it can also be seen that the activity varies depending on the support. These effects are clearly important, but the results of Fig. 2 indicate that the most important effect is that of size. In this review, therefore, we concentrate on the intrinsic catalytic activity of Au particles bearing in mind that there are additional effects to consider in order to develop a complete picture of Au catalysis.

## Density functional theory simulations

To investigate why the size of Au nanoparticles has such a significant influence on the catalytic activity, we apply density functional theory calculations (DFT) to simulate the behavior of adsorbed molecules on a Au nanoparticle. Rather than simulating a Au cluster of 3–5 nm with thousands of atoms, we simulate a ten atom cluster (as shown in the insert in Fig. 3). We do not include a substrate in the simulations either,

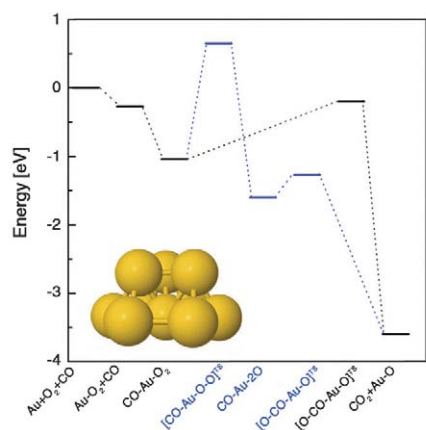


Fig. 3 Calculated reaction energies for CO oxidation on an Au<sub>10</sub> cluster (shown in insert). The lower layer of the cluster is kept fixed in the direction perpendicular to the support. Two reaction routes are shown: one dissociates O<sub>2</sub> before reaction with CO to form CO<sub>2</sub>, and the other reacts molecular O<sub>2</sub> directly with CO.

so the results originate only from the Au nanoparticles themselves. This is clearly an oversimplification of a real catalytic system, but is adequate to illustrate the effect of the particle size qualitatively. We consider below the CO oxidation as a test reaction.

The calculated energy diagram of two possible routes of CO oxidation is shown in Fig. 3<sup>34,75</sup>. One route dissociates O<sub>2</sub> before reacting with CO to form CO<sub>2</sub>; the other is a reaction between molecular O<sub>2</sub> and CO. The results indicate that CO oxidation is possible at room temperature. It can be seen that the reaction between molecular O<sub>2</sub> and CO is favored – it requires considerably lower activation energy than the reactions involving dissociation of O<sub>2</sub><sup>48</sup>. The single adsorbed O-atom left over from the reaction between O<sub>2</sub> and CO will react with another CO following the last half of the other route.

The energy diagram also reveals what could be an important clue to understanding the ability of Au nanoparticles to act as a catalyst: both O<sub>2</sub>, O, and CO bind to the surface of the cluster. This is in sharp contrast to extended Au surfaces (see, for example, Fig. 1). It turns out that a useful way of characterizing the difference between Au nanoparticles and extended Au surfaces is by considering the metal coordination number of the Au atoms to which the reactants (O<sub>2</sub>, O, or CO) bond (Fig. 4). Au atoms on a close-packed surface have nine Au neighbors, at steps on the surface the coordination number is seven, but at the corners of a small particle it can be as low as three to four. Fig. 4 shows that the binding energy decreases approximately linearly with decreasing coordination number<sup>34,80</sup>.

Small particles have a relatively large number of low-coordinated Au atoms, which are located at the edges and, in particular, at the corners of particles. The simple analysis above indicates that these Au atoms are able to bind CO and oxygen, which is a prerequisite for a catalytic reaction. It is therefore conceivable that at these sites the CO oxidation reaction is possible at room temperature – the barriers are

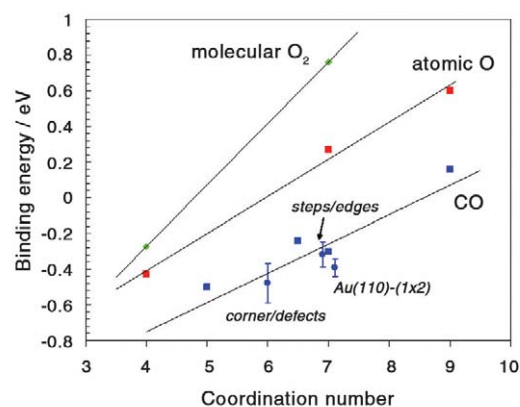


Fig. 4 The correlation between the binding energies for O<sub>2</sub>, O, and CO on Au and the coordination number of the Au atoms in different surfaces and clusters. The binding energies are calculated using DFT and the experimental values are from elsewhere<sup>34,102</sup>. The superscript TS denotes the transition state of the reaction.

small and, importantly, the intermediates and CO<sub>2</sub> that are formed are only weakly bound, so it is not necessary to have a high temperature to keep parts of the surface free.

If the low-coordinated corner sites are the active sites, then the catalytic activity should scale with the number of low-coordinated atoms in the nanoparticles, and not with the surface area. Fig. 5 shows a calculation of the fraction of atoms that are located at either corners, edges, or on surfaces in the top half of a truncated octahedron as a function of the particle diameter<sup>34</sup>. Clearly, the total number of surface atoms changes only slightly when the particle size decreases from 10 nm to 2 nm. However, the fraction of corners increases significantly when the particle size is less than 4 nm and scales approximately as  $d^{-3}$  as the diameter of the particles shrinks. The increase in the estimated fraction of corner atoms behavior coincides with a generally observed increase in CO oxidation activity with decreasing Au particle size

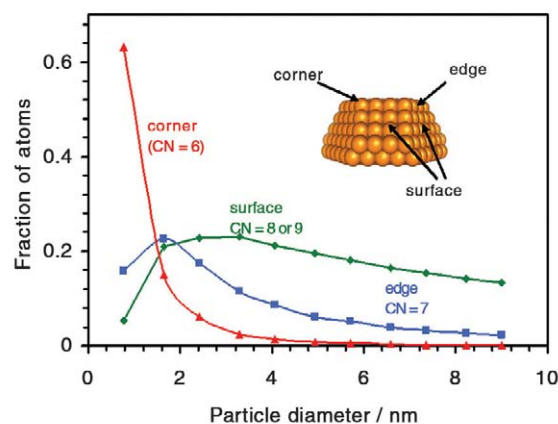


Fig. 5 Calculated fractions of Au atoms at corners (red), edges (blue), and crystal faces (green) in uniform nanoparticles consisting of the top half of a truncated octahedron as a function of Au particle diameter. The insert shows a truncated octahedron and the position of representative corner, edge, and surface atoms. (Reproduced with permission from<sup>34</sup>. © 2007 Springer.)

(Fig. 2). This supports the hypothesis that the total number of atoms located at the corners of the nanoparticles has a major influence on the activity of a supported Au catalyst.

## Experimental observations

The simulation results showing that chemisorption strength increases with decreasing coordination number is supported by a number of recent experiments. Temperature-programmed desorption (TPD) of CO on well-defined surfaces of Au and Au particles shows that the desorption temperature increases with decreasing coordination number<sup>34,77,95–97</sup>. This indicates that the chemisorption becomes stronger, in agreement with simulations. In fact, the estimated chemisorption energies are close to the values expected from calculations, as indicated in Fig. 4.

Experiments show that low-coordinated sites on a densely packed Au(111) surface produced by ion bombardment are also active for CO oxidation<sup>98</sup>. Recently, Xu *et al.*<sup>99</sup> have shown that unsupported nanoporous Au is an active catalyst for CO oxidation. The nanoporous Au catalyst, with pore sizes of less than 6 nm, is produced by etching away Ag from an Ag/Au alloy. The results provide additional support for the hypothesis that metallic Au is intrinsically catalytically active if the coordination number of the Au atoms is sufficiently low.

Evidence for the scaling of the catalytic activity of Au nanoparticles with the number of corner atoms has been provided by Overbury *et al.*<sup>93</sup>. They evaluated the dimensionality of the dominating active site by correlating the CO oxidation activity of a Au/TiO<sub>2</sub> catalyst with Au particle size by combining extended X-ray absorption fine structure (EXAFS) with *in situ* activity measurements. The particle size is varied by heating samples of the catalyst to different temperatures. This is done to eliminate possible variations in the preparation of different batches of catalyst. Fig. 6 shows the correlation for 4.5 wt.% and 7.2 wt.% Au at 273 K. The slope of the lines through the data is  $-2.1$  and  $-2.8$ , respectively. This indicates that the corners (slope:  $-3$ ) and to a lesser extent edge sites (slope:  $-2$ ) are the dominating site for 7.2 wt.% whereas edges and to a lesser extent corners contribute to the active site for 4.5 wt.%.

In studies by Janssens *et al.*<sup>34,83,100</sup>, a geometric model for Au particles on TiO<sub>2</sub>, MgAl<sub>2</sub>O<sub>4</sub>, and Al<sub>2</sub>O<sub>3</sub> supports was constructed based on scanning transmission electron microscopy (STEM) and EXAFS measurements. This allows an accurate count of the corner atoms in these supported catalysts. By comparing their catalytic activities, it has been found that the turn over frequency per corner atom for Au/TiO<sub>2</sub> and Au/MgAl<sub>2</sub>O<sub>4</sub> catalysts is the same, and any difference in catalytic activity between these two materials can therefore be entirely ascribed to differences in particle size and shape, which determine the total number of low-coordinated corner atoms. The turn over frequency per corner atom for Au/Al<sub>2</sub>O<sub>3</sub> is about a factor of four lower, which indicates an additional support effect in this case. This example nicely illustrates that the catalytic activity of Au nanoparticles is not

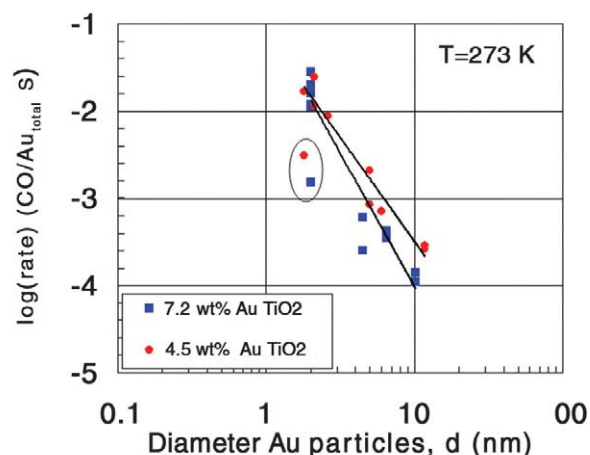


Fig. 6 Activity at 273 K as a function of Au particle diameter for two series of Au/TiO<sub>2</sub> catalysts containing 4.5 wt.% and 7.2 wt.% Au, respectively. The particle size has been varied by heat treatment at various temperatures between 423 K and 773 K. The rate is expressed per total amount of Au. Best power law fits to the data (excluding the two encircled points) are shown for each catalyst. (Reproduced with permission from<sup>93</sup>. © 2006 Elsevier.)

the result of a single contribution, but the result of a combination of different effects.

## Conclusions

Nanoscale effects are found throughout heterogeneous catalysis, but are perhaps best illustrated by the remarkable catalytic activity of Au nanoparticles. We still do not understand in detail the many effects that contribute to this activity, but in this review we have pointed to one very important effect: the increased reactivity of low-coordinated Au atoms. Such atoms are particularly abundant on the smallest nanometer-sized nanoparticles, and this may go a long way toward explaining the catalytic activity of such Au nanoparticles.

We are far from having explored all the possible applications of Au catalysis, but the system is extremely interesting. One intriguing property of Au nanoparticle catalysts is that they can catalyze several reactions at or even below room temperature. This could give energy savings in many catalytic processes, and provides an interesting analogue to enzyme catalysis, which can also take place at room temperature.

We also need to be able to synthesize Au nanoparticles in forms that are stable over long time periods. Understanding the interaction between Au particles and their support material is a key issue<sup>101</sup>. Finally, the question arises as to whether there are other classes of catalytic materials where nanoscale effects are as pronounced as for Au. We clearly need more insight. **nt**

## Acknowledgments

The Center for Atomic-scale Materials Design is supported by the Lundbeck Foundation. In addition, we thank the Danish Research Council for the Technical Sciences and the NABIIT program for financial support, and Danish Center for Scientific Computing for computer time.

REFERENCES

1. Maxwell, I., *Stud. Surf. Sci. Catal.* (1996) **101**, 1
2. Wickham, D. T., et al., *Prepr. – Am. Chem. Soc., Div. Pet. Chem.* (1992) **37**, 1034
3. Lazaga, M. A. A., et al., *Catalytic selective oxidation*. ACS Symposium Series (1993) **523**, 90
4. Hammer, B., and Nørskov, J. K., *Nature* (1995) **376**, 238
5. Haruta, M., et al., *Chem. Lett.* (1987) **16**, 405
6. Kobayashi, T., et al., *Sens. Actuators* (1988) **13**, 339
7. Haruta, M., et al., *J. Catal.* (1989) **115**, 301
8. Haruta, M., et al., *Stud. Surf. Sci. Catal.* (1989) **44**, 33
9. Haruta, M., et al., *J. Catal.* (1993) **144**, 175
10. Valden, M., et al., *Science* (1998) **281**, 1647
11. Valden, M., et al., *Catal. Lett.* (1998) **56**, 7
12. Bond, G. C., and Thomson, D. T., *Catal. Rev. – Sci. Eng.* (1999) **41**, 319
13. Hayashi, T., et al., *Prepr. – Am. Chem. Soc., Div. Pet. Chem.* (1996) **41**, 71
14. Haruta, M., *Stud. Surf. Sci. Catal.* (1997) **110**, 123
15. Dekkers, M. A. P., et al., *Catal. Today* (1999) **54**, 381
16. Kalvachev, Y. A., et al., *J. Catal.* (1999) **186**, 228
17. Uphade, B. S., et al., *Appl. Catal. A* (2000) **190**, 43
18. Grisel, R. J. H., and Nieuwenhuys, B. E., *Catal. Today* (2001) **64**, 69
19. Grisel, R. J. H., et al., *Top. Catal.* (2001) **16/17**, 425
20. Carrettin, S., et al., *Chem. Commun.* (2002), 696
21. Choudhary, T. V., and Goodman, D. W., *Top. Catal.* (2002) **21**, 25
22. Landon, P., et al., *Chem. Commun.* (2002), 2058
23. Schimpf, S., et al., *Catal. Today* (2002) **72**, 63
24. Carrettin, S., et al., *Phys. Chem. Chem. Phys.* (2003) **5**, 1329
25. Gluhoi, A. C., et al., *J. Catal.* (2003) **219**, 197
26. Okumura, M., et al., *Chem. Lett.* (2003) **32**, 822
27. Carrettin, S., et al., *Top. Catal.* (2004) **27**, 131
28. Meyer, R., et al., *Gold Bull.* (2004) **37**, 72
29. Abad, A., et al., *Angew. Chem. Int. Ed.* (2005) **44**, 4066
30. Gluhoi, A. C., et al., *J. Catal.* (2005) **229**, 154
31. Gluhoi, A. C., et al., *J. Catal.* (2005) **232**, 96
32. Hughes, M. D., et al., *Nature* (2005) **437**, 1132
33. Nijhuis, T. A., et al., *Ind. Eng. Chem. Res.* (2006) **45**, 3447
34. Janssens, T. V. W., et al., *Top. Catal.* (2007) **44**, 15
35. Kim, D. H., et al., *Catal. Lett.* (2004) **98**, 11
36. Lin, S. D., et al., *Catal. Today* (2004) **90**, 3
37. Christensen, C. H., et al., *Angew. Chem. Int. Ed.* (2006) **45**, 4648
38. Burch, R., *Phys. Chem. Chem. Phys.* (2006) **8**, 5483
39. Lai, X., et al., *Prog. Surf. Sci.* (1998) **59**, 25
40. Lai, X., et al., *J. Mol. Catal. A* (2000) **162**, 33
41. Yang, Z., et al., *Phys. Rev. B* (2000) **61**, 14066
42. Sanchez, A., et al., *J. Phys. Chem. A* (1999) **103**, 9573
43. Ricci, D., et al., *Phys. Rev. Lett.* (2006) **97**, 036106
44. van Bokhoven, J. A., et al., *Angew. Chem. Int. Ed.* (2006) **45**, 4651
45. Mavrikakis, M., et al., *Catal. Lett.* (2000) **64**, 101
46. Hammer, B., *Top. Catal.* (2006) **37**, 3
47. Liu, L. M., et al., *J. Am. Chem. Soc.* (2006) **128**, 4017
48. Liu, Z.-P., et al., *J. Am. Chem. Soc.* (2002) **124**, 14770
49. Molina, L. M., and Hammer, B., *Phys. Rev. Lett.* (2003) **90**, 206102
50. Molina, L. M., et al., *J. Chem. Phys.* (2004) **120**, 7673
51. Molina, L. M., and Hammer, B., *Phys. Rev. B* (2004) **69**, 155424
52. Molina, L. M., and Hammer, B., *Appl. Catal. A* (2005) **291**, 21
53. Okumura, M., et al., *Catal. Lett.* (1998) **51**, 53
54. Sakurai, H., et al., *Appl. Catal. A* (2005) **291**, 179
55. Schubert, M. M., et al., *J. Catal.* (2001) **197**, 113
56. Finch, R. M., et al., *Phys. Chem. Chem. Phys.* (1999) **1**, 485
57. Hao, Z., et al., *React. Kinet. Catal. Lett.* (2000) **70**, 153
58. Bera, P., and Hegde, M. S., *Catal. Lett.* (2002) **79**, 75
59. Hodge, N. A., et al., *Catal. Today* (2002) **72**, 133
60. Kung, H. H., et al., *J. Catal.* (2003) **216**, 425
61. Carrettin, S., et al., *Angew. Chem. Int. Ed.* (2004) **43**, 2538
62. Costello, C. K., et al., *J. Phys. Chem. B* (2004) **108**, 12529
63. Fierro-Gonzalez, J. C., and Gates, B. C., *J. Phys. Chem. B* (2004) **108**, 16999
64. Guzman, J., and Gates, B. C., *J. Am. Chem. Soc.* (2004) **126**, 2672
65. Carrettin, S., et al., *Appl. Catal. A* (2005) **291**, 247
66. Fierro-Gonzalez, J. C., et al., *Catal. Lett.* (2005) **101**, 265
67. Fu, L., et al., *J. Phys. Chem. B* (2005) **109**, 3704
68. Chrétien, S., and Metiu, H., *Catal. Lett.* (2006) **107**, 143
69. Comas-Vives, A., et al., *J. Am. Chem. Soc.* (2006) **128**, 4756
70. Concepción, P., et al., *Appl. Catal. A* (2006) **307**, 42
71. González-Arellano, C., et al., *J. Catal.* (2006) **238**, 497
72. Hutchings, G. J., et al., *J. Catal.* (2006) **242**, 71
73. Grunwaldt, J.-D., et al., *J. Catal.* (1999) **186**, 458
74. Lopez, N., and Nørskov, J. K., *Surf. Sci.* (2002) **515**, 175
75. Lopez, N., and Nørskov, J. K., *J. Am. Chem. Soc.* (2002) **124**, 11262
76. Mills, G., et al., *J. Chem. Phys.* (2003) **118**, 4198
77. Shaikhutdinov, Sh. K., et al., *Catal. Lett.* (2003) **86**, 211
78. Lemire, C., et al., *Surf. Sci.* (2004) **552**, 27
79. Lemire, C., et al., *Angew. Chem. Int. Ed.* (2004) **43**, 118
80. Lopez, N., et al., *J. Catal.* (2004) **223**, 232
81. Biener, M. M., et al., *Surf. Sci.* (2005) **590**, L259
82. Deng, X., et al. *J. Am. Chem. Soc.* (2005) **127**, 9267
83. Janssens, T. V. W., et al., *J. Catal.* (2006) **240**, 108
84. Nowitzki, T., et al., *Surf. Sci.* (2006) **600**, 3595
85. Bligaard, T., et al., *J. Catal.* (2004) **224**, 206
86. Kim, J., et al., *Surf. Sci.* (2006) **600**, 4622
87. Nilsson, A., et al., *Catal. Lett.* (2005) **100**, 111
88. Lin, S. D., et al., *Catal. Lett.* (1993) **17**, 245
89. Yuan, Y., et al., *Catal. Lett.* (1996) **42**, 15
90. Haruta, M., *Catal. Today* (1997) **36**, 153
91. Lee, S.-J., and Gavriilidis, A., *J. Catal.* (2002) **206**, 305
92. Calla, J. T., et al., *J. Catal.* (2006) **238**, 458
93. Overbury, S. H., et al., *J. Catal.* (2006) **241**, 56
94. Yan, Z., et al., *Catal. Lett.* (2006) **111**, 15
95. Ruggiero, C., and Hollins, P., *J. Chem. Soc., Faraday Trans.* (1996) **92**, 4829
96. Gottfried, J. M., et al., *Surf. Sci.* (2003) **536**, 206
97. Kim, J., et al., *J. Phys. Chem. B* (2006) **110**, 17512
98. Biener, J., et al., *ChemPhysChem* (2006) **7**, 1906
99. Xu, C., et al., *J. Am. Chem. Soc.* (2007) **129**, 42
100. Carlsson, A., et al., *J. Phys. Chem. B* (2006) **110**, 5286
101. Matthey, D., et al., *Science* (2007) **315**, 1692
102. Lopez, N., et al., *J. Catal.* (2004) **225**, 86

## **Paper VI**

### **Insights into the reactivity of supported Au nanoparticles: combining theory and experiments**

**Ton V.W. Janssens, Bjerne S. Clausen, Britt Hvolbæk, Hanne Falsig, Claus H. Christensen, Thomas Bligaard, Jens K. Nørskov *Top. Catal.* 44 15 (2007)**

# Insights into the reactivity of supported Au nanoparticles: combining theory and experiments

Ton V. W. Janssens<sup>a</sup>, Bjerne S. Clausen<sup>a</sup>, Britt Hvolbæk<sup>b</sup>, Hanne Falsig<sup>c</sup>, Claus H. Christensen<sup>c</sup>, Thomas Bligaard<sup>b</sup>, and Jens K. Nørskov<sup>b,\*</sup>

<sup>a</sup>*Haldor Topsøe A/S, Nymollevej 55, DK-2800 Lyngby, Denmark*

<sup>b</sup>*Department of Physics, NanoDTU, Center for Atomic-scale Materials Physics, Technical University of Denmark, DK-2800 Lyngby, Denmark*

<sup>c</sup>*Department of Chemistry, NanoDTU, Center for Sustainable and Green Chemistry, Technical University of Denmark, DK-2800 Lyngby, Denmark*

The origin of the extraordinary catalytic activity of gold nanoparticles is discussed on the basis of density-functional calculations, adsorption studies on single crystal surfaces, and activity measurements on well characterized supported gold particles. A number of factors are identified contributing to the activity, and it is suggested that it is useful to consider low-coordinated Au atoms as the active sites, for example, CO oxidation and that the effect of the support can be viewed as structural and electronic promotion. We identify the adsorption energy of oxygen and the Au-support interface energy as important parameters determining the catalytic activity.

**KEY WORDS:** Au; nanoparticles; catalytic activity; DFT; CO-oxidation; low-coordination sites; cluster.

## 1. Introduction

Gold catalysis has received considerable attention since the discovery that nano-sized gold particles are catalytically active [1–8]. The catalytic activity of small gold particles is interesting, since low-index gold surfaces are known to be noble [9–11] and inactive towards most molecules. The fundamental question is therefore which size-related properties make the gold nanoparticles catalytically active. Catalysis by gold is technically interesting, since it opens up the possibility of developing catalysts with new and unique properties. Nanoparticles of gold can, for instance, catalyze CO oxidation at room temperature and below, which is significantly lower than the temperatures needed using more traditional supported metal catalysts. Selective and total oxidation reactions with hydrocarbons also occur at low temperature on supported gold catalysts [12–34]. This suggests that catalysis by gold nanoparticles may lead to new types of catalysts working under mild conditions—a phenomenon which is usually associated with the catalytic processes found in nature, where enzymes are able to catalyze even difficult reactions at room temperature. Understanding gold catalysis may therefore give us clues about how to mimic enzyme catalysis.

The origin of the reactivity of gold nanoparticles has been extensively debated in the literature, and a large number of proposals have been put forward. The first type of explanations associates the catalytic activity with the nature of the gold atoms in the particles. Both theory and experiments have pointed to the importance of low-

coordinated Au atoms acting as active sites [35–47]. A change in the electronic structure of gold, resulting in a metal-insulator transition has also been invoked [6,48–50]. Another type of explanation involves indirect effects of the support; charge transfer to or from the support [51–53] or support-induced strain [36]. A third type of explanation involves the support directly. This includes transfer of activated oxygen from the support (i.e., reducible or irreducible support), or special active sites at the metal/oxide boundary [8,54–64]. Finally, there are a number of reports of catalysts consisting of single or a few Au<sup>+</sup> ions in the support [27,65–81]. We note that combinations of the above effects can come into play; the gold-support interaction may for instance determine the morphology of the gold particles and thus influence the number of low-coordinated atoms or the strain. Therefore, it is not surprising that the activity of gold catalysts is often found to be influenced by the method of preparation and activation of the catalyst [82–85].

In the following we will develop a model for catalysis by gold that can be used to understand a number of the effects that have been observed. From the outset we will distinguish between the catalytic effects originating from metallic gold particles and those associated with Au<sup>+</sup> dissolved in the support. Both types of Au catalysis exist for different systems. We concentrate solely on the particle size effects of metallic gold. We will show that several of the explanations mentioned above contribute to the activity of gold particles, and that they can be ordered in a hierarchy according to their importance. We propose that it is useful to first consider the effect of low coordinated Au atoms acting as active sites. The support also has an effect on the activity, and may

\* To whom correspondence should be addressed.  
E-mail: nørskov@fysik.dtu.dk

therefore be viewed as a promoter, which both affects the surface chemistry directly and acts as a structural promoter determining the particle size and shape, and hence, the number of low coordinated gold atoms.

## 2. The reactivity of gold

Most molecules adsorb only weakly on gold surfaces at room temperature, and dissociative chemisorption of simple molecules such as  $O_2$  is thermodynamically prohibited. To exemplify this, figure 1 shows the calculated dissociative chemisorption energy of oxygen on a number of stepped metal surfaces relative to a free oxygen molecule [86]. Of all the metals considered, Au has the weakest bond to atomic oxygen, and is the only metal where the  $O_2$  dissociation is endothermic on the stepped (211) surface. This is in excellent agreement with the experimental observation that molecular oxygen does not produce oxygen adatoms even on a stepped Au(211) surface at 700 Torr at 300–450 K [87].

There are two effects that cause the weak bonding of oxygen on Au. The first effect is related to the energy of the orbitals involved in the oxygen–metal bond formation, viz., the metal-d band and the 2p valence level of oxygen. The bond strength is predominantly determined by the filling of the metal-d/2p antibonding orbitals. If the d-band energy is close to the Fermi energy, which is the case for example, Fe and Ru, the antibonding states lie well above the Fermi-level and are therefore mostly empty. This results in a strong oxygen-metal bonding [11,88]. For the elements further to the right in the periodic table, the d-bands are lower in energy, and the metal-d/2p antibonding orbitals move down in energy towards the Fermi level, causing a higher occupation of the antibonding levels. The result is a weaker oxygen binding. For Cu, Ag, and Au, the d-band has moved to such a low energy, that the metal-d/2p antibonding states are essentially filled, and hence these metals have the lowest binding energy for oxygen in each transition metal row. The other effect is the Pauli repulsion between the O valence states and the metal d states; for the noble metals this effect dominates. Since the 5d

Cr	Mn	Fe	Co	Ni	Cu
		-6.30	-5.07	-3.90	-2.51
Mo	Tc	Ru	Rh	Pd	Ag
-7.48		-4.62	-4.03	-1.20	-0.65
W	Re	Os	Ir	Pt	Au
-8.62			-4.65	-2.17	+0.54

Figure 1. Calculated dissociative chemisorption energies for oxygen on transition metal surfaces with respect to the molecule in vacuum. All results are for adsorption at stepped bcc(210) (Fe, Mo, W) and fcc(211) (other metals) surfaces [86].

states are more extended than the 4d states and the 3d states, the Pauli repulsion is largest here and there is a weakening of the bond when going down in the periodic table from Cu to Au. Both bond-weakening effects are most pronounced in the case of Au, which explains the unique nobleness of Au towards oxygen [11,36].

In spite of the inert character of Au, supported gold catalysts have been shown to be active for several reactions. The most studied reaction is CO oxidation. For this reaction, the general trend is that supported gold catalysts, which exhibit significant catalytic activity, always contain gold particles with a diameter less than approximately 5–6 nm, as Haruta et al. pointed out already in an early publication [5]. This is illustrated in figure 2, showing a compilation of literature data from the past 10 years for CO oxidation activities at 273 K as a function of the Au particle diameter for different Au catalysts [13,22,43,47,54,55,89–94]. The strong dependence of the activity on the Au particle size is obvious. If we look at only the data with a  $TiO_2$  substrate it is seen that the activity of e.g., 2 nm and 20 nm clusters differs by a factor of more than 100. The differences between particles of the same size for different supports are at least an order of magnitude smaller; typically they differ by a factor of 2–3 [43]. We also note that the results do not depend strongly on whether the support is reducible or not. This is clear experimental evidence that the gold particle size is an important parameter for the catalytic activity of supported catalysts. In order to gain some insight into the reason for this particle size effect, we

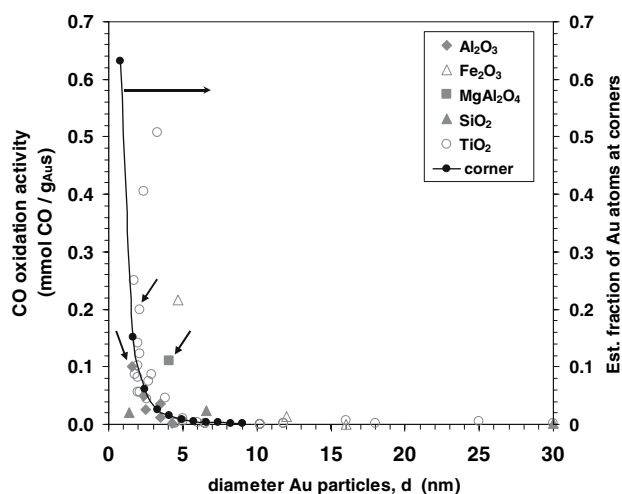


Figure 2. Reported catalytic activities (in  $\text{mmol}/g_{Au} \text{ s}$ , left axis) for CO oxidation at 273 K over different Au-based catalysts as a function of the Au particle size ( $d$ , in nm) [13,22,43,47,54,55,89–94]. The different supports are indicated by the symbol shape, open symbols correspond to reducible supports, closed symbols to irreducible supports. The solid curve shows the calculated fraction of atoms (right axis) located at the corners of the nanoparticles as a function of particle diameter for uniform particles shaped as the top half of a regular cuboctahedron (see also Figure 8). The arrows point to the measured activities in ref. [47]. Updated from ref. [43].



turn to some simple density functional theory calculations designed to elucidate the origin of the catalytic activity of small gold particles.

### 3. Catalytic activity of Au clusters: a simple DFT model

To investigate the reactivity of the gold clusters by DFT calculations, the CO oxidation reaction is used as a test reaction. We consider a gold nanoparticle with 10 atoms, first as a free particle without support, and later with a support included. The calculations serve to show how small particles can be catalytically active, and by comparing the results to those for extended surfaces, we can understand in more general terms what characterizes the active sites of the Au nanoparticles. The 10 atom cluster used here has a diameter of  $\sim 0.7$  nm, which is at the low end of the clusters studied experimentally. It is mainly chosen to illustrate the effects, and not as a realistic model of the active catalysts.

Figure 3 [37] shows the calculated energy diagram for the two possible reaction mechanisms for CO oxidation; one where the  $O_2$  is dissociated prior to reaction with CO and one where molecular  $O_2$  reacts directly with CO on the surface. The calculation is made on an  $Au_{10}$  cluster identical to the one in ref. [37] to illustrate an Au cluster bound to a support. The bottom layers are restricted not to move perpendicular to the layers to mimic the adhesion to the substrate. This is an extremely simple model and a slightly more realistic one will be

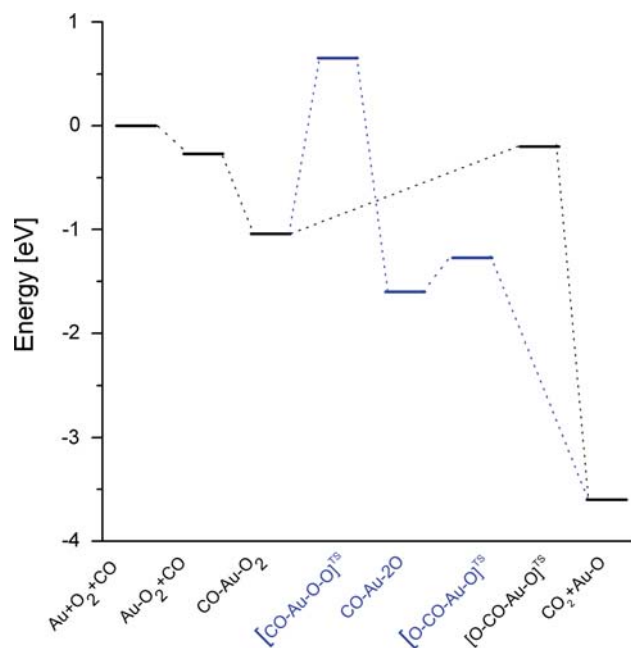


Figure 3. Calculated reaction energies for CO oxidation on an  $Au_{10}$  cluster (shown in inset). The bottom of the cluster is kept fixed in the direction perpendicular to the support. Both a path involving dissociation of  $O_2$  and one where molecular  $O_2$  reacts directly with CO are shown.

discussed later. We find in agreement with ref. [37] that both  $O_2$  and CO adsorb readily on the  $Au_{10}$  cluster. The reaction of adsorbed  $O_2$  and CO to form  $CO_2$  and the subsequent reaction of adsorbed O with another CO molecule have low barriers [37]. The alternative process where  $O_2$  dissociates directly we find to have a sizable barrier—more than 1 eV in agreement with [56]. This result is different from that in ref. [37], and we suggest that the barrier reported in ref. [37] is flawed by having too few images included in the Nudged Elastic Band calculation of the reaction path.

These results clearly indicate that CO oxidation should be possible at room temperature at the surface of a  $Au_{10}$  cluster. Both  $O_2$ , O, and CO bind to the surface in sharp contrast to the endothermic adsorption energy on the Au(211) surface, see e.g., figure 1. This is the first clue why the surface of a nano-sized Au cluster is chemically very different from close-packed or stepped surfaces.

Next, figure 4 shows the results of the calculations for the  $O_2$  mechanism for a  $Au_{10}$  cluster that is anchored to a rutile  $TiO_2(110)$  support. The titania surface to which the Au cluster binds has three oxygen vacancies [95,96]. This model is chosen on the basis of detailed STM experiments and calculations, which show that Au clusters bind to  $TiO_2(110)$  through oxygen vacancies, and that about one vacancy per three Au atoms is required to make the cluster stable [95,97]. In this case the Au/ $TiO_2$  cluster has been allowed to relax freely, and the structure it assumes is quite different from the model used in figure 3.

Two different reaction paths are investigated in figure 4: one path in which the reaction only takes place on the Au cluster (shown in path1), and another path where the substrate takes part in the reaction (shown in path2). The energy barriers along the two paths are shown in

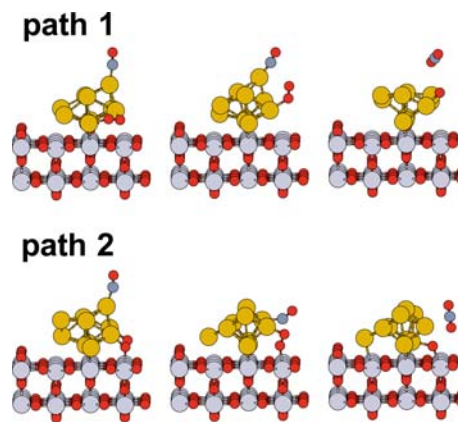


Figure 4. Relaxed geometries of the initial, transition, and final states for CO oxidation on a  $Au_{10}$  cluster supported on a  $TiO_2(110)$  surface. Path 1: CO oxidation takes place on the Au particle, without direct influence of the support. Path 2: CO oxidation takes place at the Au– $TiO_2$  interface, and involves direct interaction with the support. From ref. [96].

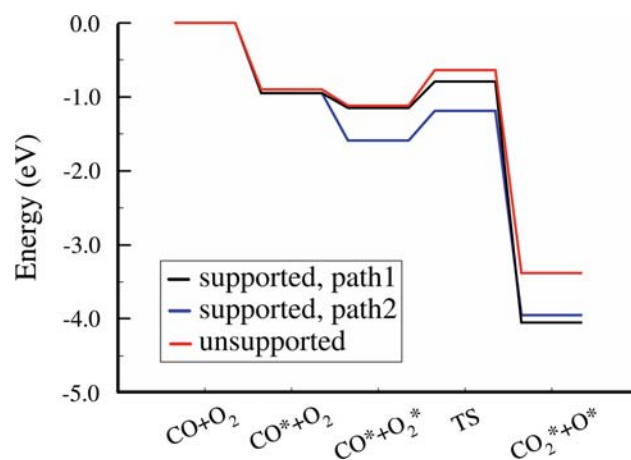


Figure 5. Energy profiles for CO oxidation on a  $\text{Au}_{10}$  cluster. Blue line:  $\text{Au}_{10}$  supported on  $\text{TiO}_2(110)$ , CO oxidation takes place at the Au/ $\text{TiO}_2$  interface (path a); black line:  $\text{Au}_{10}$  supported on  $\text{TiO}_2(110)$ , CO oxidation takes place solely on the Au particle (path b); red line: unsupported cluster with the bottom three atoms kept fixed at the positions as they would be if the oxide were present.

figure 5, where they are compared to the energy barriers of the reaction on an unsupported  $\text{Au}_{10}$  cluster of the same structure [95,96]. The results in figure 5 show that the effect of the support on the activation barriers is quite small. Adding the support, however, results in stronger bonding of  $\text{O}_2$ , as shown by Hammer et al. and Hu et al. [57–59,98]. It should be noted that the results of Hammer et al. and Hu et al. [57–59,98] also involve low coordinated atoms, but due to constraints of the models used in their studies, only edges are involved. The very low barriers in figure 5 clearly involve corner atoms with even lower coordination numbers. We note that the activation barrier found in figure 5 for CO oxidation (ca. 0.5 eV) is consistent with the range (0.1–0.4 eV) measured experimentally [5,22,54,55,89,90,93,99].

#### 4. The importance of the Au coordination number

The simple model calculations described above point to corner atoms of the  $\text{Au}_{10}$  cluster as the active sites for  $\text{O}_2$  and CO bonding and for the CO oxidation process. In this section we will show that this can be viewed as a general effect of low-coordinated metal atoms, and in the next section we will show that this can explain semi-quantitatively the experimentally observed variation of catalytic activity with particle size.

Figure 6 shows that there is a clear relation between the adsorption energy of CO and oxygen and the coordination number of the Au atoms to which these molecules are attached: The lower the coordination number, the stronger the bond. The plot includes calculated values for the  $\text{Au}_{10}$  cluster and for different extended surfaces. This dependence points to the coordination number of the Au atoms as an important

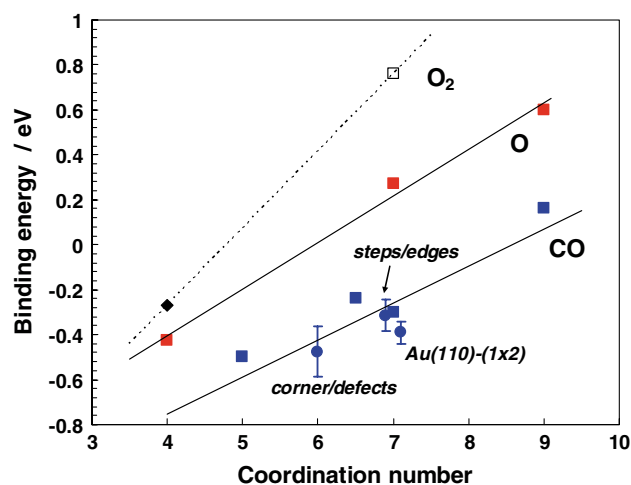


Figure 6. The correlation between the binding energies for CO,  $\text{O}_2$  and O atoms on Au and the coordination number of the Au atoms in a series of environments. The binding energies (eV) are referred to gas-phase CO and  $\text{O}_2$ , the values for atomic oxygen adsorption are given per O atom (half the value of figure 1). Since  $\text{O}_2$  adsorbs on Au(211) in a metastable state this value is only tentative. The solid blue dots indicate experimentally determined values for the CO adsorption energy on steps, edges, and the Au(110)-(1 $\times$ 2) surface. These values are determined from CO TPD on the Au(211), Au(332), and Au(110)-(1 $\times$ 2) single crystal surfaces and from Au nanoparticles supported on flat  $\text{Al}_2\text{O}_3$  or FeO [39,102–104] assuming a pre-exponential factor of  $10^{13}$ . The error bars indicate the energy range obtained with a pre-exponential factor between  $10^{11}$  and  $10^{15}$  (see figure 7).

parameter. The figure only includes adsorption energies, but the same trend is often observed for the transition state energies [100].

It is important to note the magnitude of the coordination number effects. For the O–Au and  $\text{O}_2$ –Au bond the variation in bond energy from high to low coordinated atoms is of the order of 1 eV and for CO the effect is only a little smaller. This is a significantly larger effect than e.g., the effect of the interaction with the support as seen in figure 5.

The coordination number effect on the adsorption energies can be related to changes in the surface electronic structure [42]. The low coordinated Au atoms have high lying metal d states, which are in a better position to interact with the adsorbate valence state than the low lying states of the high coordination number states of the close packed surface. We note that this is an effect that is not restricted to Au catalysis. Low coordinated transition metal atoms on surfaces are generally found to have higher lying d states and to be more reactive than highly coordinated metal atoms [11,101].

The trend that the CO adsorption strength on Au surfaces increases with decreasing coordination number is also reflected in temperature-programmed desorption of CO (CO-TPD) on Au single crystal surfaces and well-defined nanoparticles. Figure 7 shows an overview of TPD traces of CO adsorbed on the Au(211) [102] and Au(332) [103] surfaces, a sputtered and annealed

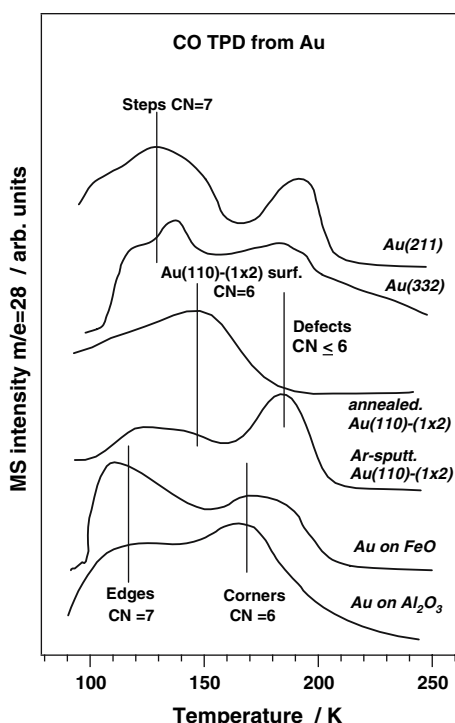


Figure 7. Temperature programmed desorption of CO on Au(211) [102], Au(332) [103], sputtered and annealed Au(110)-(1×2) [104], and Au nanoparticles on a flat Al<sub>2</sub>O<sub>3</sub> and FeO surface [39]. Each trace has an arbitrary scaling, and does not reflect the absolute amounts of CO in the different systems, only relative intensities within a single curve can be used.

Au(110)-(1×2) surface [104], and Au nanoparticles on Au/FeO and Au/Al<sub>2</sub>O<sub>3</sub> [39]. A consistent interpretation of these results is that the desorption around 170–190 K corresponds to CO adsorbed on defect sites or corner sites, the desorption around 150 K corresponds to CO adsorption on the Au(110)-(1×2) surface, and the desorption around 110–130 K is due to CO adsorbed on edges of the nanoparticles, or step sites on the single crystal surfaces. The assignment of the feature around 170–200 K to defect sites is confirmed by the fact that it disappears upon annealing the sputtered Au(110)-(1×2) surface. An assignment of the two desorption peaks in CO-TPD from the Au(211) and Au(332) surfaces to desorption from step sites (~190 K) and terraces (~130 K) seems unlikely, since the relative intensities of the two signals is about the same for both surfaces, despite the fact that the Au(332) surface contains about twice as much terrace sites compared the Au(211) surface. The higher edge/corner ratio on the Au/FeO system reflects the larger particle size on Au/FeO (5.0 nm) compared to the Au/Al<sub>2</sub>O<sub>3</sub> system (2.5 nm), as determined by STM [39]. The estimated CO adsorption energies, derived from the observed desorption temperature ranges, using the rate equation for first order desorption and assuming a pre-exponential factor between 10<sup>11</sup> and 10<sup>15</sup> s<sup>-1</sup>, are 0.24–0.39 eV for the edge/step sites (CN = 7), 0.34–0.45 eV for the Au

(110)-(1×2) surface—in excellent agreement with the energy range reported by Meier et al. [105]—and 0.38–0.58 eV for the Au corner and defect sites (CN≤6). These values are also indicated in figure 6, and lends support to the calculated trends in interaction energies.

There is additional experimental evidence that supports the notion that low-coordinated Au atoms on metal surfaces are chemically active. Infrared studies of adsorbed CO on Au particles indicate that adsorption of CO is not sensitive for particle size or thickness, except for very thin particles, which is an expected behavior if the Au–Au coordination number controls the adsorption [42]. Oxygen-sputtering of Au(111) results in an enhanced SO<sub>2</sub> uptake [45]. Finally, atomic oxygen deposited by exposure to an oxygen plasma jet or by electron-induced dissociation of NO<sub>2</sub> on a Au(111) surface causes a surface roughening, and the sticking and dissociation probability of O<sub>2</sub> increases by more than 1000 times [46,106,107].

## 5. Low coordinated Au atoms in supported Au catalysts

In supported Au particles, the atoms in the surface of the (111) and (100) crystal faces, at the edges, at the corners, and the atoms at the contact perimeter between the support and Au particle are in principle accessible for CO and oxygen, and are therefore possible active sites. The results of the DFT calculations indicate that the low coordinated Au atoms are important for the activity of Au nanoparticles. Obviously, the abundance of these sites in a supported catalyst depends on the diameter and the shape of the Au particles. In the following we show how the relative number of low coordinated atoms varies with particle size, first using simple models and subsequently by explicitly counting the number of low coordinated atoms for well characterized supported Au catalysts.

Figure 8 shows the fraction of the Au atoms that are present in the crystal faces, at the edges, and at the corners of the Au particles for particle diameters between 1 nm and 9 nm for Au particles shaped as the top half of a truncated octahedron. The details are given in the supporting material of ref. [108]. From this figure, it is seen that in the size range 2–5 nm the number of surface atoms is almost constant, while the number of edge and corner atoms increases substantially. The calculated number of corner atoms is shown as the solid line in figure 2, and it is clearly seen that the increase in the number of corner atoms correlates very well with the increase of the measured CO oxidation activity of Au catalysts with decreasing Au particle size observed for supported catalysts in general. This implies that the observed general trend for the catalytic activity of supported Au catalysts can be explained by the expected amounts of Au corner atoms at the different Au particle sizes.

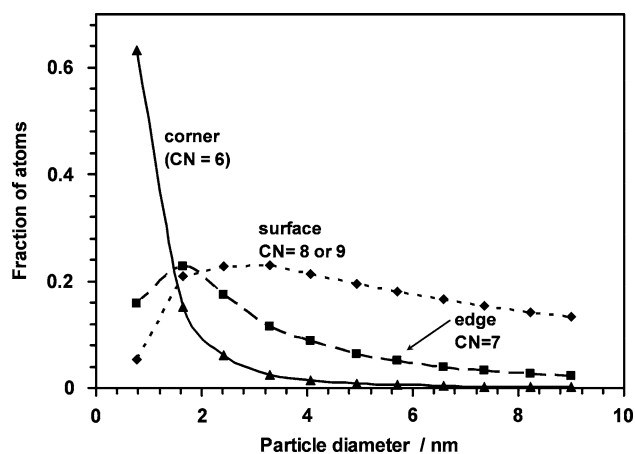


Figure 8. Calculated fractions of Au atoms at corners, edges, and crystal faces in uniform nanoparticles consisting of the top half of a truncated octahedron as a function of the Au particle diameter.

This conclusion is in excellent agreement with the results obtained from DFT calculations, which show that adsorption of CO or oxygen does not occur on Au atoms with a coordination number larger than 7. This means that adsorption of CO or oxygen on the (111) and (100) planes of Au, represented in figure 2 as surface atoms (CN = 8 or 9) does not occur. For Au atoms with a lower coordination number, i.e., edges (CN = 7), or corners (CN = 5 or 6) adsorption of CO and oxygen becomes feasible, and therefore these sites can be catalytically active. The fact that the variation in the CO oxidation activity with size corresponds with the estimated number of corner atoms, is an indication that the contribution of the corner atoms dominates.

From a geometric consideration, it can be derived that the dependence of the catalytic activity on the particle diameter is determined by the dimensionality of the active site. For particles with a given shape, the number of corner atoms per gold particle is independent of the particle diameter,  $d$ . This means that the catalytic activity becomes proportional to the number of Au particles in the supported catalyst. For a given amount of Au, the number of particles is proportional to  $1/d^3$ , and consequently, the catalytic activity (expressed per gram or mol Au) is expected to be proportional to  $1/d^3$ , if the reaction occurs at the Au corner atoms. Similarly, the activity becomes proportional to  $1/d^2$  if the reaction occurs on the edges or contact perimeter of the Au particles, and proportional to  $1/d$  if the reaction occurs on the (111) and (100) crystal faces. The general expression is a power law in the form of  $r \propto d^{(n-3)}$ , where  $n$  is the dimension of the active site: 0 for points (corners), 1 for edge or perimeter, and 2 for the crystal faces.

By evaluation of  $n$ , the dimensionality of the (dominating) active site is obtained, and thus it can be determined whether the reaction takes place at the corners, edges or perimeters, or crystal faces of the Au particles. Overbury et al. applied this approach in a recent study

of Au/TiO<sub>2</sub> catalysts (4.5 and 7.2 wt%), using EXAFS combined with CO oxidation activity measurements [94]. In these experiments, the particle size was varied by applying different annealing procedures. The particle size was then derived from the Au–Au coordination number determined by EXAFS. These results are represented in figure 9, showing the logarithm of the measured activities as a function of the logarithm of the Au particle size. From the slope of these graphs, it is found that the rate varies with  $d^{-2}$  to  $d^{-2.4}$  for the catalyst with a 4.5 wt% Au loading, and  $d^{-2.9}$  to  $d^{-3.0}$  for the catalyst with a 7.2 wt% loading. The corresponding dimensionality of the active sites in the 4.5 wt% Au/TiO<sub>2</sub> catalyst is 0.6–1, which would correspond to a contribution of both corners and edges. The dimensionality in the 7.2wt% Au/TiO<sub>2</sub> catalyst is 0, which points to corner atoms as the active sites. These experimental results obtained from supported Au catalysts are in good agreement with the conclusion that low-coordinated Au atoms are required for catalytic activity [43].

The power law relation between catalytic activity and Au particle diameter presented above is quite easy to apply, but it represents a simple model that cannot account for particle size distributions and differences in

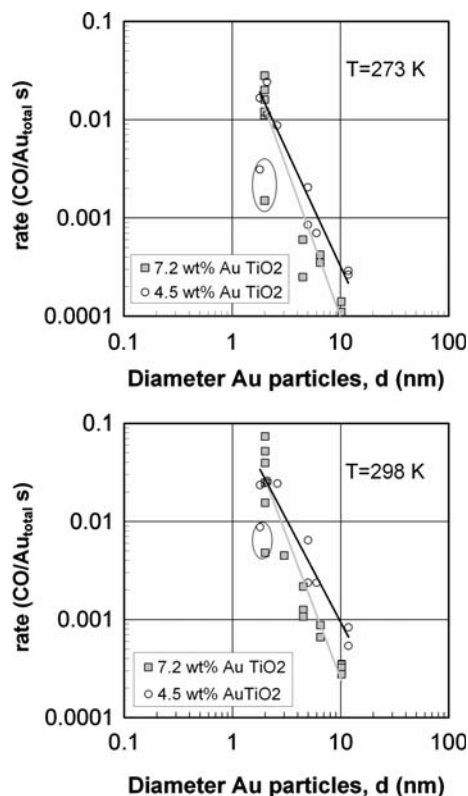


Figure 9. Activity at 298 K (bottom) and at 273 K (top) as a function of the Au particle diameter for two series of Au/TiO<sub>2</sub> catalysts, containing 4.5 and 7.2 wt% Au., respectively. The particle size has been varied by heat treatment at various temperatures between 423 and 773 K. The rate is expressed per total amount of Au. Best power law fits to the data (excluding the two encircled points) are shown for each catalyst. Reproduced from ref. [94].

particle shape. Recently, a more advanced model was developed, that is capable of handling particle size distributions and variations in Au particle shape. In this model, which is based on measurements of the sizes and volumes of the individual Au particles by High Angle Annular Dark Field-Scanning Transmission Electron Microscopy (HAADF-STEM) [108], the Au particle geometry in a supported gold catalyst is described as the top slice of a truncated octahedron, a geometry that is consistent with an fcc crystal structure [109]. The number of atoms at the edges of the truncated octahedron ( $m$ ) and the particle thickness ( $l$ ) can be varied independently of each other, and the complete geometric model of the supported Au particles then consists of a two-dimensional distribution function with  $m$  and  $l$  as parameters. An example of such a distribution is given in figure 10, which shows the distribution of Au particle size and shape in a supported Au/TiO<sub>2</sub> catalyst [108]. The local environment of each Au atom is known in these geometric models, and the number of Au atoms in specific locations, e.g., corners, edges, contact perimeter, crystal faces, is readily estimated. Using this method to count atoms in different configurations, it is possible to relate the knowledge on the atomic scale obtained from surface science studies and DFT calculations to the measured activity of supported Au catalysts.

By combining the analysis of the Au particle geometry with activity measurements, the turn-over frequency

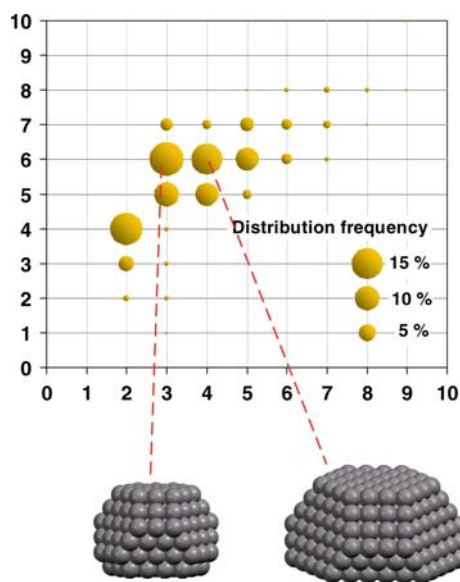


Figure 10. Example of a two-dimensional particle geometry distribution for a Au/TiO<sub>2</sub> catalyst containing 4.4 wt% Au after heating to 400 °C for 1 h and approximately 15 h on stream at 273 K in an atmosphere of 1% CO/21% O<sub>2</sub> in Ar. The particle geometry is determined from a HAADF-STEM characterization of the catalyst after reaction. The area of the circles indicates the fraction of the Au particles with the indicated edge length (horizontal axis) and number of layers (vertical axis). The two most abundant geometries are drawn as examples of the general Au particle geometry in the geometric model. Data from ref. [108].

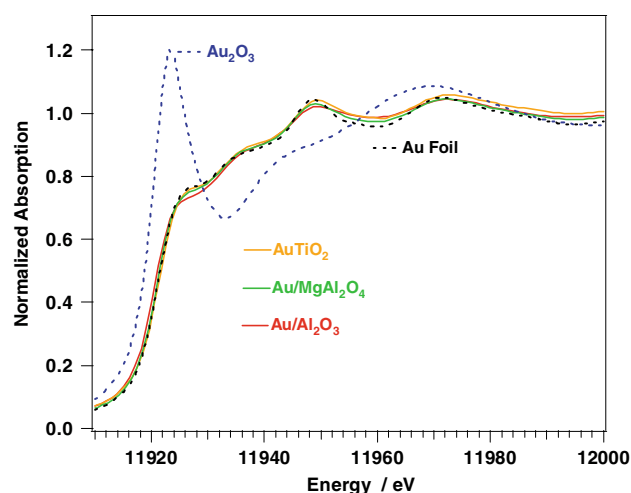


Figure 11. Au-L<sub>3</sub> XANES edge for a 4.4 wt% Au/TiO<sub>2</sub>, 4.1 wt% Au/MgAl<sub>2</sub>O<sub>4</sub>, and a 4.0 wt% Au/Al<sub>2</sub>O<sub>3</sub> catalyst during reaction at room temperature in 1% CO/21% O<sub>2</sub> in Ar, after 1 h heating at 400 °C in the same gas mixture. The XANES edges for Au<sub>2</sub>O<sub>3</sub> and Au foil (dashed lines) are given as a reference. The data indicate that all the Au in the catalysts is in the metallic state.

at specific sites, e.g., corners, can be calculated. This has been done for a supported Au/TiO<sub>2</sub>, Au/MgAl<sub>2</sub>O<sub>4</sub> and a Au/Al<sub>2</sub>O<sub>3</sub> catalyst, all containing approximately 4 wt% Au [47]. The activity of these three catalysts was measured at 273 K and 1 atm, using a feed of 1% CO and 21% O<sub>2</sub> in Ar, after annealing the freshly prepared catalysts for 1 h at 400 °C in the same gas mixture. Figure 11 shows the Au-L<sub>3</sub> X-ray absorption edges (XANES) for these catalysts after this heat treatment, together with the corresponding edges for Au<sub>2</sub>O<sub>3</sub> and Au-foil as a reference. This clearly shows that all Au in these supported catalysts is present as metallic Au, and the catalytic activity of these catalysts must therefore be ascribed to metallic Au.

Figure 12 shows the measured activities of these catalysts as a function of the time on stream;  $t = 0$  is defined as the time at which the reactor temperature reached 273 K after the heat treatment [47]. The Au/MgAl<sub>2</sub>O<sub>4</sub> and Au/Al<sub>2</sub>O<sub>3</sub> catalysts reach the steady state rather quickly, while the Au/TiO<sub>2</sub> shows a slower deactivation. After 10–15 h on stream, all catalysts reached a rather constant activity. The activities of the Au/TiO<sub>2</sub>, Au/MgAl<sub>2</sub>O<sub>4</sub> and Au/Al<sub>2</sub>O<sub>3</sub> catalysts in this study are 8.8 mmol/g<sub>cat</sub> s, 4.8 mmol/g<sub>cat</sub> s, and 4.2 mmol/g<sub>cat</sub> s, respectively [47]. These final activities are indicated by the arrows in figure 2, and it can be seen that the values are consistent with the general trend for the CO oxidation activity for Au catalysts. By combining the activity data and the geometric models for these catalysts, the turn over frequency per Au corner atom becomes 0.8 s<sup>-1</sup> for both the Au/TiO<sub>2</sub> and the Au/MgAl<sub>2</sub>O<sub>4</sub> catalysts, and 0.2 s<sup>-1</sup> for the Au/Al<sub>2</sub>O<sub>3</sub> catalyst. This result shows that the different activity of the

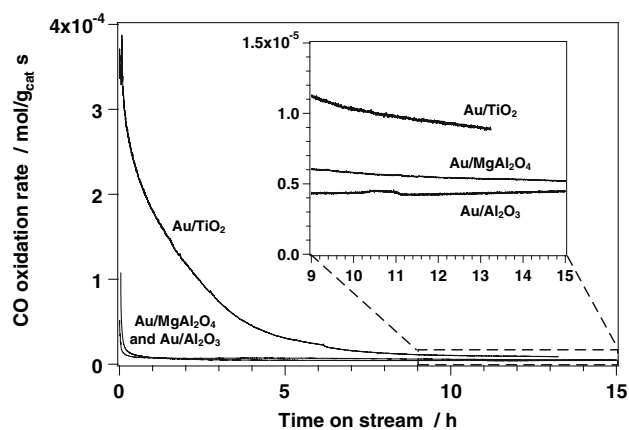


Figure 12. CO oxidation activity of a 4.4 wt% Au/TiO<sub>2</sub>, 4.1 wt% Au/MgAl<sub>2</sub>O<sub>4</sub>, and a 4.0 wt% Au/Al<sub>2</sub>O<sub>3</sub> catalyst during reaction at 273 K in 1% CO/21% O<sub>2</sub> in Ar during the first 10–15 h of operation. The inset shows an enlargement of the final part, indicating that the Au/TiO<sub>2</sub> catalyst is about twice as active as the Au/MgAl<sub>2</sub>O<sub>4</sub>, and Au/Al<sub>2</sub>O<sub>3</sub> catalysts. From ref. [47].

Au/TiO<sub>2</sub> and the Au/MgAl<sub>2</sub>O<sub>4</sub> catalysts can be entirely explained by the different amount of corner-Au atoms in these catalysts, despite the fact that TiO<sub>2</sub> is a reducible support and the MgAl<sub>2</sub>O<sub>4</sub> support is not. The turn over frequency for Au/Al<sub>2</sub>O<sub>3</sub> is approximately 4 times lower. We note that the Au particles on Al<sub>2</sub>O<sub>3</sub> have a very different shape, being much flatter and this may result in a different support effect in this case. This is unresolved at the present.

It is important to note that by ascribing the dependence of the catalytic activity on the Au particle size to a higher density of active sites (corner atoms), the turn-over frequency (per corner atom) does *not* depend on the particle size; it is the same in both small and large particles. This is fundamentally different from the quantum-size effect [6,7,22,48], which ascribes the activity of small Au particles to a particle-size dependent turn over frequency, arising from changes in electronic structure as the particle size decreases. Though quantum-size effects are definitely important for very small particles, containing only a few atoms [110–112], they seem not to be necessary to explain the catalytic effect for supported Au particles on Au/TiO<sub>2</sub> and Au/MgAl<sub>2</sub>O<sub>4</sub> larger than about 1.5 nm.

A consequence of the requirement for low-coordinated Au atoms is that large particles can be catalytically active as well, with essentially the same turn over frequency per active site as small particles. To obtain a measurable activity, a sufficient amount of Au atoms with a low coordination number must be available. This is often not the case in supported catalysts containing a few large particles and no small particles (see figure 8). By applying surface sensitive techniques on single crystal surfaces or flat model systems, it has been shown that continuous Au surfaces are capable of adsorbing CO or

atomic oxygen, and can be active catalysts for CO oxidation provided that low coordinated Au atoms are present on the surface. Adsorption of CO takes place on the stepped Au(211), Au(322), and the Au(110)-(1×2) reconstructed Au single crystal surfaces [102–104,113], or a Au tip in field emission microscopy [114], while the Au(111) or Au(100) surfaces are inert. Likewise, CO oxidation has been shown on the Au(110)-(1×2) surface or an unannealed continuous film of Au on TiO<sub>2</sub> [115,116]. In conclusion, the Au–Au coordination number is the critical parameter to obtain catalytically active Au particles, rather than the particle size itself. In supported high-surface area catalysts, however, small particles are generally required to obtain a large amount of low-coordinated Au atoms.

## 6. Influence of the support

Many of the factors that influence the performance of supported Au catalysts are in some way connected to the support. The result that the turn over frequencies for the Au/TiO<sub>2</sub> and Au/MgAl<sub>2</sub>O<sub>4</sub> supported catalysts are the same (per corner atom) indicates that the support does not affect the turn over frequency in these cases, or that the two different supports affect the turn over frequency in the same way. The two supported catalysts do not have the same overall activity, so there is a clear indirect influence of the support in these catalysts: The support determines the size and shape of the Au particles, and consequently the amount of low-coordinated Au atoms. This type of indirect support effect has been proposed earlier [44,97,117,118] and implies that the Au/support interface energy is an important parameter that determines the final shape and size of the Au particles [119,120]. The interaction between the Au particles and the Al<sub>2</sub>O<sub>3</sub> support is significantly stronger compared to the TiO<sub>2</sub> and MgAl<sub>2</sub>O<sub>4</sub>-supports [108], and it can be speculated if this is related to the observed lower turn over frequency per corner atom for Au/Al<sub>2</sub>O<sub>3</sub> [47,108]. For Au/TiO<sub>2</sub>, it has been shown that Au exclusively binds on the oxygen vacancies in the TiO<sub>2</sub> surface, and that the interface energy depends on the number of oxygen vacancies under the Au particle [97]. As a consequence, for the Au/TiO<sub>2</sub> catalysts, the final shape of the Au particles depends on the defect density in the support.

Another support effect that has been discussed intensively is support-mediated oxygen transport. In this model, oxygen is released from the oxidic support, which diffuses over the support surface to the edges of the Au particles, where the CO oxidation reaction takes place. According to this model, application of reducible oxides results in more active catalysts. However, the similar turn over frequency found for the Au/TiO<sub>2</sub> and Au/MgAl<sub>2</sub>O<sub>4</sub> catalysts implies that such a support

mediated oxygen transport does not take place on the Au/TiO<sub>2</sub> catalyst: Since the MgAl<sub>2</sub>O<sub>4</sub> support is not reducible, support mediated oxygen transport is not possible, and the similar turn over frequency for the Au/TiO<sub>2</sub> and Au/MgAl<sub>2</sub>O<sub>4</sub> supports indicate that the influence of the support on the turn over frequency is the same for these catalysts. Likewise, the lower turn over frequency for the Au/Al<sub>2</sub>O<sub>3</sub> catalyst is not the consequence of lack of surface mediated oxygen transport, since both the MgAl<sub>2</sub>O<sub>4</sub> and Al<sub>2</sub>O<sub>3</sub> supports are irreducible. Therefore, support mediated oxygen transport does not seem to play an important role in the Au/TiO<sub>2</sub>, Au/MgAl<sub>2</sub>O<sub>4</sub> and Au/Al<sub>2</sub>O<sub>3</sub> catalysts.

The absence of surface mediated oxygen transport in Au catalyzed CO oxidation is corroborated by isotope labeling studies of the CO oxidation reaction on Au/TiO<sub>2</sub> and Au/Al<sub>2</sub>O<sub>3</sub>, which show that the CO<sub>2</sub> does not contain oxygen originating from the support [121]. Furthermore, the activities of a Au/TiO<sub>2</sub>, Au/Al<sub>2</sub>O<sub>3</sub>, Au/ZnO, and Au/ZrO<sub>2</sub>, catalysts do not follow the trend expected from the reducibility of the support [35,118,122]. A recent report of an active and stable LaPO<sub>4</sub><sup>-</sup> supported Au catalyst proves that non-oxidic supports can also be used [123], which further supports the idea that support-mediated oxygen transport does not necessarily contribute to the CO oxidation activity of Au catalysts.

Even if the support does not supply the oxygen for the CO oxidation reaction, it may still play a role in the binding of oxygen on the supported Au catalyst as discussed above. The energy diagram shown in figure 5 for instance shows that in the support-mediated reaction path, the oxygen binding is stronger [95,96], while the activation energy for CO oxidation is about the same as for the metal-only reaction pathway. The stronger binding of the oxygen may have a positive effect on the catalytic activity, as first proposed by Molina and Hammer [57,58,61]. The extra bonding at the gold-oxide interface can be viewed as a promotion of the oxygen adsorption much like the promotion of N<sub>2</sub> adsorption by alkali metals in ammonia synthesis catalysts [124–127]. Similar effects can be obtained by addition of other promoting metal oxides [19,20,31,128,129].

## 7. Conclusions

The general trend that the activity of supported Au catalysts increases with decreasing Au particle size can be related to the number of low coordinated Au atoms present in the Au particles. Density functional (DFT) calculations of adsorption of CO and oxygen on Au show that adsorption on the densely packed surfaces is generally difficult or thermodynamically not possible, while adsorption becomes feasible on Au atoms with a lower coordination number. The effect of the Au coordination number on the adsorption strength of CO and

oxygen is larger than other electronic effects, or strain, and is therefore a crucial parameter for the catalytic activity of Au.

The adsorption energies estimated from temperature programmed desorption of CO on Au(332), Au(211), Au(110)-(1×2) surfaces, and Au nanoparticles are consistent with the expected values from Au coordination number in these systems, thus supporting the calculated relation between coordination number and adsorption energy.

In supported Au catalysts, the most reactive low-coordinated Au atoms are the ones located on the corners of the Au particles. The estimated amount of corner atoms from a simple particle model consisting of uniform particles with a truncated-octahedral geometry follows closely the observed general trend of increasing CO oxidation activity with decreasing particle size. This is the first indication that the activity of Au particles is largely determined by the number of low coordinated Au atoms. More detailed studies of the relation between Au particle structure and catalytic activity for supported Au/TiO<sub>2</sub>, Au/MgAl<sub>2</sub>O<sub>4</sub>, also point to a proportional relationship between the activity and amount of corner atoms in these catalysts.

The activity of Au/Al<sub>2</sub>O<sub>3</sub> is lower than expected. A possible explanation is that the support effect in Au/Al<sub>2</sub>O<sub>3</sub> is different compared to the TiO<sub>2</sub> and MgAl<sub>2</sub>O<sub>4</sub> supports. The nature of this different support effect is unknown at the moment. A direct oxygen supply from the support, however, can be ruled out for Au/TiO<sub>2</sub>, Au/MgAl<sub>2</sub>O<sub>4</sub>, and Au/Al<sub>2</sub>O<sub>3</sub> catalysts. Since adsorption and activation of oxygen on metallic Au is difficult, it seems likely that these support effects are related to binding of oxygen on the catalyst.

The interface energy between Au and the different supports plays a crucial role in determining the structural and chemical properties of the catalysts. During the synthesis of the catalysts, the properties of the support surface (i.e., quality and number of nucleation sites) influence the size, dispersion and morphology of the Au nanoparticles, and thereby the concentration of active, low coordinated sites. During catalytic operation the interface energy has a significant influence on the stability of the particles. Sintering of the nanoparticles can probably be partly suppressed by having a large interface energy present.

The fact that supported Au catalysts are active for a number of catalytic reactions at significant lower temperatures than more traditional catalysts makes them interesting for many technical applications. The lower reaction temperature will result in significant savings in both capital and operational costs and has the potential of increasing the selectivity of the various catalytic reactions making the reactions “cleaner”. In specific applications, such as exhaust and air cleaning and clean-up of hydrogen streams to low temperature PEM fuel cells, low reaction temperatures are a must and the Au catalysts may have a future in these technologies. Also

in neighboring fields, like electrocatalysis and sensor technology, technological applications of nanoparticles of Au may be realized.

Understanding the catalytic behavior of nanosized gold particles represents a very interesting challenge to our general understanding of heterogeneous catalysis. We have pointed to several factors which may contribute: the presence of low-coordinated Au atoms and promotion effects at the gold-support interface, but more work is clearly needed to unravel, in particular, the effects of the support.

### Acknowledgment

The Center for Atomic-scale Materials Design is supported by the Lundbeck Foundation. The Center for Sustainable and Green Chemistry is supported by the Danish National Research Foundation. In addition we thank the Danish Research Council for the Technical Sciences and the NABIIT programme for financial support, and Danish Center for Scientific Computing for computer time.

### References

- [1] M. Haruta, N. Kobayashi, H. Sano and N. Yamada, *Chem. Lett.* (1987) 405.
- [2] T. Kobayashi, M. Haruta, H. Sano and M. Nakane, *Sens. Actuators* 13 (1988) 339.
- [3] M. Haruta, N. Yamada, T. Kobayashi and S. Ijima, *J. Catal.* 115 (1989) 301.
- [4] M. Haruta, H. Kageyama, N. Kamijo, T. Kobayashi and F. Delannay, *Stud. Surf. Sci. Catal.* 44 (1989) 33.
- [5] M. Haruta, S. Tsubota, T. Kobayashi, H. Kageyama, M.J. Genet and B. Delmon, *J. Catal.* 144 (1993) 175.
- [6] M. Valden, X. Lai and D.W. Goodman, *Science* 281 (1998) 1647.
- [7] M. Valden, S. Pak, X. Lai and D.W. Goodman, *Catal. Lett.* 56 (1998) 7.
- [8] G.C. Bond and D.T. Thomson, *Catal. Rev. Sci. Eng.* 41 (1999) 319.
- [9] D.T. Wickham, D.H. Parker, G.N. Kastanas, M.A. Lazaga and B.E. Koel, *Prepr. - Am. Chem. Soc., Div. Pet. Chem.* 37 (1992) 1034.
- [10] M.A. Lazaga, D.T. Wickham, D.H. Parker, G.N. Kastanas and B.E. Koel, *ACS Symp. Ser.* 523 (1993) 90.
- [11] B. Hammer and J.K. Nørskov, *Nature* 376 (1995) 238.
- [12] T. Hayashi, K. Tanaka and M. Haruta, *Prepr. Am. Chem. Soc., Div. Pet. Chem.* 41 (1996) 71.
- [13] M. Haruta, *Stud. Surf. Sci. Catal.* 110 (1997) 123.
- [14] B.S. Uphade, M. Okumura, T. Hayashi and M. Haruta, *Chem. Lett.* (1998) 1277.
- [15] Y.A. Kalvachev, T. Hayashi, S. Tsubota and M. Haruta, *J. Catal.* 186 (1999) 228.
- [16] M.A.P. Dekkers, M.J. Lippits and B.E. Nieuwenhuys, *Catal. Today* 54 (1999) 381.
- [17] B.S. Uphade, M. Okumura, S. Tsubota and M. Haruta, *Appl. Catal. A* 190 (2000) 43.
- [18] T.V. Choudhary and D.W. Goodman, *Top. Catal.* 21 (2002) 25.
- [19] R.J.H. Grisel, J.J. Slyconish and B.E. Nieuwenhuys, *Top. Catal.* 16/17 (2001) 425.
- [20] R.J.H. Grisel and B.E. Nieuwenhuys, *Catal. Today* 64 (2001) 69.
- [21] S. Carrettin, P. McMorn, P. Johnston, K. Griffin and G.J. Hutchings, *Chem. Commun.* (2002) 696.
- [22] S. Schimpf, M. Lucas, C. Mohr, U. Rodemerck, A. Brückner, J. Radnik, H. Hofmeister and P. Claus, *Catal. Today* 72 (2002) 63.
- [23] P. Landon, P.J. Collier, A.J. Papworth, C.J. Kiely and G.J. Hutchings, *Chem. Commun.* (2002) 2058.
- [24] S. Carrettin, P. McMorn, P. Johnston, K. Griffin, C.J. Kiely and G.J. Hutchings, *Phys. Chem. Chem. Phys.* 5 (2003) 1329.
- [25] M. Okumura, Y. Kitagawa, K. Yamaguchi, T. Akita, S. Tsubota and M. Haruta, *Chem. Lett.* 32 (2003) 822.
- [26] J.A. Moulijn, A. Zwijnenburg, W.G. Sloof, M.W.J. Craje and M. Makkee, *Abstract of Papers, 226th ACS National Meeting, New York, NY* (2003).
- [27] S. Carrettin, P. McMorn, P. Johnston, K. Griffin, C.J. Kiely, G.A. Attard and G.J. Hutchings, *Top. Catal.* 27 (2004) 131.
- [28] R. Meyer, C. Lemire, S. Shaikhutdinov and H.J. Freund, *Gold Bull.* 37 (2004) 72.
- [29] M.D. Hughes, Y.J. Xu, P. Jenkins, P. McMorn, P. Landon D.I. Enache, A.F. Carley, G.A. Attard, G.J. Hutchings, F. King, E.H. Stitt, P. Johnston, K. Griffin and C.J. Kiely, *Nature* 437 (2005) 1132.
- [30] A. Abad, P. Concepcion, A. Corma and H. Garcia, *Angew. Chem. Int. Ed.* 44 (2005) 4066.
- [31] A.C. Gluhoi, M.A.P. Dekkers and B.E. Nieuwenhuys, *J. Catal.* 219 (2003) 197; *J. Catal.* 229 (2005) 154; *J. Catal.* 232 (2005) 96.
- [32] C.H. Christensen, B. Jørgensen, J. Rass-Hansen, K. Egeblad, R. Madsen, S.K. Klitgaard, S.M. Hansen, M.R. Hansen, H.C. Andersen and A. Riisager, *Ang. Chem. Int.* 45 (2006) 4648.
- [33] I.S. Nielsen, E. Taarning, K. Egeblad, R. Madsen and C.H. Christensen, *Catal. Lett.* DOI: 10.1007/s10562-007-9086-9 (2007).
- [34] T.A. Nijhuis, M. Makkee, J.A. Moulijn and B.M. Weckhuysen, *Ind. Eng. Chem. Res.* 45 (2006) 3447.
- [35] J.D. Grunwaldt, M. Maciejewski, O.S. Becker, P. Fabrizioli and A. Baiker, *J. Catal.* 186 (1999) 458.
- [36] M. Mavrikakis, P. Stoltze and J.K. Nørskov, *Catal. Lett.* 64 (2000) 101.
- [37] N. Lopez and J.K. Nørskov, *J. Am. Chem. Soc.* 124 (2002) 11262.
- [38] N. Lopez and J.K. Nørskov, *Surf. Sci.* 515 (2002) 175.
- [39] S. Shaikhutdinov, R. Meyer, M. Naschitzki, M. Baeumer and H.J. Freund, *Catal. Lett.* 86 (2003) 211.
- [40] G. Mills, M.S. Gordon and H. Metiu, *J. Chem. Phys.* 118 (2003) 4198.
- [41] C. Lemire, R. Meyer, S. Shaikhutdinov and H.-J. Freund, *Surf. Sci.* 552 (2004) 27.
- [42] C. Lemire, R. Meyer, S. Shaikhutdinov and H.J. Freund, *Angew. Chem. Int. Ed.* 43 (2004) 118.
- [43] N. Lopez, T.V.W. Janssens, B.S. Clausen, Y. Xu, M. Mavrikakis, T. Bligaard and J.K. Nørskov, *J. Catal.* 223 (2004) 232.
- [44] R. Zanello, S. Giorgio, C.H. Shin, C.R. Henry and C. Louis, *J. Catal.* 222 (2004) 357.
- [45] M.M. Biener, J. Biener and C.M. Friend, *Surf. Sci.* 590 (2005) L259.
- [46] X. Deng, B.K. Min, A. Guloy and C.M. Friend, *J. Am. Chem. Soc.* 127 (2005) 9267.
- [47] T.V.W. Janssens, A. Carlsson, A. Puig-Molina and B.S. Clausen, *J. Catal.* 240 (2006) 108.
- [48] X. Lai, T.P. Clair, M. Valden and D.W. Goodman, *Prog. Surf. Sci.* 59 (1998) 25.
- [49] X. Lai and D.W. Goodman, *J. Mol. Catal. A* 162 (2000) 33.
- [50] Z. Yang, R. Wu and D.W. Goodman, *Phys. Rev. B* 61 (2000) 14066.
- [51] A. Sanchez, S. Abbet, U. Heiz, W.-D. Schneider, H. Häkkinen, R.N. Barnett and U. Landman, *J. Phys. Chem. A* 103 (1999) 9573.
- [52] D. Ricci, A. Bongiorno, G. Pacchioni and U. Landman, *Phys. Rev. Lett.* 97 (2006) 036106.



- [53] J.A. Bokhoven, C. Louis, J.T. Miller, M. Tromp, O.V. Safonova and P. Glatzel, *Angew. Chem. Int. Ed.* 45 (2006) 4651.
- [54] M. Okumura, S. Nakamura, S. Tsubota, T. Nakamura M. Azuma and M. Haruta, *Catal. Lett.* 51 (1998) 53.
- [55] M.M. Schubert, S. Hackenberg, A.C. van Veen, M. Muhler, V. Plzak and R.J. Behm, *J. Catal.* 113 (2001) 197.
- [56] Z.P. Liu, P. Hu and A. Alavi, *J. Am. Chem. Soc.* 124 (2002) 14770.
- [57] L.M. Molina and B. Hammer, *Phys. Rev. Lett.* 90 (2003) 206102.
- [58] L.M. Molina and B. Hammer, *Phys. Rev. B* 69 (2004) 155424.
- [59] L.M. Molina, M.D. Rasmussen and B. Hammer, *J. Chem. Phys.* 120 (2004) 7673.
- [60] G.C. Bond and D.T. Thompson, *Gold Bull.* 33 (2000) 41.
- [61] L.M. Molina and B. Hammer, *Appl. Catal. A* 291 (2005) 21.
- [62] H. Sakurai, T. Akita, S. Tsubota, M. Kiuchi and M. Haruta, *Appl. Catal. A* 291 (2005) 179.
- [63] L.M. Liu, B. McAllister, H.Q. Ye and P. Hu, *J. Am. Chem. Soc.* 128 (2006) 4017.
- [64] B. Hammer, *Top. Catal.* 37 (2006) 3.
- [65] R.M. Finch, N.A. Hodge, G.J. Hutchings, A. Meagher Q.A. Pankhurst, M.R. Siddiqui, F.E. Wagner and R. Whyman, *Phys. Chem. Chem. Phys.* 1 (1999) 485.
- [66] Z. Hao, L. An, H. Wang and T. Hu, *React. Kinet. Catal. Lett.* 70 (2000) 153.
- [67] N.A. Hodge, C.J. Kiely, R. Whyman, M.R.H. Siddiqui G.J. Hutchings, Q.A. Pankhurst, F.E. Wagner, R.R. Rajaram and S.E. Golunski, *Catal. Today* 72 (2002) 133.
- [68] P. Bera and M.S. Hegde, *Catal. Lett.* 79 (2002) 75.
- [69] H.H. Kung, M.C. Kung and C.K. Costello, *J. Catal.* 216 (2003) 425.
- [70] J. Guzman and B.C. Gates, *J. Am. Chem. Soc.* 126 (2004) 2672.
- [71] C.K. Costello, J. Guzman, J.H. Yang, Y.M. Wang, M.C. Kung, B.C. Gates and H.H. Kung, *J. Phys. Chem. B* 108 (2004) 12529.
- [72] S. Carrettin, P. Concepcion, A. Corma, J.M. Lopez Nieto and V.F. Puentes, *Angew. Chem. Int. Ed.* 43 (2004) 2538.
- [73] J.C. Fierro-Gonzalez and B.C. Gates, *J. Phys. Chem. B* 108 (2004) 16999.
- [74] J.C. Fierro-Gonzalez, B.G. Anderson, K. Ramesh, C.P. Vinod, J.W. Niemantsverdriet and B.C. Gates, *Catal. Lett.* 101 (2005) 265.
- [75] S. Carrettin, A. Corma, M. Iglesias and F. Sanchez, *Appl. Catal. A* 291 (2005) 247.
- [76] L. Fu, N.Q. Wu, J.H. Yang, F. Qu, D.L. Johnson, M.C. Kung, H.H. Kung and V.P. Dravid, *J. Phys. Chem. B* 109 (2005) 3704.
- [77] C. Gonzalez-Arellano, A. Corma, M. Iglesias and F. Sanchez, *J. Catal.* 238 (2006) 497.
- [78] A. Comas-Vives, C. Gonzalez-Arellano, A. Corma, M. Iglesias, F. Sanchez and G. Ujaque, *J. Am. Chem. Soc.* 128 (2006) 4756.
- [79] P. Concepcion, S. Carrettin and A. Corma, *Appl. Catal. A* 307 (2006) 42.
- [80] G.J. Hutchings, M.S. Hall, A.F. Carley, P. Landon, B.E. Solsona, C.J. Kiely, A. Herzing, M. Makkee, J.A. Moulijn and A. Overweg, *J. Catal.* 242 (2006) 71.
- [81] S. Chretien and H. Metiu, *Catal. Lett.* 107 (2006) 143.
- [82] A. Baiker, J.D. Grunwaldt, C.A. Mueller and L. Schmid, *Chimia* 52 (1998) 517.
- [83] A. Wolf and F. Schuth, *Appl. Catal. A* 226 (2002) 1.
- [84] A.K. Sinha, S. Seelan, T. Akita, S. Tsubota and M. Haruta, *Appl. Catal. A* 240 (2003) 243.
- [85] C. Aprile, A. Abad, H. Garcia and A. Corma, *J. Mater. Chem.* 15 (2005) 4408.
- [86] T. Bligaard, J.K. Nørskov, S. Dahl, J. Matthiesen, C.H. Christensen and J. Sehested, *J. Catal.* 224 (2004) 206.
- [87] J. Kim, E. Samano and B.E. Koel, *Surf. Sci.* 600 (2006) 4622.
- [88] A. Nilsson, L.G.M. Pettersson, B. Hammer, T. Bligaard, C.H. Christensen and J.K. Nørskov, *Catal. Lett.* 100 (2005) 111.
- [89] S.D. Lin, M. Bollinger and M.A. Vannice, *Catal. Lett.* 17 (1993) 245.
- [90] Y. Yuan, K. Asakura, H. Wan, K. Tsai and Y. Iwasawa, *Catal. Lett.* 42 (1996) 15.
- [91] M. Haruta, *Catal. Today* 36 (1997) 153.
- [92] S.J. Lee and A. Gavriilidis, *J. Catal.* 206 (2002) 305.
- [93] J.T. Calla, M.T. Bore, A.K. Datye and R.J. Davis, *J. Catal.* 238 (2006) 458.
- [94] S.H. Overbury, V. Schwartz, D.R. Mullins, W. Yan and S. Dai, *J. Catal.* 241 (2006) 56.
- [95] E. Wahlstrom, N. Lopez, R. Schaub, P. Thosttrup, A. Ronnau, C. Africh, E. Lægsgaard, J.K. Nørskov and F. Besenbacher, *Phys. Rev. Lett.* 90 (2003) 026101.
- [96] I.N. Remediakis, N. Lopez and J.K. Nørskov, *Angew. Chem. Int. Ed.* 44 (2005) 1824.
- [97] N. Lopez, J.K. Nørskov, T.V.W. Janssens, A. Carlsson, A. Puig-Molina, B.S. Clausen and J.-D. Grunwaldt, *J. Catal.* 225 (2004) 86.
- [98] Z.P. Liu, X.Q. Gong, J. Kohanoff, C. Sanchez and P. Hu, *Phys. Rev. Lett.* 91 (2003) 266102.
- [99] M.A. Bollinger and M.A. Vannice, *Appl. Catal. B* 8 (1996) 417.
- [100] J.K. Nørskov, T. Bligaard, A. Logadottir, S. Bahn, L.B. Hansen, M. Bollinger, H. Bengaard, B. Hammer, Z. Sljivancanin and M. Mavrikakis, *J. Catal.* 209 (2002) 275.
- [101] B. Hammer and J.K. Nørskov, *Adv. Catal.* 45 (2000) 71.
- [102] J. Kim, E. Samano and B.E. Koel, *J. Phys. Chem. B* 110 (2006) 17512.
- [103] C. Ruggiero and P. Hollins, *J. Chem. Soc. Farad. Trans.* 92 (1996) 4829.
- [104] J.M. Gottfried, K.J. Schmidt, S.L.M. Schroeder and K. Christmann, *Surf. Sci.* 536 (2003) 206.
- [105] D.C. Meier, V. Bukhtiyarov and D.W. Goodman, *J. Phys. Chem. B* 107 (2003) 12668.
- [106] J.D. Stiehl, T.S. Kim, S.M. McClure and C.B. Mullins, *J. Phys. Chem. B* 109 (2005) 6316.
- [107] B.K. Min, X. Deng, D. Pinnaduwege, R. Schalek and C.M. Friend, *Phys. Rev. B* 72 (2005) 121410.
- [108] A. Carlsson, A. Puig-Molina and T.V.W. Janssens, *J. Phys. Chem. B* 110 (2006) 5286.
- [109] R. van Hardeveld and F. Hartog, *Surf. Sci.* 15 (1969) 189.
- [110] B. Yoon, H. Häkkinen and U. Landman, *J. Phys. Chem. A* 107 (2003) 4066.
- [111] X. Wu, L. Senapati, S.K. Nayak, A. Selloni and M. Hajaligol, *J. Chem. Phys.* 117 (2002) 4010.
- [112] G. Mills, M.S. Gordon and H. Metiu, *Chem. Phys. Lett.* 359 (2002) 493.
- [113] J.M. Gottfried, K.J. Schmidt, S.L.M. Schroeder and K. Christmann, *Surf. Sci.* 511 (2002) 65.
- [114] T. Bar, T.V. De Bocarme, B.E. Nieuwenhuys and N. Kruse, *Catal. Lett.* 74 (2001) 127.
- [115] J.M. Gottfried and K. Christmann, *Surf. Sci.* 566–568 (2004) 1112.
- [116] J.D. Stiehl, T.S. Kim, C.T. Reeves, R.J. Meyer and C.B. Mullins, *J. Phys. Chem. B* 108 (2004) 7917.
- [117] J.-D. Grunwaldt, C. Kiener, C. Wögerbauer and A.J. Baiker, *J. Catal.* 181 (1999) 223.
- [118] M. Comotti, W.C. Li, B. Spliethoff and F. Schüth, *J. Am. Chem. Soc.* 128 (2006) 917.
- [119] S.C. Parker, A.W. Grant, V.A. Bondzie and C.T. Campbell, *Surf. Sci.* 441 (1999) 10.
- [120] L. Zhang, F. Cosandey, R. Persaud and T.E. Madey, *Surf. Sci.* 439 (1999) 73.
- [121] J.T. Calla and R.J. Davis, *J. Catal.* 241 (2006) 407.
- [122] M. Maciejewski, P. Fabrizioli, J.D. Grunwaldt, O.S. Becker and A. Baiker, *Phys. Chem. Chem. Phys.* 3 (2001) 3846.
- [123] W. Yan, S. Brown, Z. Pan, S.M. Mahurin, S.H. Overbury and S. Dai, *Angew. Chem. Int. Ed.* 45 (2006) 3614.
- [124] G. Ertl, S.B. Lee and M. Weiss, *Surf. Sci.* 114 (1982) 527.
- [125] J.K. Nørskov, S. Holloway and N.D. Lang, *Surf. Sci.* 137 (1984) 65.

- [126] S.R. Bare, D.R. Strongin and G.A. Somorjai, *J. Phys. Chem.* 90 (1986) 4726.
- [127] J.J. Mortensen, B. Hammer and J.K. Nørskov, *Phys. Rev. Lett.* 80 (1998) 4333.
- [128] R.J.H. Grisel and B.E. Nieuwenhuys, *J. Catal.* 199 (2001) 48.
- [129] R.J.H. Grisel, C.J. Weststrate, A. Goossens, M.W.J. Craje, A.M. Kraan and B.E. Nieuwenhuys, *Catal. Today* 72 (2002) 123.